Field Aligned Currents Derived from Pressure Profiles Obtained from TWINS ENA Images

by

Keith D. Wood

A dissertation submitted to the Graduate Faculty of
Auburn University
in partial fulfillment of the
requirements for the Degree of
Doctor of Philosophy

Auburn, Alabama
December 16, 2017

Keywords: Magnetospheric Physics, Space Physics, Birkeland Currents, Field Aligned Currents, TWINS

Approved by

Joseph D. Perez, Chair, Professor of Physics
Yu Lin, Professor of Physics
Kaijun Liu, Assistant Professor of Physics
David Maurer, Associate Professor of Physics

Abstract

Field aligned currents (FACs) are an important mechanism coupling the Earth's magnetosphere and ionosphere. The Two Wide-Angle Imaging Neutral-atom Spectrometers (TWINS) mission is the first stereoscopic neutral atom imager. Identical energetic neutral atom (ENA) detectors are placed on widely separated satellites, allowing nearly continuous monitoring of the Earth's inner magnetosphere. TWINS ENA measurements, combined with the Tsyganenko and Sitnov 2005 (TS05) magnetic field model, yield ion pressure profiles. Calculations are performed in the quasistatic approximation, allowing FACs to be determined from the ion pressure profiles.

TWINS ENA measurements allow the pitch angle distribution (PAD) of the ions to be determined. These PADs allow anisotropic pressure distributions to be determined. This work calculates FACs using the measured PAD anisotropy from TWINS and compares these calculations to those done assuming an isotropic ion pressure the corotating interaction region (CIR) storm of 01 June 2013. The results are very similar in most cases, but important differences are observed. These differences indicate that pressure anisotropy is important for fine-scale structures in the FACs during geomagnetic stormtime.

The calculation of FACs in the anisotropic pressure case involves an integral with three terms. In the case of isotropic pressure, two of these terms are eliminated. The current densities due to each term are evaluated and compared for several points on the northern ionosphere. In regions where the two cases differ substantially, it is shown that the term appearing in the isotropic case is exceeded by one of the purely anisotropic terms, leading to differences in magnitude and direction of the current.

The evolution of pressure and current density along magnetic field lines is examined at several locations. These indicate that FACs dominate the current near the ionosphere, while currents perpendicular to the magnetic field are more important near the equatorial plane. Current paths are traced through the inner magnetosphere, beginning at several locations on the

equatorial plane, and at the ionosphere. These paths indicate that the simple picture of FACs moving along field lines from the ionosphere to the ring current misses important aspects of the current behavior.

Acknowledgments

The journey to a Ph.D. is long and difficult, and I could not have completed it without the guidance and support of numerous people. I am especially grateful to my advisor, Joseph Perez, who introduced me to magnetospheric physics and helped me develop my research skills. I would also like to thank our collaborators, particularly Mei-Ching Fok and Natasha Buzulukova who both offered invaluable advice and encouragement. I am also indebted to my dissertation committee: David Maurer, Yu Lin, Kaijun Liu, and Dan Marghitu. Because of their comments and suggestions, this dissertation is a great deal better.

To my wonderful girlfriend, Megan Flannery: I am truly thankful for your help and support. Your cheerful encouragement helped me keep everything in perspective. I can't imagine doing this without you.

To my great friend and fellow Ph.D. recipient, Nathalia Alzate: we made it! It has been a very long road for both of us, but we made it to the end. Time for us to make a mark on this field!

To my parents, Judith and Charles Wood: Your endless emotional support (and occasional financial support) has meant the world to me. Without you, I would certainly not be where I am today.

Thank you to everyone who has helped to make this possible.

Table of Contents

List of Figures

Chapter 1

Introduction

1.1 History of Magnetospheric Physics

The effects of magnetism have been observed for thousands of years. By 1000 AD the magnetic compass had been invented in China, and its use quickly spread through the Arab world and Europe as a navigational aid. Despite the early use of the Earth's magnetic field as a tool, it wasn't until the year 1600 that the idea of a magnetosphere began to form. In this year, William Gilbert - an English physician and amatuer natural philosopher - published the results of his research with a magnetized sphere, which he called a terella. It was known through the work of Robert Norman that the force felt by compass needles was not horizontal; it had a component pointing toward the ground as well. Further, mariners had long reported that magnetic north did not exactly align with true north. Gilbert experimented with small compass needles near the surface of his terrella, and observed that their behavior closely approximated the observations of Norman. This led Gilbert to hypothesize that the Earth is a giant spherical magnet due to an iron core.

In 1635, it was realized that the Earth's magnetic field was not constant. Through careful analysis of previous observations, an English mathematician named Henry Gellibrand discovered that magnetic declination changed over time. This variation was quite slow. Nearly a century later, in 1724, Graham observed large, rapid, and irregular changes in the direction of compass needles, which he dubbed "magnetic storms". In 1741, the Swedish astronomers Olof Hiorter and Anders Celsius observed similar fluctuations in compass needles during a polar aurora event, indicating that the aurora are associated with magnetic storms.

The discovery by Hans Christian Oersted in 1820 that magnetic effects can be produced by electric currents was the first strong evidence that the effects seen in magnetic storms were

caused by electric currents. While the idea of electric currents in the upper atmosphere or beyond was not well received at the time, it gained more traction in the century that followed as more evidence was obtained. In 1843, Samuel Schwabe reported the existence of the sunspot cycle, an eleven year cycle during which the number of visible sunspots waxes and wanes. In 1859, Richard Carrington observed a solar flare approximately 17 hours before a magnetic storm occurred on Earth, and postulated that the two were connected. This hypothesis was confirmed by George Ellery Hale. In 1892, Hale introduced the spectroheliograph, which drastically improved the ability to detect solar flares. With these more sensitive observations, the association of magnetic storms and solar flares was quickly confirmed.

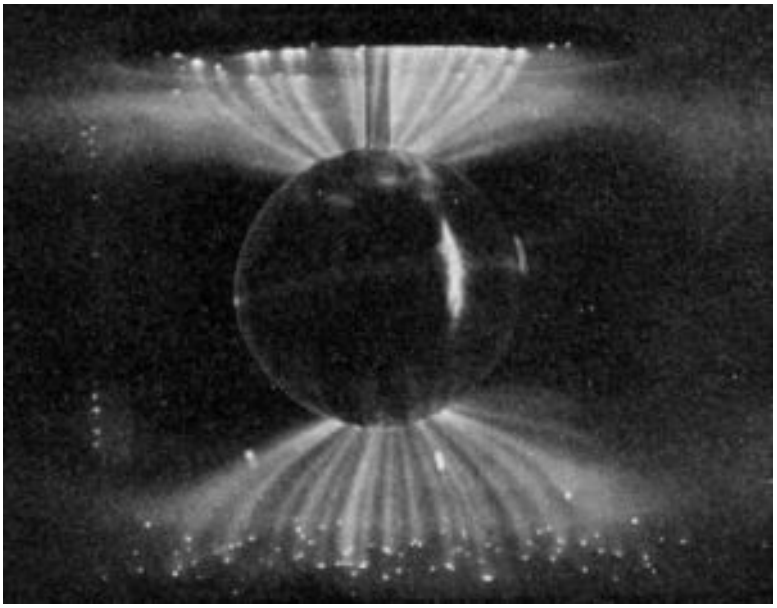

Figure 1.1: Kristian Birkeland's terrella. Placed in a vacuum chamber, an electron beam is fired at this spherical magnet. The electrons are deflected to the polar regions of the terrella. Image from plasma-universe.com

In the earliest years of the twentieth century, Kristian Birkeland returned to Gilbert's terrella experiments, although the intervening centuries had granted Birkeland much more sophisticated techniques than were available to Gilbert. In Birkeland's experiments, the terrella was placed in a vacuum chamber in order to more closely approximate the region of space beyond the Earth's atmosphere. A beam of electrons (called cathode rays at the time) was fired at the terrella. Instead of striking the terrella near the equator as the beam line would indicate, however, the electrons were deflected by the terrella's magnetic field, striking near the poles.

In addition to his laboratory experiments with terrellae, Birkeland conducted expeditions north of the arctic circle to establish a network of stations which observed the magnetic field during times of active aurora borealis. His results with the terrellae, combined with the information gained from his observatories and the pioneering work done by others before, led Birkeland to propose that magnetic storms, and the aurora, were caused by a stream of electrons flowing from the Sun.

Also in the early twentieth century, significant advances were being made in the field of long distance communications. Guglielmo Marconi, one of the pioneers of radio communications, claimed to have made the first wireless transmission across the Atlantic in 1901. While the veracity of this claim is doubted by many, it spurred investigations into the manner in which the signal overcame the problem of the Earth's curvature, since a straight-line path is impossible over such distances without traveling beneath the surface of the Earth. This problem was solved by Oliver Heaviside, who hypothesized a conducting layer high in the atmosphere, which could reflect the radio transmission. This layer is now called the ionosphere.

By 1930, Birkeland's hypothesis that magnetic storms were caused by a flow of electrons from the Sun had been rejected. It was shown that such a flow would cause the Earth to build up a large electrostatic charge very quickly, which would interrupt the current and eliminate both magnetic storms and the aurora. Sydney Chapman and Vincent Ferraro saw that Birkeland's ideas could be made to work if the charge could be kept neutral. With this in mind, they proposed a flow of both ions and electrons; separate positive and negative charges, but taken as a whole, neutrally charged - what is now called a plasma, though the word was not yet widely used in physics.

Chapman and Ferraro proposed a model in which clouds of plasma were ejected from the Sun, causing magnetic storms when the cloud reached and surrounded Earth. They realized that for a sufficiently large cloud, the leading edge approaching Earth could be treated as an effectively infinite wall. This allowed them to employ an approximation already worked out by Maxwell; by treating the Earth's magnetic field as a dipole and assuming perfect conductivity in the cloud's plasma, they could employ the method of images to calculate the cloud's magnetic field at the Earth. The Earth's magnetic field affects the plasma cloud, too. Since

the cloud is approaching the Earth, the magnetic field it feels grows stronger, changing over time, and inducing a current in the plasma cloud. These currents are deflected by the Earth's magnetic field. As the plasma cloud overtakes the Earth, the magnetic deflection of the currents in the plasma results in the formation of a cavity within the cloud, surrounding the Earth. This Chapman-Ferraro cavity was an important conceptual advance, underpinning the current understanding of the magnetopause.

By the mid-1950s, James Van Allen had begun his rocket experiments, launching scientific instruments into the upper atmosphere in the auroral zone to detect radiation. In 1957, the Soviet Union launched Sputnik, the world's first satellite. While this satellite carried no scientific instruments, it ushered in the age of spacecraft-based observations. Van Allen and his collaborators used their expertise in rocket-based science to design a space-based package of scientific instruments called Explorer 1. Launched in 1958, Explorer 1 was launched on the United States' very first Juno rocket, and returned data for almost four months. This mission revealed the first evidence of the radiation belts surrounding Earth. Explorer 3, also launched in 1958, confirmed the observations of Explorer 1, and provided further evidence of the radiation belts. These radiation belts are now called Van Allen belts, in honor of his contributions to their discovery.

Meanwhile, Eugene Parker was studying the solar corona. It was known that temperatures in the corona were generally more than 10^6 K, much hotter than in the underlying photosphere. This presented an interesting question, since one would expect outlying layers to be cooler than those closer to the core. Indeed, this is still an active area of research. In 1958, Parker attempted to find the equilibrium structure of the Sun's corona, but found that it was impossible to make such a solution work given the observations that had already occurred. Instead, he proposed a solution in which the upper layer of the photosphere is continually blown off the Sun, resulting in a constant flow of material from the Sun. This is now called the solar wind, and has been confirmed by numerous satellite observations. This idea extended the Chapman-Ferraro model of plasma clouds to involve a constant flow of plasma, interrupted by sporadic bursts of material.

In the early 1970s, Alfred Zmuda and Jim Armstrong used magnetometer data from the United States Navy's Triad satellite to determine that, as predicted by Chapman and Ferraro, there were large scale current systems flowing into and out of the Earth's auroral zones. This work was published in 1974, though both researchers had died prior to publication. These currents flowed largely along field lines, and are thus commonly called field aligned currents, and have been named Birkeland currents in honor of Kristian Birkeland, whose work with terrellae laid the foundations of this research.

1.2 The Earth's Magnetosphere

The Earth's magnetosphere is the region of space in which the behavior of charged particles is determined primarily by the Earth's magnetic field. While Earth's inherent magnetic field is approximately dipolar, the geomagnetic field is determined by the addition of the dipolar field with the interplanetary magnetic field (IMF), carried by the solar wind. As can be seen in figure 1.2, the flow of the solar wind compresses the geomagnetic field on the side nearest the Sun, and elongates it on the side opposite. The region of compression terminates on the sunward side with the bow shock, so called because it resembles the wave of water coming off the front of a moving ship. The bow shock separates the magnetosphere from the ambient interplanetary medium, and under quiescent conditions is located approximately 14 R_E sunward from the Earth. Behind the bow shock is a layer of thermalized plasma called the magnetosheath, which serves as an intermediary between the magnetosphere and the solar wind, allowing particles from the solar wind to pass, but reducing the pressure from them.

The magnetotail is the region of the magnetosphere on the far side of the Earth from the Sun, characterized by stretched magnetic field lines, elongated into the shape of a long tail. This tail has two large lobes, one north of the equatorial plane, and one south of it. These lobes are characterized by long, nearly parallel magnetic field lines. In the northern lobe, the field lines point towards the Earth, while in the southern lobe they point away. These field lines connect with the Earth at high latitudes, forming a roughly circular shape around the poles. Separating the two lobes is a region called the plasma sheet, which has a higher plasma density and lower

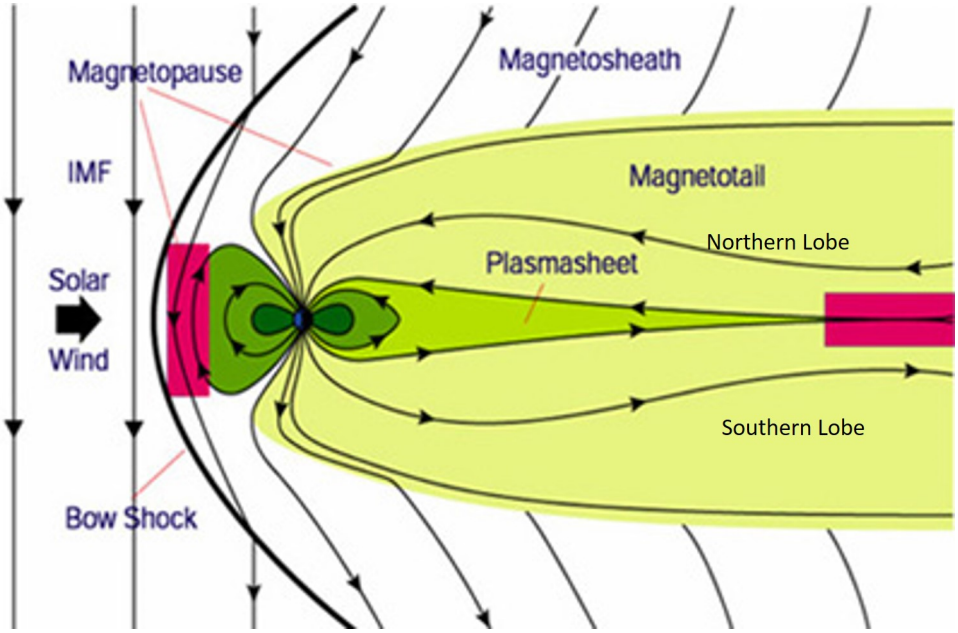

Figure 1.2: Diagram of the Earth's magnetosphere interacting with the solar wind. From http://mms.space.swri.edu/mission.html

magnetic field strength than the two lobes. The plasma sheet varies from approximately two to six R_E in width, and is approximately centered on the equatorial plane.

The magnetopause is layer at which the pressure from the magnetosphere is exactly balanced by the pressure from the solar wind. The equilibrium layer can be thought of as the boundary between the Earth's magnetosphere and the interplanetary medium. While the position of the magnetopause will vary based on solar wind conditions, under quiescent conditions it is typically 10.5 R_E from Earth on the sunward side, stretching to more than 25 R_E on the tailward side.

Within these magnetospheric regions live a number of plasma populations and currents that help to give the magnetosphere the structure it has, as illustrated in figure 1.3. In the Earth's upper atmosphere lies the ionosphere. The ionosphere is so named because the gas in this region is ionized by radiation from the Sun. While the structure of the ionosphere can be quite complicated, the upper region typically lies at approximately 1000 km altitude and forms the base of the magnetosphere.

Beyond the ionosphere is a population of ions and electrons called the plasmasphere. This region is filled with cold, relatively dense plasma, primarily from the Earth's upper atmosphere.

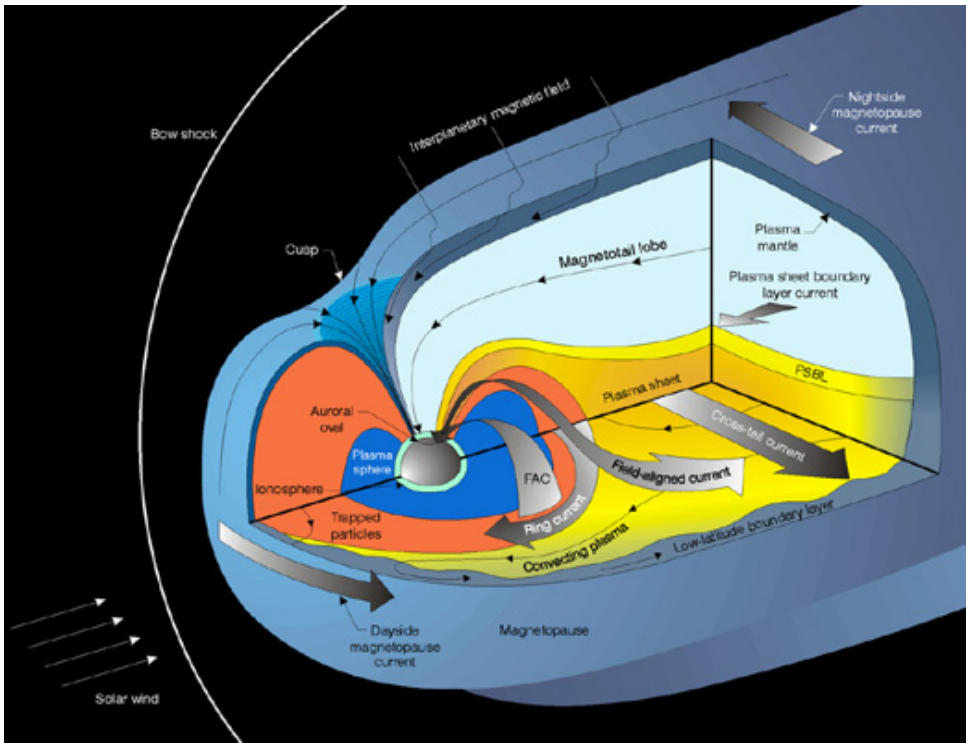

Figure 1.3: Illustration of the composition of the Earth's magnetosphere. From http://mms.space.swri.edu/science-4.html

Because of the low energy of this plasma, the ions and electrons become tied to geomagnetic field lines such that the plasmasphere rotates in the same direction as the Earth, lagging the Earth's rotation rate by about ten percent. The outer boundary of the plasmasphere is called the plasmapause, and is defined by a marked drop in plasma pressure. The plasmapause is typically 3-7 R_E from Earth.

The Van Allen radiation belts are regions of high energy charged particles. There are typically two belts: an outer belt composed primarily of high energy electrons, along with hydrogen, helium, and oxygen ions, and an inner belt composed primarily of energetic ions, most of which are protons, and lower energy electrons. The outer belt is populated primarily by the solar wind, while the inner belt is populated by a combination of solar wins particles and ions generated from neutron decay in the upper ionosphere. The inner belt ranges from about 0.2 to 2 R_E from the Earth's surface, while the outer belt extends from 3 to 10 R_E, with a peak concentration typically around 4-5 R_E. These belts pose a serious hazard to orbiting spacecraft due to the high energy of the plasma. Thus, spacecraft traversing this region typically have sensitive onboard electronics carefully shielded.

The ring current is a region of current carried by energetic charged particles, primarily hydrogen ions, in the equatorial plane surrounding Earth. The ring current typically lies between $L = 2$ and $L = 7$, and flows in the direction opposite to the Earth's rotation; that is, clockwise when looking down on the northern hemisphere. The magnetic field induced by this current serves to reduce the geomagnetic field at the Earth's surface, due to the current's direction. Because the ring current increases in magnitude during geomagnetic storms, the magnetic field measured at the Earth's surface will drop during these storms. The activity of the ring current can be observed in either the Dst index or the Sym/H index. The Sym/H index will be used in this work, and will be explained in a later chapter.

In addition to the ring current, there are several other currents in the magnetosphere such as the cross-tail current, which runs from the dawn side to the dusk side across the magnetotail in the plasma sheet, and magnetopause currents, which run from dawn to dusk across the day side of magnetopause, and from dusk to dawn on the nightside. Additionally, there are field aligned currents, which will be discussed at greater length in the next section, and are an important component of this research.

1.3 Field Aligned Currents

Field aligned currents are currents traveling either parallel or antiparallel to the geomagnetic field. While these currents will necessarily create magnetic fields perpendicular to the geomagnetic field lines, the magnitude of these fields is generally very small in comparison, and may be neglected. When traveling parallel to a geomagnetic field line, of course, the charged particles of which the current is composed of feel no magnetic force; thus, they continue to travel in a straight line along the magnetic field line until they are scattered by another particle onto another trajectory, or the magnetic field line changes its direction.

This work will examine a type of field aligned currents called Birkeland currents, named for Kristian Birkeland who first proposed their existence. These currents are important mechanisms in coupling the Earth's magnetosphere to its ionosphere. These currents typically occur most strongly near dawn and dusk. Further, they are typically found in two distinct regions.

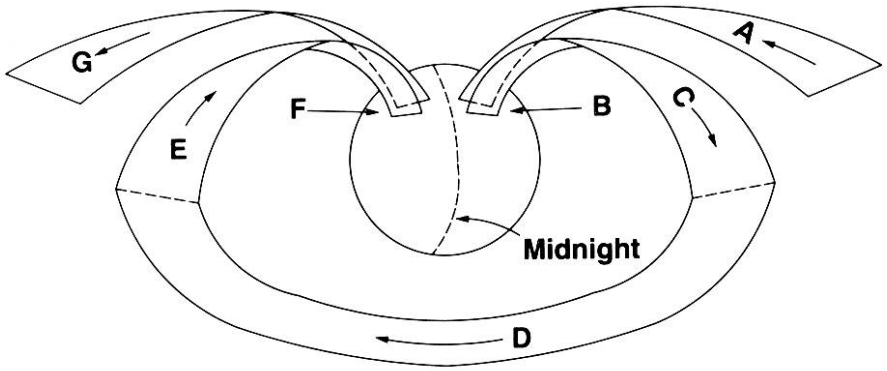

Figure 1.4: Illustration of the Region 1 and 2 Birkeland Currents. One picture of the Birkeland currents has them enter the ionosphere near dawn as Region 1 currents (A). These currents may join the outward Region 1 currents (G) via the polar ionosphere through either Hall or Pedersen currents or, as in this sketch, join the Region 2 currents via a shorter path in the ionosphere (B). The outward Region 2 current (C) connects to the ring current (D), and from there to the inward Region 2 current (E), which connects to the ionosphere near dusk. This current connects to the outward Region 1 current (G) via the ionosphere (F), where it leaves the inner magnetosphere. From https://www-spof.gsfc.nasa.gov/Education/whcurren.html

In the classical picture, Region 1 currents flow into the ionosphere on the dawn side of the Earth, and out on the dusk side, along ”open” magnetic field lines. These field lines are not truly open; they do obey $\nabla \cdot \vec{B} = 0$. However, they leave the inner magnetosphere. Region 2 currents, on the other hand, flow along ”closed” magnetic field lines. These currents flow into the ionosphere near dusk, and out near dawn, and remain trapped in the inner magnetosphere. This work will focus on Region 2 currents during a geomagnetic storm.

1.4 Geomagnetic Storms

There are two main causes of geomagnetic storms: Interplanetary Coronal Mass Ejections (ICMEs) and Corotating Interaction Regions (CIRs). ICMEs are very large bubbles of dense plasma blown off the surface of the Sun. When traveling toward the Earth, they are sometimes called Halo CMEs, because they often have a larger angular diameter than the Sun, forming a halo around it. By the time an ICME reaches the Earth, a distance of 1 astronomical unit (AU) from the Sun, the ICME is often more than 0.25 AU in diameter. These events carry a very large

amount of energy, and are often highly effective at transferring that energy into the magnetospheric system. This is especially true if the magnetic field of the ICME has a strong southward component, which facilitates magnetic reconnection with the northward geomagnetic field.

ICME storms are characterized by a sudden storm commencement (SSC), where the Sym/H index suddenly increases before dropping to negative values, a strong magnetic field, and a relatively short recovery period. High ion speeds are also common, with some storms exceeding 2000 km/s. ICME storms can occur at any time during the solar cycle, but are far more common near sunspot maximum, when an average of five coronal mass ejections per day erupt from the Sun.

CIRs are long lasting features associated with regions on the Sun called coronal holes. Coronal holes are regions in which the density of the coronal plasma is lower than in surrounding regions. This allows dense, energetic plasma from the lower corona to escape as a fast solar wind, which is funneled out by the corona and slow solar wind. These directed flows of plasma can extend to Earth, where they trigger geomagnetic storms.

Because CIRs are associated with coronal holes, which can persist for several rotations of the Sun, they may repeat periodically, approximately every 27 days. During storms associated with CIRs, the ion temperature can go quite high; as high as 10^6 K. CIR storms also generally lack a SSC, and often have very long recovery phases. Like ICMEs, CIRs may occur at any time. However, they are substantially more likely to occur during the declining phase of the solar cycle; that is, after solar maximum but before solar minimum. The storm analyzed in this research is a CIR storm.

Chapter 2

TWINS

2.1 Mission

The Two Wide-angle Imaging Neutral-atom Spectrometers (TWINS) mission is a NASA mission-of-opportunity. The first stereoscopic neutral atom imager, identical TWINS energetic neutral atom (ENA) detectors are located on two widely separated satellites placed in Molniya orbits. Commonly used for Russian communications satellites, Molniya orbits are highly eccentric, with an orbital inclination of 63.4 degrees and orbital period of twelve sidereal hours. The TWINS satellites have an apogee of 7.2 Earth radii (R_E). Due to the eccentricity of the orbits, the spacecraft spend most of their time near apogee, allowing them to collect data for extended periods. Because the orbits of the two spacecraft are widely separated, the TWINS detectors achieve near-continuous coverage of the Earth's magnetosphere. Further, when both spacecraft are in a favorable position to observe, stereoscopic imaging can be achieved.

Each ENA detector records a line-of-sight measurement of the neutral atoms impinging on it. The measured neutral atoms arise from charge exchange between magnetospheric ions and cold geocoronal hydrogen. This charge exchange process results in the magnetospheric ions gaining an electron, becoming neutral and thus no longer being affected by the geomagnetic field. From McComas et al. [2009], the ENA flux is described by:

$$j_{ena} = \int n_H j_{ion} \sigma dl \tag{2.1}$$

where j_{ena} is the flux of ENAs at the detector, n_H is the geocoronal neutral hydrogen density, j_{ion} is the ion intensity, and σ is the charge-exchange cross section. The integral is taken over the emitting volume. n_H is a function of position in the geocorona, and will vary along the line-of-sight path. This quantity is determined through the TWINS Geocorona Model [Zoennchen et al. 2011].

While this integral appears straight forward, j_{ena} is measured during observation; it is j_{ion} that must be derived from this measurement. A deconvolution process is used to separate j_{ion} from the integral on the right hand side of the equation. This process is described in detail in Perez et al. [1999].

2.2 Instrumentation

Figure 2.1 shows the TWINS instrument, which among other parts comprises two ENA sensor heads, a dual-headed Lyman-alpha detector, and a data processing unit. The Lyman-alpha detectors give important information about the Earth's geocorona, which is used to constrain the TWINS geocoronal model. The data processing unit gives the TWINS research team spacecraft command and telemetry interface, and controls both the ENA and Lyman-alpha detectors.

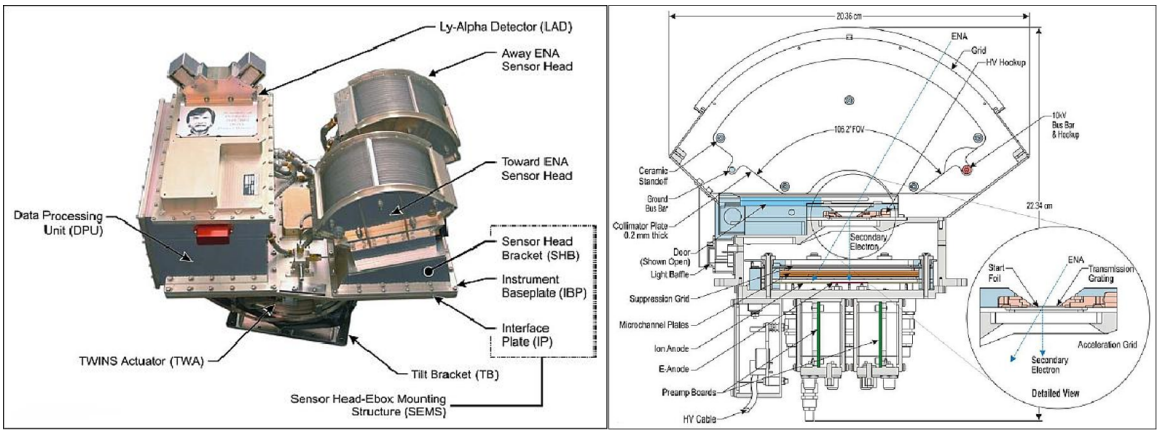

Figure 2.1: TWINS Instrument: Left - Labeled picture of TWINS instrument. Right - Schematic diagram of ENA detector. Image credit: TWINS Consortium

The TWINS ENA detectors are able to detect neutral hydrogen atoms with kinetic energies in the range 1-100 keV, with a spatial resolution of $4° \times 4°$, and time resolution of approximately one minute. Each detector has a $50°$ field of view. However, each detector rotates over the course of 60 seconds. This gives the two combined detectors an effective field of view of $105°$. These detectors are quite sophisticated, and have a number of inbuilt systems designed to ensure that only ENAs are detected. Following the path of an incoming ENA, one first comes to the collimator, the outermost plate of which is labeled in the left hand diagram of figure 2.1.

The collimator is a series of thin, closely spaced, electrically biased plates. The electrical bias alternates between positive and negative, establishing a strong electric field perpendicular to the path of the ENAs. Being neutrally charged, ENAs are unaffected by this field; any ion or electron that happens to be following a similar path, however, will feel a strong force perpendicular to its motion, causing it to strike a collimator plate instead of entering the detector.

After passing through the collimator, one comes to the sensor aperture. This opening is capped with a transmission grating, which eliminates any high energy photons along this path while allowing most ENAs to pass. After the transmission grating, only ENAs should remain; all electrons, ions, and high energy photons will have been eliminated. After the transmission grating comes the start foil. ENAs pass through this ultra-thin carbon foil with minimal perturbation to their energies, releasing secondary electrons as the pass.

Following the start foil comes a drift region, ending in microchannel plate (MCP) detectors. There are two MCPs, one designed to record the impact of ENAs, which surrounds one designed to record the impact of the secondary electrons. These detectors record the one-dimensional position of the impacts, which gives information about the trajectory of the ENA. The drift region has a strong electric field, such that the secondary electrons are rapidly accelerated toward the central MCR detector. Along with recording the position of impact, this detector has a ”start anode”; that is, it records the time of impact of the secondary electrons as the start of a detection event. The ENAs are unaffected by the electric field, and continue on the same straight-line trajectory they had initially. Upon colliding with the MCP detector, the position of the impacting ENA is recorded. Additionally, this detector has a ”stop anode”. It records the time of impact as the end of an event. The difference between the start time and stop time is the time of flight. It is a matter of simple goemetry to calculate the distance travelled by the ENA; thus the ENA's speed is known. It should be noted that the electron-detecting MCP creates a blind spot in the center of the ENA-detecting MCP. The two ENA detectors on each spacecraft are carefully positioned so that each one's blind spot is covered by the other detector.

Chapter 3

Pressure Tensor

3.1 Equatorial Pressure Distribution

The previous chapter discussed how the TWINS ENA measurements can be used in conjunction with a geocoronal model to calculate an ion population. In order to calculate the magnetospheric ion-pressure driven currents, it is necessary to use the ion distribution and energies to calculate an ion pressure. This was first performed by Parker [1957], who solved the Vlasov equation assuming time-independence, and later clarified and expanded upon by Heinemann [1990] in Appendix A. This work used the simplifying assumptions of Chen et al. [1998, 1999], leading to the following formulations for the parallel and perpendicular components of the ion pressure at the equatorial plane:

$$P_{\perp}(s_0) = \int_0^{\infty} \int_0^{\pi/2} f(E, \alpha_0) sin^3(\alpha_0) d\alpha_0 dE \tag{3.1}$$

$$P_{\parallel}(s_0) = 2 \int_0^{\infty} \int_0^{\pi/2} f(E, \alpha_0) cos^2(\alpha_0) sin(\alpha_0) d\alpha_0 dE \tag{3.2}$$

In these equations, s_0 is the point of interest on the equatorial plane, α_0 is the pitch angle at the equatorial plane, and $f(E, \alpha_0)$ is the equatorial ion flux determined from TWINS measurements, which is a function of energy and pitch angle.

3.2 Pressure Off the Equatorial Plane

Once the equatorial ion pressure has been calculated, it is possible to determine the ion pressure at any point in the inner magnetosphere. How this calculation is performed depends on the ion pitch-angle distribution (PAD). In the case of an isotropic PAD, the calculation is particularly simple. In this case, $P_{\parallel} = P_{\perp}$, and the pressure remains constant along the magnetic field line. Thus, the pressure at any point can be found by simply tracing the magnetic

field at the point back to the equatorial plane. The pressure at this point, or any other point along this field line, is equal to the pressure at the mapped equatorial point.

The anisotropic PAD case is considerably more complicated. In this case, $P_{\parallel} \neq P_{\perp}$, and while both components of pressure map along magnetic field lines, they do not remain constant along them. Instead, they vary with distance along the magnetic field line.

$$P_{\perp}(s) = \int_0^{\infty} \int_0^{\pi/2} f(E, \alpha_0) sin^3(\alpha_0) d\alpha dE$$

$$P_{\parallel}(s) = 2 \int_0^{\infty} \int_0^{\pi/2} f(E, \alpha_0) cos^2(\alpha_0) sin(\alpha_0) d\alpha dE$$

In the above equations, s is the point of interest, s_0 is the point mapped from s along the magnetic field line to the equatorial plane, where the pressure is known, α_0 is the pitch angle at the point on the equatorial plane, s_0, and α is the pitch angle at point s. Note that the integral is taken over α rather than α_0. In order to perform this calculation, one must map the pitch angle along the magnetic field line. This mapping is governed by the following relations:

$$cos^2(\alpha_0) = 1 - \beta sin^2(\alpha)$$

$$sin^2(\alpha_0) = \beta sin^2(\alpha)$$

where $\beta = \frac{B(s_0)}{B(s)}$. The function $f(E, \alpha_0)$ is expanded into powers of $sin(\alpha_0)$, and thus may be transformed using the above relations.

$$P_{\perp}(s) = \int_0^{\infty} \int_0^{\pi/2} f(E, \alpha) \beta sin^3(\alpha) d\alpha dE \tag{3.3}$$

$$P_{\parallel}(s) = 2 \int_0^{\infty} \int_0^{\pi/2} f(E, \alpha)(1 - \beta sin^2(\alpha)) \beta sin(\alpha) d\alpha dE \tag{3.4}$$

These equations allow one to calculate the pressure at any point in the inner magnetosphere, provided the anisotropic pressure at the equatorial plane is known. Note that $B(s_0)$ is the magnetic field at the point on the equatorial plane connected by a magnetic field line to the point of interest. This will generally be near the point of minimum magnetic field. Thus, almost

always, $\frac{B(s_0)}{B(s)} < 1$, becoming very small approaching the ionosphere. Because this factor becomes smaller as one moves closer to the ionosphere, both parallel and perpendicular pressure tend to become smaller as one moves from the equatorial plane to the ionosphere.

Chapter 4

Magnetic Field

4.1 Dipole Field Approximation

In order to determine anything about the magnetosphere from TWINS observations, it is necessary to know the magnetic field in the inner magnetosphere, typically to $L = 8$. Because regions of small L are distorted by the solar wind substantially less than at higher L, a dipole approximation may be a reasonable assumption for the inner-most magnetosphere in some cases. Further, it is simple to calculate, and remains constant over time; the magnetic field can be described by: $\vec{B} = -B_0\left(\frac{R_E}{r}\right)^3\left[2cos\theta\hat{r} + sin\theta\hat{\theta}\right]$, where θ is the colatitude, and $B_0 = 3.12 \times 10^{-5}T$. Thus, it is substantially easier to determine and use than any other magnetic field model. For these reasons, much early work assumed a dipole field.

Unfortunately, this assumption does not hold up throughout the inner magnetosphere, becoming less accurate as L becomes larger, and is especially inaccurate under geomagnetic storm conditions. Under these conditions, the geomagnetic field becomes distorted away from a dipole field even at low L, particularly in the magnetotail, which can become quite stretched. This moves the oval at which a given L intersects with the ionosphere to lower latitudes. Further, a distorted field line travels a longer distance between the equatorial plane and the ionosphere. As will become apparent in the next section, this typically will increase the magnitude of any field aligned current along the line.

4.2 Tsyganenko Magnetic Field Model

Nikolai Tsyganenko has spent his career developing a variety of magnetic field models. In conjunction with Mikhail Sitnov, a best fit model was developed that employs a variety of in-situ measurements from spacecraft to estimate the magnetic field in the magnetosphere under geomagnetic storm conditions. This model was published in 2005, and will thus be

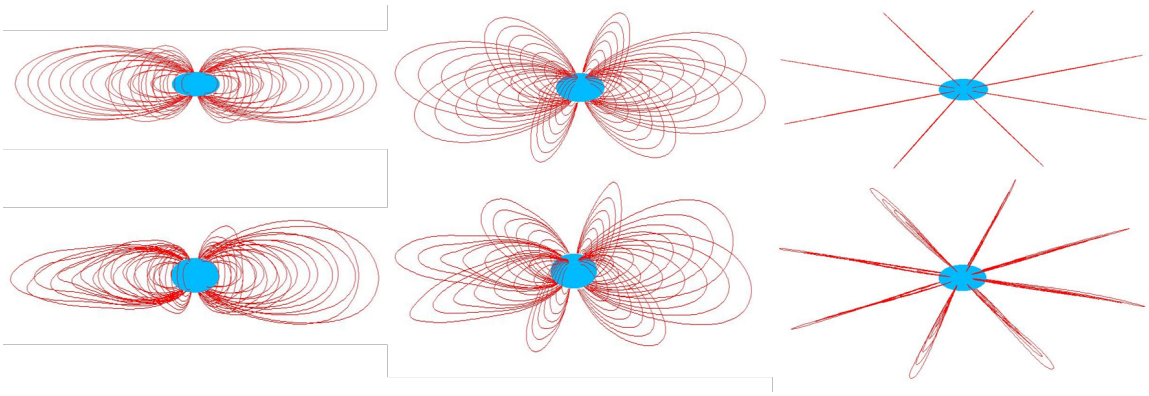

Figure 4.1: A comparison of the TS05 magnetic field with the dipole approximation at 08:00 UT on 1 June 2013. Top Row: Dipole magnetic field. Bottom Row: TS05 magnetic field. Left Column: View from equatorial plane. Center Column: View from 45 degrees north latitude. Right Column: View from above north magnetic pole. The Sun is to the right in these images.

referred to in this work as the TS05 model [Tsyganenko and Sitnov 2005]. While many earlier magnetic field models had calculated the magnetospheric magnetic field based on Earth-based measurements and assuming a current-free magnetosphere, in reality there are currents in the magnetosphere. These currents, of course, produced magnetic fields that interact with the both the solar wind field and the inherent field of Earth. This makes the magnetospheric magnetic field substantially more complicated than a current-free model would suggest.

Modeling such a magnetic field accurately requires a great deal of information. The TS05 model uses magnetometer data from a large number of spacecraft, occupying a wide range of positions in the magnetosphere. This allows estimates to be made of the various magnetospheric currents. In addition to these currents, the TS05 model uses measurements of the IMF, both magnitude and direction, and adjusts for the orientation of the Earth's magnetic field relative to the IMF orientation.

A comparison of the TS05 and dipole fields under geomagnetic storm conditions can be seen in figure 4.1. The magnetic fields in the dipole have no dependence on the azimuthal position, while the TS05 magnetic field lines are not symmetric. Rather, the magnetic field lines in the TS05 model are compressed on the dayside, bulging further from the equatorial plane and crossing the equatorial plane closer to the Earth, and stretched on the nightside, crossing the equatorial plane further from the Earth. A careful look will reveal that the nightside field lines do not all reach their furthest point from the Earth at the equatorial plane; they do not

even reach this point on the same plane. The view from over the pole also reveals an important difference. The dipole magnetic field looks like a set of spokes radiating out from the Earth. There is absolutely no variance along the field lines in the azimuthal direction. The TS05 field, on the other hand, does have azimuthal variance along field lines. The visibility of concentric field lines indicates that these lines have a small, but noticeable, azimuthal dependence.

The differences between these models have important implications. Further, the differences increase as one moves radially away from Earth. Because, as will be seen, the calculated FACs depend on the length of the magnetic field lines, the TS05 field will produce far more accurate results than the dipole model, particularly at high latitudes and on the nightside.

4.3 Surface of Minimum Magnetic Field

As will be seen in section 5.3, the calculation of the FACs depends on an integration over the length of magnetic field lines, beginning at the point of minimum magnetic field along the line. In the dipole approximation this is simple; the point of minimum magnetic field always lies on the equatorial plane. Roelof et al. [1989, 2004] used the assumptions of both PAD isotropy and a dipole magnetic field to calculate magnetospheric currents. Under these assumptions, surfaces of constant presssure extend from the equatorial plane to both northern and southern ionospheres along magnetic field lines. The lines of current in figure 4.2 lie along these surfaces; in this case, the surface corresponding to P=0.8 nPa. Each line of current lies at the intersection of the surface of constant pressure and a surface of constant flux tube volume, where the flux tube volume is: $V_{ft}(s) = \int_{s_0}^{s} \frac{ds'}{B} ds'$. Each line of current carries 2800 A.

Most of the current lines in figure 4.2 intersect the northern hemisphere of the Earth at moderately high latitude. This requires the current loop to be closed through the ionosphere. Currents near the equatorial plane, however, will never reach the ionosphere. These currents are closed loops, lying near the equatorial plane for as long as the conditions producing them persist.

While the dipole model ensures that the minimum magnetic field always lies on the equatorial plane, in more realistic models, including the Tsyganenko [2005] model used in this

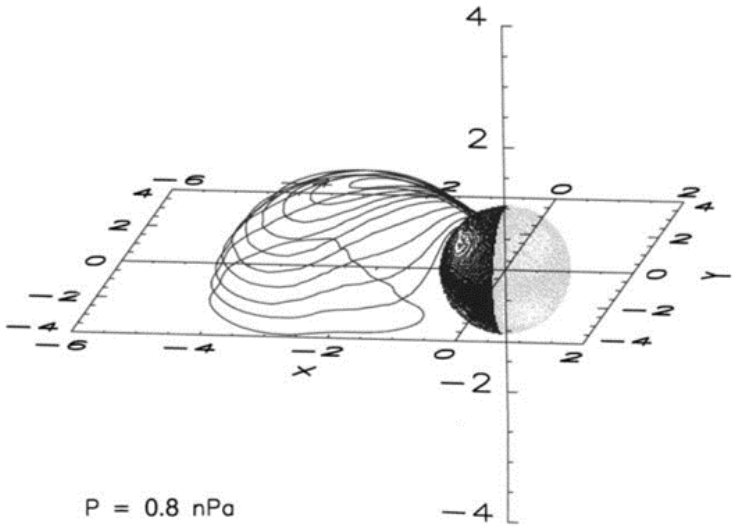

Figure 4.2: Lines of constant current in nightside magnetosphere, assuming isotropic PAD and dipole magnetic field. Figure 2 of Roelof et al. 2004.

work, this is not necessarily the case. Further, the collection of minimum magnetic field points for the entire magnetosphere does not necessarily lie in any plane. Rather, in general they form a two dimensional, non-planar surface. The non-planar nature of this surface has important effects. Because there is no field aligned component of the current at the point of minimum magnetic field along a field line, at this point all current is perpendicular to the field line. In the case of a dipole magnetic field, this means that any current on the equatorial plane - which is the plane of minimum magnetic field - will stay on the equatorial plane. It will be trapped there forever. Further, currents in one hemisphere can never cross into the other; they may approach the equatorial plane, but may never reach it, let alone cross.

This is not true for more realistic magnetic fields. Like the dipole case, a current on the surface of minimum magnetic field will be entirely perpendicular to the magnetic field line. However, the surface is not necessarily perpendicular to the magnetic field line. This means the current may move off the surface of minimum magnetic field, at which point it may acquire some field aligned component. Thus, when using a field model like TS05, currents may not only reach the minimmum magnetic field surface, they may cross it. This means the two hemispheres are not strictly separated as they are in the dipole case. This will be shown in more detail in chapter 8.

Chapter 5

Field Aligned Current Derivation

5.1 Ampere's Law, Charge Conservation, and Pressure

This work will be done in the quasi-static approximation, assuming charge conservation, quasi-neutrality, and gyrotropy. Given these assumptions, the following equations may be written:

$$\boldsymbol{\nabla} \cdot \vec{B} = 0 \tag{5.1}$$

$$\boldsymbol{\nabla} \times \vec{B} = \mu_0 \vec{J} \tag{5.2}$$

$$\boldsymbol{\nabla} \cdot \vec{J} = 0 \tag{5.3}$$

$$\boldsymbol{\nabla} \cdot P = \vec{J} \times \vec{B} \tag{5.4}$$

The pressure must be written as a tensor, such that:

$$\begin{aligned} P &= P_\perp \hat{I} + \left(P_\parallel - P_\perp\right) \frac{\vec{B}\vec{B}}{B^2} \\ &= P_\perp \hat{I} + \frac{\chi}{\mu_0} \vec{B}\vec{B} \end{aligned} \tag{5.5}$$

where $\chi = \frac{\mu_0(P_\parallel - P_\perp)}{B^2}$. χ is a dimensionless quantity related to both plasma beta and anisotropy. Plasma beta relates the plasma pressure to the magnetic pressure, $\beta = \frac{P}{P_{mag}}$, where $P_{mag} = \frac{B^2}{2\mu_0}$. This work defines anisotropy as: $A = \frac{P_\perp - P_\parallel}{P_\perp + P_\parallel} = \frac{P_\perp - P_\parallel}{P}$. Therefore, we may write:

$$\chi = -\frac{1}{2} A\beta \tag{5.6}$$

$$
\begin{aligned}
\boldsymbol{\nabla}\cdot P &= \boldsymbol{\nabla}\cdot\left(P_{\perp}\hat{I}\right)+\frac{1}{\mu_0}\boldsymbol{\nabla}\cdot\chi\vec{B}\vec{B}\\
&= P_{\perp}\boldsymbol{\nabla}\cdot\hat{I}+\hat{I}\cdot\boldsymbol{\nabla}P_{\perp}+\left(\boldsymbol{\nabla}\cdot\left(\frac{\chi}{\mu_0}\vec{B}\right)\right)\vec{B}+\left(\frac{\chi}{\mu_0}\vec{B}\cdot\boldsymbol{\nabla}\right)\vec{B}\\
&= \boldsymbol{\nabla}P_{\perp}+\left[\frac{\chi}{\mu_0}\boldsymbol{\nabla}\cdot\vec{B}+\vec{B}\cdot\boldsymbol{\nabla}\frac{\chi}{\mu_0}\right]\vec{B}+\frac{\chi}{\mu_0}\left(\vec{B}\cdot\boldsymbol{\nabla}\right)\vec{B}\\
&= \boldsymbol{\nabla}P_{\perp}+\left(\vec{B}\cdot\boldsymbol{\nabla}\frac{\chi}{\mu_0}\right)\vec{B}+\frac{\chi}{\mu_0}\left[\left(\boldsymbol{\nabla}\vec{B}\right)\cdot\vec{B}-\vec{B}\times\left(\boldsymbol{\nabla}\times\vec{B}\right)\right]\\
&= \boldsymbol{\nabla}P_{\perp}+\left(\vec{B}\cdot\boldsymbol{\nabla}\frac{\chi}{\mu_0}\right)\vec{B}+\frac{\chi}{\mu_0}\left[\boldsymbol{\nabla}\frac{B^2}{2}-\mu_0\vec{B}\times\vec{J}\right]
\end{aligned}
$$

From equation 5.4,

$$
\vec{J}\times\vec{B}=\boldsymbol{\nabla}P_{\perp}+\left(\vec{B}\cdot\boldsymbol{\nabla}\frac{\chi}{\mu_0}\right)\vec{B}+\frac{\chi}{\mu_0}\boldsymbol{\nabla}\frac{B^2}{2}+\chi\vec{J}\times\vec{B}
$$

$$
\vec{J}\times\vec{B}=\frac{\boldsymbol{\nabla}P_{\perp}+\left(\vec{B}\cdot\boldsymbol{\nabla}\frac{\chi}{\mu_0}\right)\vec{B}+\frac{\chi}{\mu_0}\boldsymbol{\nabla}\frac{B^2}{2}}{1-\chi} \tag{5.7}
$$

Equation 5.7 is equivalent to equation 6 in Heinemann [1990]. We may define a vector $\vec{F}=\frac{\boldsymbol{\nabla}P_{\perp}+\left(\vec{B}\cdot\boldsymbol{\nabla}\frac{\chi}{\mu_0}\right)\vec{B}+\frac{\chi}{\mu_0}\boldsymbol{\nabla}\frac{B^2}{2}}{1-\chi}$, where $\vec{F}$ is the force per unit volume of plasma.

5.2 Perpendicular Current Density

Crossing both sides of equation 5.7 with $\vec{B}$ yields:

$$
\vec{B}\times\left(\vec{J}\times\vec{B}\right)=\vec{B}\times\vec{F}
$$

Considering the left-hand side of this equation, we find:

$$
\begin{aligned}
\vec{B}\times\left(\vec{J}\times\vec{B}\right) &= \left(\vec{B}\cdot\vec{B}\right)\vec{J}-\left(\vec{B}\cdot\vec{J}\right)\vec{B}\\
&= B^2\vec{J}-BJ_{\parallel}\vec{B}\\
&= B^2\left(\vec{J_{\parallel}}+\vec{J_{\perp}}\right)-B^2\vec{J_{\parallel}}\\
&= B^2\vec{J_{\perp}}
\end{aligned}
$$

Thus,

$$\vec{J_\perp} = \frac{\vec{B} \times \vec{F}}{B^2} = \frac{\vec{B} \times \left(\boldsymbol{\nabla} P_\perp + \left(\vec{B} \cdot \boldsymbol{\nabla} \frac{\chi}{\mu_0} \right) \vec{B} + \frac{\chi}{\mu_0} \boldsymbol{\nabla} \frac{B^2}{2} \right)}{B^2 \left(1 - \chi\right)}$$

$$= \frac{\vec{B} \times \boldsymbol{\nabla} P_\perp + \left(\vec{B} \cdot \boldsymbol{\nabla} \frac{\chi}{\mu_0} \right) \vec{B} \times \vec{B} + \frac{\chi}{\mu_0} \vec{B} \times \boldsymbol{\nabla} \frac{B^2}{2}}{B^2 \left(1 - \chi\right)}$$

$$\vec{J_\perp} = \frac{\vec{B} \times \boldsymbol{\nabla} P_\perp + \frac{\chi B}{\mu_0} \vec{B} \times \boldsymbol{\nabla} B}{B^2 \left(1 - \chi\right)} \tag{5.8}$$

Equation 5.8 gives the component of the current density perpendicular to the magnetic field in the general case. If, however, the pitch-angle distribution of the ions is isotropic, equation 5.8 may be simplified. In this case, $P_\parallel = P_\perp$ and $\chi = 0$. Defining $P = P_\perp + P_\parallel$, the perpendicular current density in the case of isotropic PAD may be written:

$$\vec{J_\perp} = \frac{\vec{B} \times \boldsymbol{\nabla} \frac{P}{2}}{B^2} \tag{5.9}$$

5.3 Parallel Current Density

To find the field aligned component of the current density, we will employ charge conservation, equation 5.3.

$$\boldsymbol{\nabla} \cdot \vec{J} = \boldsymbol{\nabla} \cdot \left(\vec{J_\parallel} + \vec{J_\perp} \right) = \boldsymbol{\nabla} \cdot \vec{J_\parallel} + \boldsymbol{\nabla} \cdot \vec{J_\perp} = 0$$

$$\begin{aligned}
\boldsymbol{\nabla} \cdot \vec{J_\parallel} &= -\boldsymbol{\nabla} \cdot \vec{J_\perp} \\
&= -\boldsymbol{\nabla} \cdot \frac{\vec{B} \times \vec{F}}{B^2} \\
&= -\frac{1}{B^2} \boldsymbol{\nabla} \cdot \left(\vec{B} \times \vec{F} \right) - \left(\vec{B} \times \vec{F} \right) \cdot \boldsymbol{\nabla} \frac{1}{B^2} \\
&= -\frac{\vec{F} \cdot \boldsymbol{\nabla} \times \vec{B} - \vec{B} \cdot \boldsymbol{\nabla} \times \vec{F}}{B^2} - \left(\vec{B} \times \vec{F} \right) \cdot \left(-\frac{2}{B^3} \boldsymbol{\nabla} B \right) \\
&= \frac{\vec{B} \cdot \boldsymbol{\nabla} \times \vec{F} - \mu_0 \vec{F} \cdot \vec{J}}{B^2} + \frac{2}{B} \frac{\vec{B} \times \vec{F}}{B^2} \cdot \boldsymbol{\nabla} B \\
&= \frac{\vec{B} \cdot \boldsymbol{\nabla} \times \vec{F}}{B^2} - \frac{\mu_0 \vec{F} \cdot \vec{J_\parallel}}{B^2} - \frac{\mu_0 \vec{F} \cdot \vec{J_\perp}}{B^2} + \frac{2}{B} \vec{J_\perp} \cdot \boldsymbol{\nabla} B \\
&= \frac{2 \vec{J_\perp} \cdot \boldsymbol{\nabla} B}{B} + \frac{\vec{B} \cdot \boldsymbol{\nabla} \times \vec{F}}{B^2} - \frac{\mu_0 \vec{F} \cdot \vec{J_\parallel}}{B^2} - \frac{\mu_0 \vec{F} \cdot \vec{J_\perp}}{B^2}
\end{aligned}$$

$$\vec{F} \cdot \vec{J_\perp} = \vec{F} \cdot \left(\frac{\vec{B} \times \vec{F}}{B^2} \right) = 0$$

$$\begin{aligned} \vec{F} \cdot \vec{J_\parallel} &= \frac{\boldsymbol{\nabla} P_\perp + \left(\vec{B} \cdot \boldsymbol{\nabla} \frac{\chi}{\mu_0} \right) \vec{B} + \frac{\chi}{\mu_0} \boldsymbol{\nabla} \frac{B^2}{2}}{1 - \chi} \cdot \frac{J_\parallel}{B} \vec{B} \\ &= \left(\vec{J} \times \vec{B} \right) \cdot \left(\frac{J_\parallel}{B} \right) \vec{B} = 0 \end{aligned}$$

This gives:

$$\boldsymbol{\nabla} \cdot \vec{J_\parallel} = \frac{2 \vec{J_\perp} \cdot \boldsymbol{\nabla} B}{B} + \frac{\vec{B} \cdot \boldsymbol{\nabla} \times \vec{F}}{B^2}$$

Examining the left-hand side:

$$\begin{aligned} \boldsymbol{\nabla} \cdot \vec{J_\parallel} &= \boldsymbol{\nabla} \cdot \frac{J_\parallel}{B} \vec{B} \\ &= \frac{J_\parallel}{B} \boldsymbol{\nabla} \cdot \vec{B} + \vec{B} \cdot \boldsymbol{\nabla} \frac{J_\parallel}{B} \\ &= B \frac{\partial}{\partial s} \left(\frac{J_\parallel}{B} \right) \end{aligned}$$

Thus,

$$\frac{\partial}{\partial s} \left(\frac{J_\parallel}{B} \right) = \frac{1}{B^2} \left[2 \vec{J_\perp} \cdot \boldsymbol{\nabla} B + \frac{\vec{B} \cdot \left(\boldsymbol{\nabla} \times \vec{F} \right)}{B} \right] \tag{5.10}$$

This is equivalent to equation 7 in Vasyliunas 1984. It is necessary to expand $\boldsymbol{\nabla} \times \vec{F}$ in order to solve for $J_\parallel$.

$$
\begin{aligned}
\boldsymbol{\nabla} \times \vec{F} &= \boldsymbol{\nabla} \times \left(\frac{\boldsymbol{\nabla} P_{\perp} + \left(\vec{B} \cdot \boldsymbol{\nabla} \frac{\chi}{\mu_0} \right) \vec{B} + \frac{\chi}{\mu_0} \boldsymbol{\nabla} \frac{B^2}{2}}{1 - \chi} \right) \\
&= \left(\frac{1}{1-\chi} \right) \boldsymbol{\nabla} \times \left(\boldsymbol{\nabla} P_{\perp} + \left(\vec{B} \cdot \boldsymbol{\nabla} \frac{\chi}{\mu_0} \right) \vec{B} + \frac{\chi}{\mu_0} \boldsymbol{\nabla} \frac{B^2}{2} \right) \\
&\quad + \boldsymbol{\nabla} \left(\frac{1}{1-\chi} \right) \times \left(\boldsymbol{\nabla} P_{\perp} + \left(\vec{B} \cdot \boldsymbol{\nabla} \frac{\chi}{\mu_0} \right) \vec{B} + \frac{\chi}{\mu_0} \boldsymbol{\nabla} \frac{B^2}{2} \right) \\
&= \left(\frac{1}{1-\chi} \right) \left[\left(\vec{B} \cdot \boldsymbol{\nabla} \frac{\chi}{\mu_0} \right) \boldsymbol{\nabla} \times \vec{B} + \boldsymbol{\nabla} \left(\vec{B} \cdot \boldsymbol{\nabla} \frac{\chi}{\mu_0} \right) \times \vec{B} + \boldsymbol{\nabla} \frac{\chi}{\mu_0} \times \boldsymbol{\nabla} \frac{B^2}{2} \right] \\
&\quad + \left(\frac{\boldsymbol{\nabla} \chi}{(1-\chi)^2} \right) \times \left[\boldsymbol{\nabla} P_{\perp} + \left(\vec{B} \cdot \boldsymbol{\nabla} \frac{\chi}{\mu_0} \right) \vec{B} \frac{\chi}{\mu_0} \boldsymbol{\nabla} \frac{B^2}{2} \right] \\
&= \left(\frac{1}{1-\chi} \right) \left[\left(\vec{B} \cdot \boldsymbol{\nabla} \frac{\chi}{\mu_0} \right) \boldsymbol{\nabla} \times \vec{B} + \boldsymbol{\nabla} \left(\vec{B} \cdot \boldsymbol{\nabla} \frac{\chi}{\mu_0} \right) \times \vec{B} + \boldsymbol{\nabla} \frac{\chi}{\mu_0} \times \boldsymbol{\nabla} \frac{B^2}{2} \right. \\
&\quad \left. + \frac{\boldsymbol{\nabla} \chi \times \boldsymbol{\nabla} P_{\perp}}{1-\chi} + \left(\frac{\vec{B} \cdot \boldsymbol{\nabla} \frac{\chi}{\mu_0}}{1-\chi} \right) \boldsymbol{\nabla} \chi \times \vec{B} + \left(\frac{\chi}{\mu_0 (1-\chi)} \right) \boldsymbol{\nabla} \chi \times \boldsymbol{\nabla} \frac{B^2}{2} \right] \\
&= \left(\frac{1}{1-\chi} \right) \left[\left(\vec{B} \cdot \boldsymbol{\nabla} \chi \right) \vec{J} + \frac{1}{\mu_0} \boldsymbol{\nabla} \left(\vec{B} \cdot \boldsymbol{\nabla} \chi \right) \times \vec{B} + \frac{B}{\mu_0} \boldsymbol{\nabla} \chi \times \boldsymbol{\nabla} B \right. \\
&\quad + \frac{1}{1-\chi} \left(\boldsymbol{\nabla} \chi \times \boldsymbol{\nabla} P_{\perp} + \left(\frac{\vec{B} \cdot \boldsymbol{\nabla} \chi}{\mu_0} \right) \boldsymbol{\nabla} \chi \times \vec{B} \right. \\
&\quad \left. \left. + \left(\frac{\chi B}{\mu_0 (1-\chi)} \right) \boldsymbol{\nabla} \chi \times \boldsymbol{\nabla} B \right) \right]
\end{aligned}
$$

Substituting this result into the $\frac{\vec{B}}{B} \cdot \left(\boldsymbol{\nabla} \times \vec{F} \right)$ term from equation 5.10 yields:

$$\begin{aligned}
\frac{\vec{B}}{B} \cdot \left(\boldsymbol{\nabla} \times \vec{F} \right) &= \frac{1}{B\left(1-\chi\right)} \Bigg[\left(\vec{B} \cdot \boldsymbol{\nabla} \chi \right) \vec{B} \cdot \vec{J} + \frac{1}{\mu_0} \vec{B} \cdot \left(\boldsymbol{\nabla} \left(\vec{B} \cdot \boldsymbol{\nabla} \chi \right) \times \vec{B} \right) \\
&\quad + \frac{B}{\mu_0} \vec{B} \cdot \left(\boldsymbol{\nabla} \chi \times \boldsymbol{\nabla} B \right) + \frac{1}{1-\chi} \Bigg(\vec{B} \cdot \left(\boldsymbol{\nabla} \chi \times \boldsymbol{\nabla} P_{\perp} \right) \\
&\quad + \left(\frac{\vec{B} \cdot \boldsymbol{\nabla} \chi}{\mu_0} \right) \vec{B} \cdot \left(\boldsymbol{\nabla} \chi \times \vec{B} \right) + \left(\frac{\chi B}{\mu_0 \left(1-\chi\right)} \right) \vec{B} \cdot \left(\boldsymbol{\nabla} \chi \times \boldsymbol{\nabla} B \right) \Bigg) \Bigg] \\
&= \frac{1}{B\left(1-\chi\right)} \Bigg[\left(\vec{B} \cdot \boldsymbol{\nabla} \chi \right) B J_{\parallel} + 0 + \frac{B^2}{\mu_0} \left(\boldsymbol{\nabla} \chi \times \boldsymbol{\nabla} B \right) \cdot \hat{s} \\
&\quad + \frac{B}{1-\chi} \left(\boldsymbol{\nabla} \chi \times \boldsymbol{\nabla} P_{\perp} \right) \cdot \hat{s} + 0 + \frac{\chi B^2}{\mu_0 \left(1-\chi\right)} \left(\boldsymbol{\nabla} \chi \times \boldsymbol{\nabla} B \right) \cdot \hat{s} \Bigg] \\
&= \frac{B \left(\vec{B} \cdot \boldsymbol{\nabla} \chi \right)}{1-\chi} \left(\frac{J_{\parallel}}{B} \right) + \frac{B}{\mu_0 \left(1-\chi\right)} \left(1 + \frac{\chi}{1-\chi} \right) \left(\boldsymbol{\nabla} \chi \times \boldsymbol{\nabla} B \right) \cdot \hat{s} \\
&\quad + \frac{\left(\boldsymbol{\nabla} \chi \times \boldsymbol{\nabla} P_{\perp} \right) \cdot \hat{s}}{\left(1-\chi\right)^2}
\end{aligned}$$

where $\hat{s}$ is the unit vector in the direction of the magnetic field. Substituting this result into equation 5.10 yields a differential equation for $J_{\parallel}$.

$$\begin{aligned}
\frac{\partial}{\partial s} \left(\frac{J_{\parallel}}{B} \right) &= \frac{1}{B^2} \Bigg[2 \left(\frac{\vec{B} \times \boldsymbol{\nabla} P_{\perp} + \frac{\chi B}{\mu_0} \vec{B} \times \boldsymbol{\nabla} B}{B^2 \left(1-\chi\right)} \right) \cdot \boldsymbol{\nabla} B + \frac{B \left(\vec{B} \cdot \boldsymbol{\nabla} \chi \right)}{1-\chi} \left(\frac{J_{\parallel}}{B} \right) \\
&\quad + \frac{B}{\mu_0 \left(1-\chi\right)} \left(1 + \frac{\chi}{1-\chi} \right) \left(\boldsymbol{\nabla} \chi \times \boldsymbol{\nabla} B \right) \cdot \hat{s} + \frac{\left(\boldsymbol{\nabla} \chi \times \boldsymbol{\nabla} P_{\perp} \right) \cdot \hat{s}}{\left(1-\chi\right)^2} \Bigg] \\
&= \frac{2}{B^4 \left(1-\chi\right)} \left(\boldsymbol{\nabla} P_{\perp} \times \boldsymbol{\nabla} B \right) \cdot \vec{B} + 0 + \frac{\vec{B} \cdot \boldsymbol{\nabla} \chi}{B\left(1-\chi\right)} \left(\frac{J_{\parallel}}{B} \right) \\
&\quad + \frac{\left(\boldsymbol{\nabla} \chi \times \boldsymbol{\nabla} B \right) \cdot \hat{s}}{\mu_0 B \left(1-\chi\right)^2} + \frac{\left(\boldsymbol{\nabla} \chi \times \boldsymbol{\nabla} P_{\perp} \right) \cdot \hat{s}}{B^2 \left(1-\chi\right)^2} \\
&= \frac{2 \left(\boldsymbol{\nabla} P_{\perp} \times \boldsymbol{\nabla} B \right) \cdot \hat{s}}{B^3 \left(1-\chi\right)} + \frac{\frac{\partial \chi}{\partial s}}{1-\chi} \left(\frac{J_{\parallel}}{B} \right) + \frac{\left(\boldsymbol{\nabla} \chi \times \boldsymbol{\nabla} B \right) \cdot \hat{s}}{\mu_0 B \left(1-\chi\right)^2} \\
&\quad + \frac{\left(\boldsymbol{\nabla} \chi \times \boldsymbol{\nabla} P_{\perp} \right) \cdot \hat{s}}{B^2 \left(1-\chi\right)^2}
\end{aligned}$$

$$\frac{\partial}{\partial s}\left(\frac{J_{\parallel}}{B}\right)-\frac{1}{1-\chi}\frac{\partial\chi}{\partial s}\left(\frac{J_{\parallel}}{B}\right)=\frac{2\left(\boldsymbol{\nabla}P_{\perp}\times\boldsymbol{\nabla}B\right)\cdot\hat{s}}{B^{3}\left(1-\chi\right)}+\frac{\left(\boldsymbol{\nabla}\chi\times\boldsymbol{\nabla}B\right)\cdot\hat{s}}{\mu_{0}B\left(1-\chi\right)^{2}}+\frac{\left(\boldsymbol{\nabla}\chi\times\boldsymbol{\nabla}P_{\perp}\right)\cdot\hat{s}}{B^{2}\left(1-\chi\right)^{2}} \tag{5.11}$$

The solution to this differential equation is:

$$\left(\frac{J_{\parallel}}{B}\right)exp\left(-\int\frac{1}{1-\chi}\frac{\partial\chi}{\partial s}ds\right)=\int\left[\frac{2\left(\boldsymbol{\nabla}P_{\perp}\times\boldsymbol{\nabla}B\right)\cdot\hat{s}}{B^{3}\left(1-\chi\right)}+\frac{\left(\boldsymbol{\nabla}\chi\times\boldsymbol{\nabla}B\right)\cdot\hat{s}}{\mu_{0}B\left(1-\chi\right)^{2}}+\frac{\left(\boldsymbol{\nabla}\chi\times\boldsymbol{\nabla}P_{\perp}\right)\cdot\hat{s}}{B^{2}\left(1-\chi\right)^{2}}\right]exp\left(-\int\frac{1}{1-\chi}\frac{\partial\chi}{\partial s}ds\right)ds+C$$

$$\begin{aligned}\left(1-\chi\right)\left(\frac{J_{\parallel}}{B}\right)&=\int\left(1-\chi\right)\left[\frac{2\left(\boldsymbol{\nabla}P_{\perp}\times\boldsymbol{\nabla}B\right)\cdot\hat{s}}{B^{3}\left(1-\chi\right)}+\frac{\left(\boldsymbol{\nabla}\chi\times\boldsymbol{\nabla}B\right)\cdot\hat{s}}{\mu_{0}B\left(1-\chi\right)^{2}}+\frac{\left(\boldsymbol{\nabla}\chi\times\boldsymbol{\nabla}P_{\perp}\right)\cdot\hat{s}}{B^{2}\left(1-\chi\right)^{2}}\right]ds+C\\&=\int\left[\frac{2\left(\boldsymbol{\nabla}P_{\perp}\times\boldsymbol{\nabla}B\right)\cdot\hat{s}}{B^{3}}+\frac{\left(\boldsymbol{\nabla}\chi\times\boldsymbol{\nabla}B\right)\cdot\hat{s}}{\mu_{0}B\left(1-\chi\right)}+\frac{\left(\boldsymbol{\nabla}\chi\times\boldsymbol{\nabla}P_{\perp}\right)\cdot\hat{s}}{B^{2}\left(1-\chi\right)}\right]ds+C\end{aligned}$$

$\hat{s}$ has already been defined as the unit vector in the direction of the magnetic field, and s represents the path of a magnetic field line. The point along a field line at which the magnetic field is minimum shall be called s_1. $J_{\parallel}(s_1)=0$, which allows C to be found.

$$0=\left[\int\left[\frac{2\left(\boldsymbol{\nabla}P_{\perp}\times\boldsymbol{\nabla}B\right)\cdot\hat{s}}{B^{3}}+\frac{\left(\boldsymbol{\nabla}\chi\times\boldsymbol{\nabla}B\right)\cdot\hat{s}}{\mu_{0}B\left(1-\chi\right)}+\frac{\left(\boldsymbol{\nabla}\chi\times\boldsymbol{\nabla}P_{\perp}\right)\cdot\hat{s}}{B^{2}\left(1-\chi\right)}\right]ds\right]_{s_1}+C$$

$$C=-\left[\int\left[\frac{2\left(\boldsymbol{\nabla}P_{\perp}\times\boldsymbol{\nabla}B\right)\cdot\hat{s}}{B^{3}}+\frac{\left(\boldsymbol{\nabla}\chi\times\boldsymbol{\nabla}B\right)\cdot\hat{s}}{\mu_{0}B\left(1-\chi\right)}+\frac{\left(\boldsymbol{\nabla}\chi\times\boldsymbol{\nabla}P_{\perp}\right)\cdot\hat{s}}{B^{2}\left(1-\chi\right)}\right]ds\right]_{s_1}$$

Now consider a point along the same magnetic field line at which we would like to find $J_{\parallel}$. This point will be called s_2.

$$
\begin{aligned}
(1-\chi(s_2))\left(\frac{J_\parallel(s_2)}{B(s_2)}\right) &= \Bigg[\int\Bigg[\frac{2\left(\boldsymbol{\nabla}P_\perp\times\boldsymbol{\nabla}B\right)\cdot\hat{s}}{B^3}+\frac{\left(\boldsymbol{\nabla}\chi\times\boldsymbol{\nabla}B\right)\cdot\hat{s}}{\mu_0 B\left(1-\chi\right)} \\
&\quad+\frac{\left(\boldsymbol{\nabla}\chi\times\boldsymbol{\nabla}P_\perp\right)\cdot\hat{s}}{B^2\left(1-\chi\right)}\Bigg]ds\Bigg]_{s_2} \\
&\quad-\Bigg[\int\Bigg[\frac{2\left(\boldsymbol{\nabla}P_\perp\times\boldsymbol{\nabla}B\right)\cdot\hat{s}}{B^3}+\frac{\left(\boldsymbol{\nabla}\chi\times\boldsymbol{\nabla}B\right)\cdot\hat{s}}{\mu_0 B\left(1-\chi\right)} \\
&\quad+\frac{\left(\boldsymbol{\nabla}\chi\times\boldsymbol{\nabla}P_\perp\right)\cdot\hat{s}}{B^2\left(1-\chi\right)}\Bigg]ds\Bigg]_{s_1} \\
&= \int_{s_1}^{s_2}\Bigg[\frac{2\left(\boldsymbol{\nabla}P_\perp\times\boldsymbol{\nabla}B\right)\cdot\hat{s}}{B^3}+\frac{\left(\boldsymbol{\nabla}\chi\times\boldsymbol{\nabla}B\right)\cdot\hat{s}}{\mu_0 B\left(1-\chi\right)} \\
&\quad+\frac{\left(\boldsymbol{\nabla}\chi\times\boldsymbol{\nabla}P_\perp\right)\cdot\hat{s}}{B^2\left(1-\chi\right)}\Bigg]ds
\end{aligned}
$$

$$
\begin{aligned}
J_\parallel(s_2) = \frac{B(s_2)}{1-\chi(s_2)}\int_{s_1}^{s_2}\Bigg[&\frac{2\left(\boldsymbol{\nabla}P_\perp\times\boldsymbol{\nabla}B\right)\cdot\hat{s}}{B^3}+\frac{\left(\boldsymbol{\nabla}\chi\times\boldsymbol{\nabla}B\right)\cdot\hat{s}}{\mu_0 B\left(1-\chi\right)} \\
&+\frac{\left(\boldsymbol{\nabla}\chi\times\boldsymbol{\nabla}P_\perp\right)\cdot\hat{s}}{B^2\left(1-\chi\right)}\Bigg]ds
\end{aligned}
\tag{5.12}
$$

In the case of an isotropic pitch-angle distribution, $\chi = 0$ and $P_\perp = \frac{P}{2}$, as discussed previously. In this case, $J_\parallel$ reduces to:

$$
J_\parallel(s_2) = B(s_2)\int_{s_1}^{s_2}\frac{\left(\boldsymbol{\nabla}P\times\boldsymbol{\nabla}B\right)\cdot\hat{s}}{B^3}ds \tag{5.13}
$$

Chapter 6

Results

6.1 CIR Storm 01 June 2013

This work will focus on the geomagnetic storm that occurred on 01 June 2013. Figures 6.1 and 6.2, below, plot a variety of parameters compiled by OMNIWeb Plus, a service of Goddard Space Flight Center's Space Physics Data Facility. OMNIWeb Plus enables access to a wide variety of heliospheric and magnetospheric parameters at any given time. These parameters are compiled from measurements made by a wide variety of spacecraft and made available for use by the scientific community. This service enables the measurements from many different missions to be accessed in one location. The High Resolution OMNI plots used here may be reproduced at https://omniweb.gsfc.nasa.gov/form/omni_min.html. Each plotted parameter will be discussed below. The green highlighted regions in figure 6.2 are times during which TWINS measurements were sufficient to yield results for the ion distribution functions; thus these times are of particular interest in this work.

The top panel of figure 6.2 plots the average magntitude of the interplanetary magnetic field (IMF), time-shifted by OMNI to the Earth's bow shock nose, in nano-Teslas. As can be seen, the magnitude of the IMF increases sharply beginning at 00:00 UT, reaching 20 nT by 01:00 UT. It remains near this level until approximately 06:30 UT, declines slightly over the next 1.5 hours, then sharply increases to greater than 20 nT once again. At approximately 08:00 UT, the IMF magnitude begins a gradual decline until it is approximately half the magnitude at the peak by 13:00 UT, where it remains until the following day. By 04:00 UT on 02 June 2013, the IMF has returned to the pre-storm level of less than 5 nT.

The next panels show components of the magnetic field in Geocentric Solar Magnetic (GSM) coordinates. GSM coordinates are a Cartesian set of coordinates with the center of the Earth at the origin. The x-axis lies along the line connecting the Earth to the Sun, with

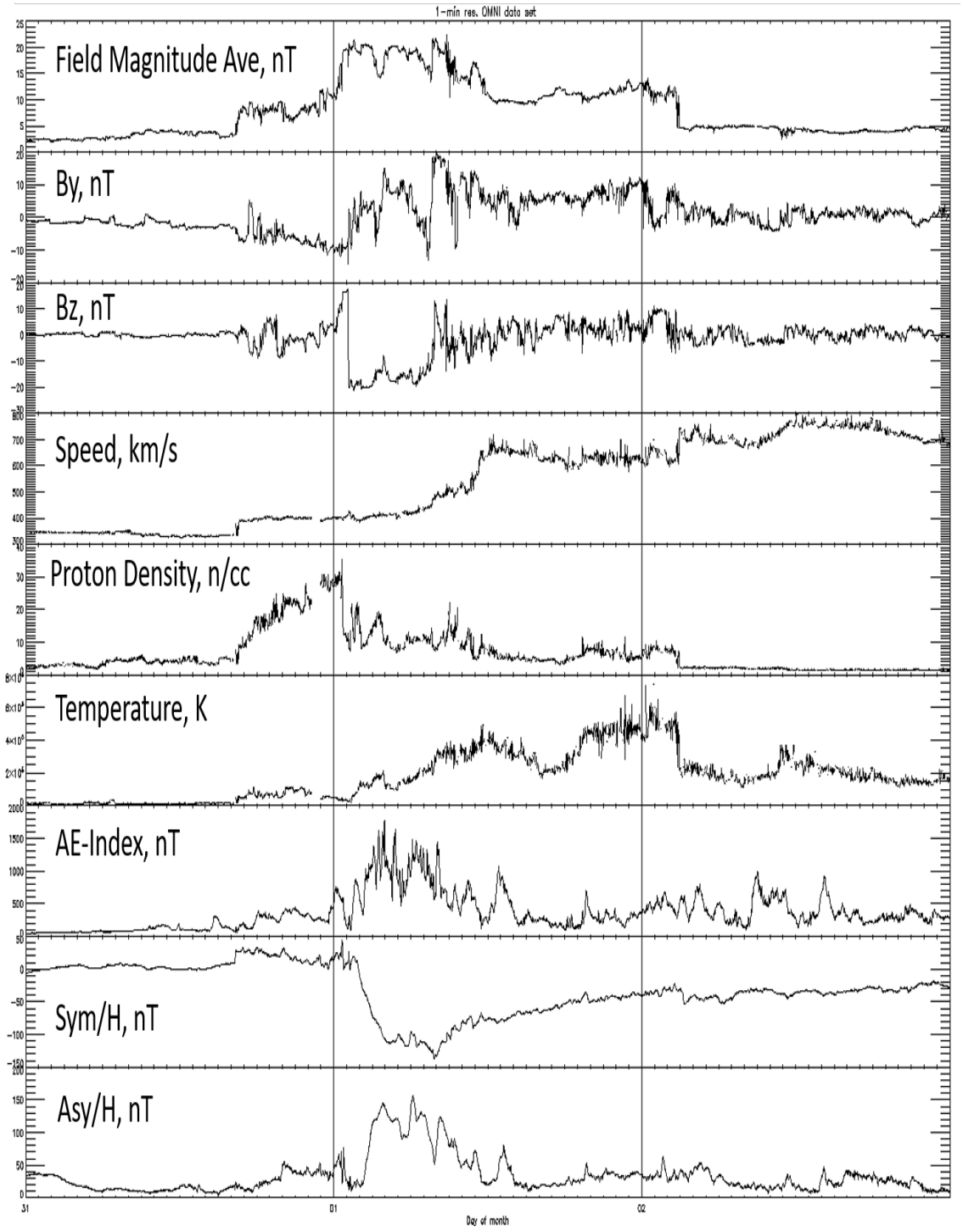

Figure 6.1: Figure obtained from https://omniweb.gsfc.nasa.gov/cgi/nx1.cgi

the positive x-axis pointing toward the Sun. The z-axis is the axis of the Earth's dipole field projected onto the plane perpendicular to the x-axis. The y-axis is defined such that $\hat{x} \times \hat{y} = \hat{z}$, with the positive y-axis pointing in approximately the opposite direction to the Earth's revolution about the Sun.

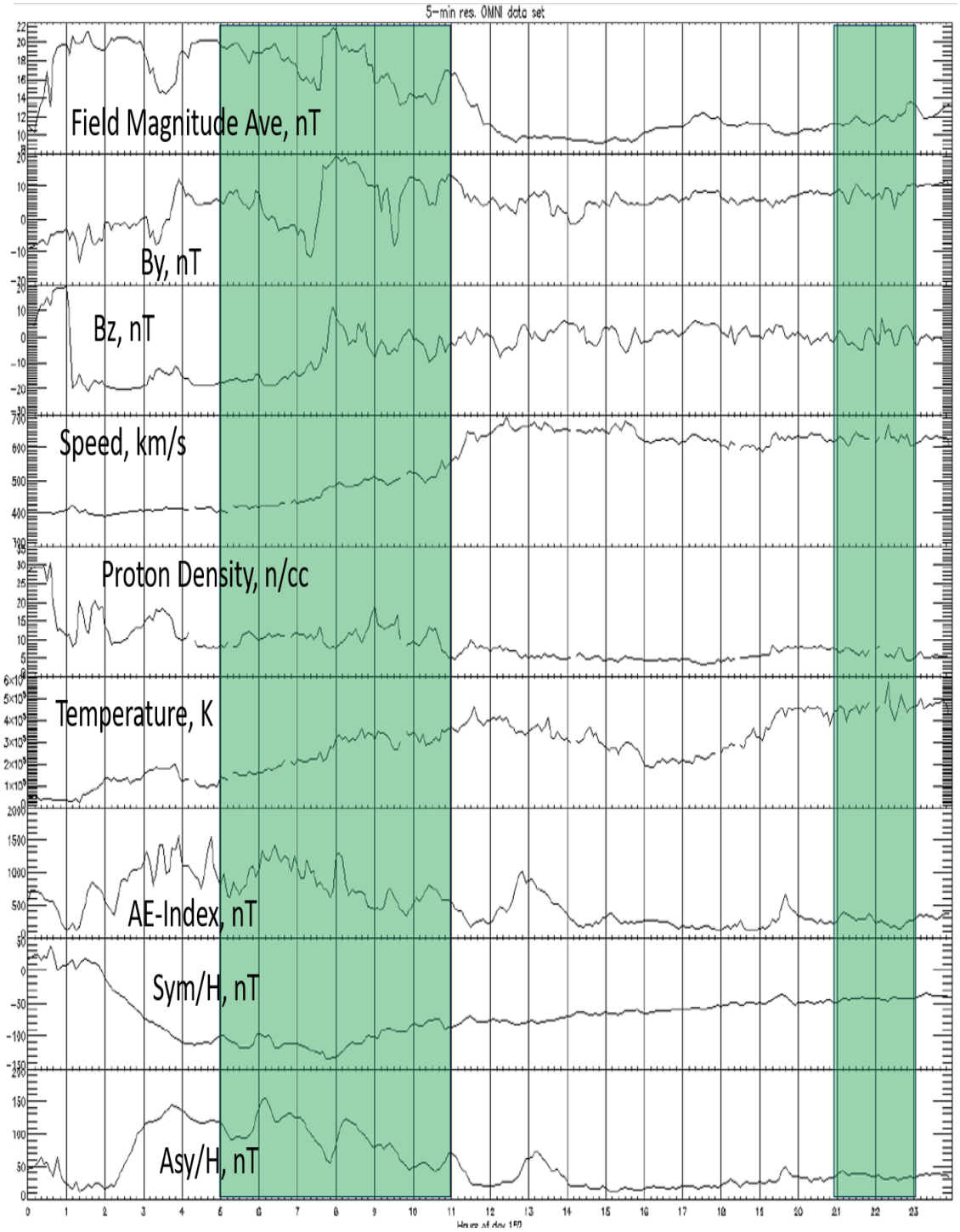

Figure 6.2: Figure obtained from https://omniweb.gsfc.nasa.gov/cgi/nx1.cgi

The second panel of each figure plots B_y, the y-component of the IMF. In these coordinates, the y-axis points in the direction opposite to the Earth's orbital direction. Under quiescent conditions, B_y is approximately zero. During this storm, B_y varies between -20 and 20 nT. While B_y remains generally positive by the second half of 01 June 2013, the oscillation

between positive and negative early in the storm is generally indicative of a CIR storm. The magnitude of B_y remains substantially elevated well into the recovery phase, returning to near zero in the first half of 02 June 2013.

The next panel is B_z, the component of the IMF perpendicular to the Earth's orbital plane. Before the onset of the storm, B_z was small. Early in the storm, B_z becomes positive, peaking at 20 nT, followed by a rapid drop to less than -20 nT, where it remains until approximately 08:30 UT. After this, B_z returns to oscillate about zero for the remainder of the storm.

Ion speed is plotted next. Prior to the onset of the geomagnetic storm the ion speed was relatively stable, at or slightly below 350 km/s. As the storm begins late on 31 May 2013, the ion speed increases. By the recovery phase, the ion speed has risen to 700-800 km/s. This elevated ion speed correlates with a high Mach number, which indicates a CIR storm.

The central row plots proton density, which is a good indication of ion density. Before the onset of the storm, the proton density remains essentially constant around four ions per cubic centimeter. As the storm begins late on 31 May 2013, it rises above 30 protons per cubic centimeter, followed by a sharp drop around 01:00 UT. The proton density varies between 10 and 20 protons per cubic centimeters after this, gradually dying down to below 10 protons per cubic centimeter by the recovery phase of the storm.

The next panel plots the temperature of the protons in the magnetosphere. Prior to the storm's onset, the temperature is low; below 20,000 K. The temperature increases gradually to approximately 600,000 K. It drops suddenly to below 200,000 K at about 03:00 UT on 02 June 2013, where it remains fairly stable through rest of the recovery. The high temperature throughout this storm indicates a CIR storm.

After the proton temperature comes the Auroral Electrojet (AE) Index. Unlike the previous quantities, the AE Index is not a simple measured quantity. Rather, it is a derived quantity that provides a quantitative measure of the magnetic activity induced by ionospheric currents within the auroral oval. While this value is not directly related to ionospheric FACs, greater AE Index values would be expected to generally correlate with higher FAC magnitudes. During this storm, the AE Index rises well above 1500 nT during the main phase of the storm, declining to less than 1000 nT during the recovery phase. Based on these values, one would expect to see

higher peak FAC magnitudes at 08:00 UT and before, with weakening FACs thereafter. Well into the recovery phase, in the second highlighted region, one would expect the FACs to be weaker still.

The second-to-last panel plots the Sym/H Index. The Sym/H Index gives the magnetic field attributable to the symmetric component of the ring current, which is a reliable means of determining the strength of a geomagnetic storm. The TWINS catalog documents all geomagnetic storms with minimum Sym/H Index values below -100 nT, beginning in 2008. This storm has a minimum Sym/H Index value of approximately -140 nT, making it a moderatley strong storm. There is no indication of a sudden storm commencement (SSC). Since SSCs are commonly associated with ICME storms, the absence of a SSC may indicate a CIR storm. Further, the Sym/H Index gradually returns to its pre-storm level over a period of more than 24 hours. This long recovery is also indicative of a CIR storm.

The final panel plots the Asym/H Index, which indicates the strength of the asymmetric ring current. Prior to the storm onset, Asym/H Index values were positive, but less than 50 nT. After storm commencement, Asym/H Index values greatly increase, peaking at over 150 nT, though these values change rapidly with time. As the main phase of the storm transitions to the recovery phase, Asym/H Index values decrease as well, returning to approximately their pre-storm levels throughout the recovery.

Several of the points discussed above indicate that this is a CIR storm. The large fluctuations in B_y, high ion speed and temperature, long recovery time, and lack of sudden storm commencement all help to distinguish this storm from an ICME storm. Further, CIR storms are tied to particular magnetic structures of the Sun. The Sun has a rotational period of approximately 27 days, and while the structures associated with CIR storms certainly change and dissipate over time, they often persist long enough to interact with the Earth on succeeding rotations. This appears to be the case here; while much weaker, there is a small storm approximately 27 days following this one. Thus, all indications point to this being a CIR storm.

This work focuses on the green highlighted regions of figure 6.2. Specifically, FACs have been determined for six times during the main phase - 05:00 UT, 07:00 UT, 08:00 UT, 09:00 UT, 10:00 UT, and 11:00 UT - and three times during the recovery phase - 21:00 UT, 22:00

UT, and 23:00 UT. These times were chosen because there are ion images extracted from ENA measurements available from at least one of the TWINS detectors. Further, this selection of times provides an overview of the time-evolution of the FACs over the entire storm, with sufficient separation that each time may be considered independently. During the main phase, one would expect the FACs produced by the storm to be of generally greater magnitude. Further, the magnetic field geometry deviates most strongly from a dipole during this time. Since the current calculations depend strongly on the magnetic field, the shape of the calculated ionospheric FACs will deviate most from the circular shape expected from a dipole field during this time period. During the recovery phase, the current magnitude would be expected to decrease, and the shape to become more circular as the conditions return to the quiescent baseline.

6.2 Field Aligned Currents at Northern Ionosphere

Figures 6.3, 6.4, and 6.5 display the Earth's northern ionosphere. Solar Magnetic (SM) coordinates are used, meaning the north pole is located at the geomagnetic north pole. Thus, the z-axis in SM coordinates coincides with the axis of the Earth's dipole field. The x-z plane contains both the dipole axis and the line connecting the Earth and Sun, with the x-axis pointing sunward (though generally not precisely at the Sun). The y-axis points in the direction opposite to the Earth's revolution about the Sun, such that $\hat{x} \times \hat{y} = \hat{z}$. In the images below, the Sun is to the left. Thus, the positive x-axis points to the left, the positive y-axis points to the bottom of the page, and the positive z-axis points out of the page.

The first column of images represents the field aligned currents at the Earth's northern ionosphere calculated assuming an isotropic ion pitch-angle distribution (PAD). The middle column plots the perpendicular component of the pressure, calculated using the TWINS ion PAD and mapped from the equatorial plane to the northern ionosphere. The third column represents the field aligned currents at the Earth's northern ionosphere calculated using the parallel and perpendicular pressure distributions determined from the TWINS ion PAD. All calculations are performed using the TS05 magnetic field model.

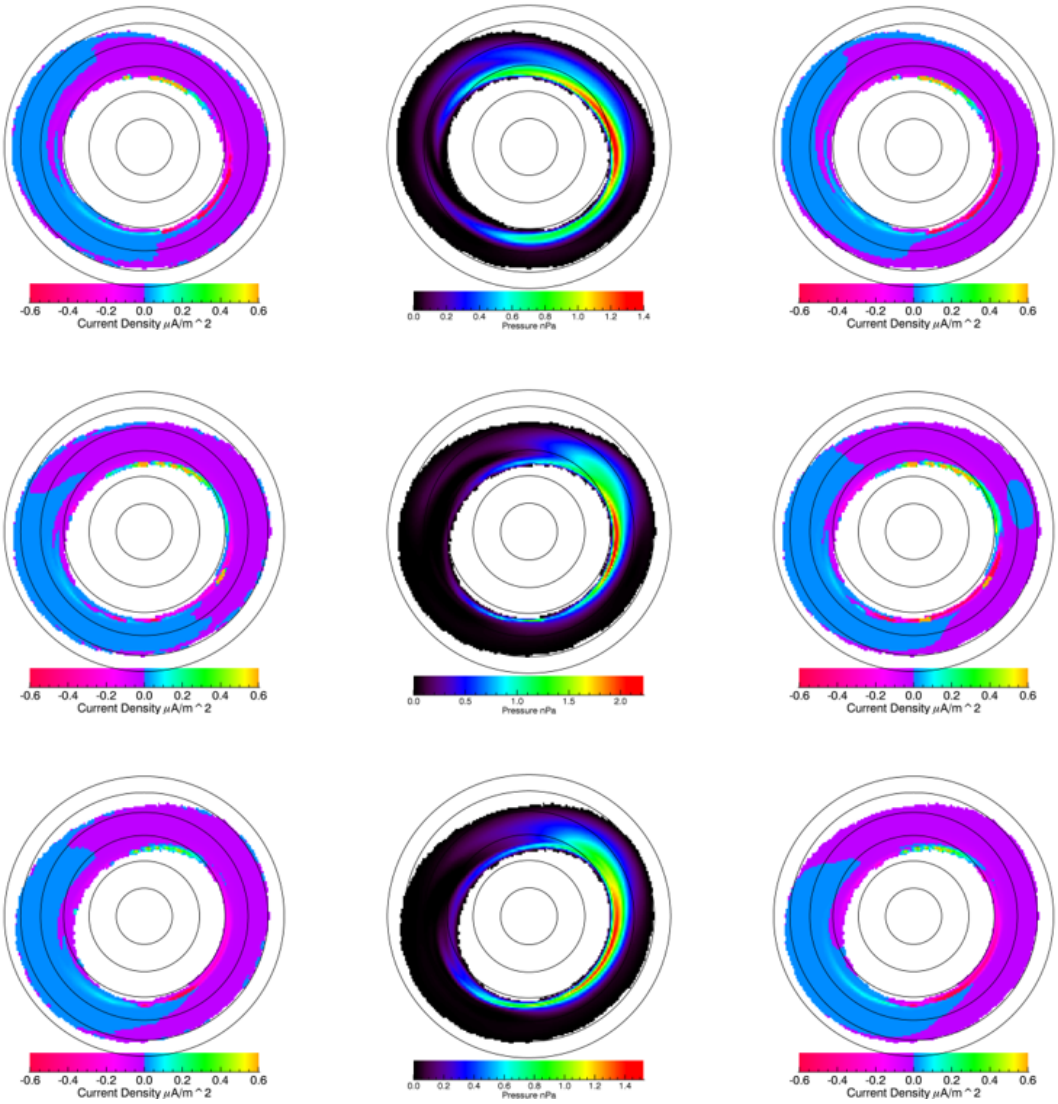

Figure 6.3: Left column: Field aligned current density at northern ionosphere calculated assuming isotropic PAD. Center column: Perpendicular pressure at northern ionosphere. Right column: Field aligned current density at northern ionosphere calculated using TWINS PAD. Top row: 0500UT. Middle row: 0700UT. Bottom row: 0800UT. The Sun is to the left in all images.

Despite the difference in assumptions, the two sets of current density images are similar. In both sets of FAC plots, positive currents - plotted in blue, green, and orange - are inward, while negative currents - plotted in red and purple - are outward. In the classic picture of FACs, Region I Birkeland currents will flow inward along geomagnetic field lines on the dawn side (top of image) and outward on the dusk side (bottom of image), while Region II Birkeland

currents will do the opposite. As the plots indicate, this is not clearly reflected in these calculations. While there is a clear demarcation between regions with inward and outward FACs, these regions are not widely separated, and do not lie strictly in the dawn and dusk regions of the ionosphere. Instead, these currents are spread over all longitudes, though the strongest currents generally lie near the dusk and dawn regions. The inward FACs appear to be generally centered about a line in the noon-to-dusk quadrant, while the outwards FACs are centered about a line near midnight or in the midnight-dawn quadrant. During the early part of the storm, the current regions are not equal in size; the outward currents cover a substantially larger portion of the northern ionosphere. By 11:00 UT, however, the currents cover approximately the same area of the ionosphere, and do so throughout the recovery.

Because TWINS ENA measurements correspond to trapped ions on magnetic field lines $L \leq 8$, it is expected that these images will comprise Region II currents. Under quiescent conditions, the near-Earth magnetic field more closely resembles a dipole field. During such times, the $L = 8$ shell intersects the ionosphere at approximately 70 degrees latitude. However, during geomagnetic storms the magnetic field lines become further distorted away from a dipole configuration. This distortion means the $L = 8$ shell intersects the ionosphere at lower latitudes. Further, because the distortion of the magnetic field lines is not uniform, the maximum observable latitude becomes more heavily magnetic local time (MLT) dependent. Latitudes corresponding to $L > 8$ are not observable by TWINS during this storm.

While the bulk of the FACs displayed in these plots are Region II-like currents, it is possible that Region I-like currents may also appear at the highest latitudes. In each of these FAC plots, both those assuming PAD isotropy and those that do not, there is a section of inward current near dawn at the highest latitude observable. There is also a corresponding outward current near dusk, extending toward midnight. These bands of current are of greater intensity than those measured elsewhere and are near the expected place for the outer edge of Region I currents. These currents become more uniform as the storm progresses. By 23:00 UT (see figure 6.5), well into the recovery phase, these currents are weaker and occupy a larger region of the ionosphere. They are also approximately symmetric about the dawn/dusk line, as would be expected in the standard picture of Birkeland currents. Region 1 currents, however, do not

follow inner magnetospheric field lines in the standard picture. Thus, the observed currents in these regions indicate that magnetospheric currents are more complicated than the traditional picture.

The plots begin at 05:00 UT (see figure 6.3), during the main phase of the geomagnetic storm. The $L = 8$ magnetic field lines intersect the ionosphere in an oval shape, with the long axis running from roughly MLT=11h to MLT=22h. $L = 8$ are as far north as 65° latitude near dawn, and south of 60° in the dusk-midnight quadrant. In both the isotropic and anisotropic PAD cases, the strongest inward FACs are found in a small band from approximately MLT=3h to dawn, while the strongest outward currents stretch from near dusk to past midnight. Both of these bands are very narrow, and are found at the northernmost edge of the region of observable currents. Another strong band of inward currents is set back a few degrees from the northern edge, covers an approximately 3h band from dusk stretching toward noon, and is substantially weaker than the first band of inward current discussed. Weak currents fill the rest of the space, with negative currents filling nearly all the night side, extending well into the day side past dawn, and inward currents covering the day side from roughly MLT=15h to dusk. The differences between the FACs calculated using isotropic and anisotropic PADs are minimal.

Because these are pressure driven currents, one would expect the FAC distribution to be associated with pressure gradients. This association is more complicated than it would appear at first glance, however. As one can see in the derivation performed in the previous chapter, even in the relatively simple isotropic case, the pressure gradient must be crossed with the gradient of the magnetic field (see equation 5.13). Further, it is only the component of the resultant vector parallel to the magnetic field that contributes, and this must be integrated along the field line from the point of minimum magnetic field to the ionosphere. In the anisotropic PAD case, it is even more complicated, as two more integrals are involved: one involving $\boldsymbol{\nabla}\chi \times \boldsymbol{\nabla}P_\perp$ and the other $\boldsymbol{\nabla}\chi \times \boldsymbol{\nabla}B$ (see equation 5.12). Despite this, one can see some correlation simply by looking at the pressure plots at the ionosphere (see central column of figures 6.3, 6.4, and 6.5).

In the 05:00 UT plot (see top row of figure 6.3), the perpendicular pressure is highest on the nightside from just before midnight to dawn, in a latitudinal band roughly three degrees wide near the northern edge of detectability. The regions of greatest pressure gradient are found

largely near this peak zone, where the pressure drops most quickly. The region of high inward FACs near dawn is associated with a strong pressure gradient, largely in the negative azimuthal direction. The strong outward currents stretching from dusk to past midnight are associated with pressure gradients in the negative latitudinal direction. The weaker positive currents in the noon-dusk quadrant are associate with a pressure gradient in the positive azimuthal direction. Further, these currents are farther south than the other peak current zones. The band of high pressure also extends further south in that region. While one cannot simply look at the pressure plots to determine what the currents will be like, there are certainly correlations.

The next set of plots is for 07:00 UT (see middle row of figure 6.3). At this time there are more pronounced differences between the isotropic and anisotropic PAD cases than there were at 05:00 UT. In the isotropic PAD case, the outward current region has extended further toward noon in the noon-dusk quadrant, while the inward current region has extended past dusk into the dusk-midnight quadrant. In the anisotropic PAD case, these changes are much less pronounced. In both cases, the peak inward current in the midnight-dawn quadrant covers a substantially larger azimuthal region, and in the anisotropic PAD case, the region of latitude covered is wider as well. The region of peak outward current has rotated toward dawn and is longer in the azimuthal direction, though in the isotropic PAD case it is narrower in the latitudinal direction and weaker than at 05:00 UT. The region of weaker inward current in the noon-midnight quadrant is smaller in both cases, and has moved somewhat towards noon. Perhaps the biggest difference between the two cases is the presence of an oval-shaped region of inward current near midnight in the large region of outward current on the nightside. This current is completely absent in the isotropic PAD case.

The oval defining the northernmost line observable by TWINS has rotated substantially over the course of two hours. The long axis now runs from approximately MLT=3h to MLT=15h. The $L = 8$ line extends as far north as 67° near MLT=8h and as far south as 58° near MLT=16h. The region of highest pressure, shown in red, is considerably smaller, and is now more or less symmetric about midnight. The region of moderate pressure, shown in green, now covers a smaller azimuthal region than it did at 05:00 UT. This region of pressure has broadened in the midnight-dawn quadrant, though, covering more than ten degrees of latitude now.

By 08:00 UT (see bottom row of figure 6.3), the two FAC plots look quite similar again. The oval region of inward current near midnight in the 07:00 UT FAC plot using the anisotropic PAD is no longer present. Further, the regions of weaker currents are in broad agreement, with only minor difference in the boundaries between inward and outward current. The region of peak inward current near dawn is much smaller and weaker in both FAC plots, and occupies essentially the same position. The region of peak outward current now occupies primarily the dusk-midnight quadrant in both FAC plots, though it is somewhat weaker in the isotropic PAD plot. The second peak inward current is somewhat stronger and larger than at 07:00 UT, and is perhaps the greatest difference between the two FAC plots. In the isotropic PAD case, this current region stretches from MLT=15h to dusk, while in the anisotropic PAD case, it occupies a two degree band in latitude through the entire noon-dusk quadrant, and is substantially greater in magnitude than in the isotropic PAD case.

The oval corresponding to $L = 8$ at the ionosphere has become more elliptical in the 08:00 UT plots, and has rotated counterclockwise a few degrees from 07:00 UT. The oval goes as far north as 69° latitude near MLT=7h and as far south as 59° latitude near dusk. The region of greatest pressure now occupies a 2°-latitude wide strip across the nightside, from approximately MLT=20h to 2h, with the region of moderate pressure extending past this nearly to dawn, covering approximately 10° in latitude. The magnitude of the pressure is, however, substantially lower, falling by approximately 25% from 07:00 UT. This contributes to the generally weaker currents seen in the FAC plots for this time.

09:00 UT (see top row of figure 6.4) once again brings some interesting differences between the FAC plots. In the isotropic PAD case, the outward currents have extended past dawn at low latitudes. This change at low latitudes is not seen in the anisotropic PAD case; instead, the inward currents extend through the region of outward current, connecting with the region of peak inward current, and isolating a region of outward current from the main body of current. Additionally, a region of inward current has appeared again near midnight at low latitude in the anisotropic PAD case. This is not seen in the isotropic PAD case. The peak currents continue to weaken at this time, particularly the secondary inward current peak in the noon-dusk quadrant, which has also moved toward dusk, particularly in the isotropic PAD case.

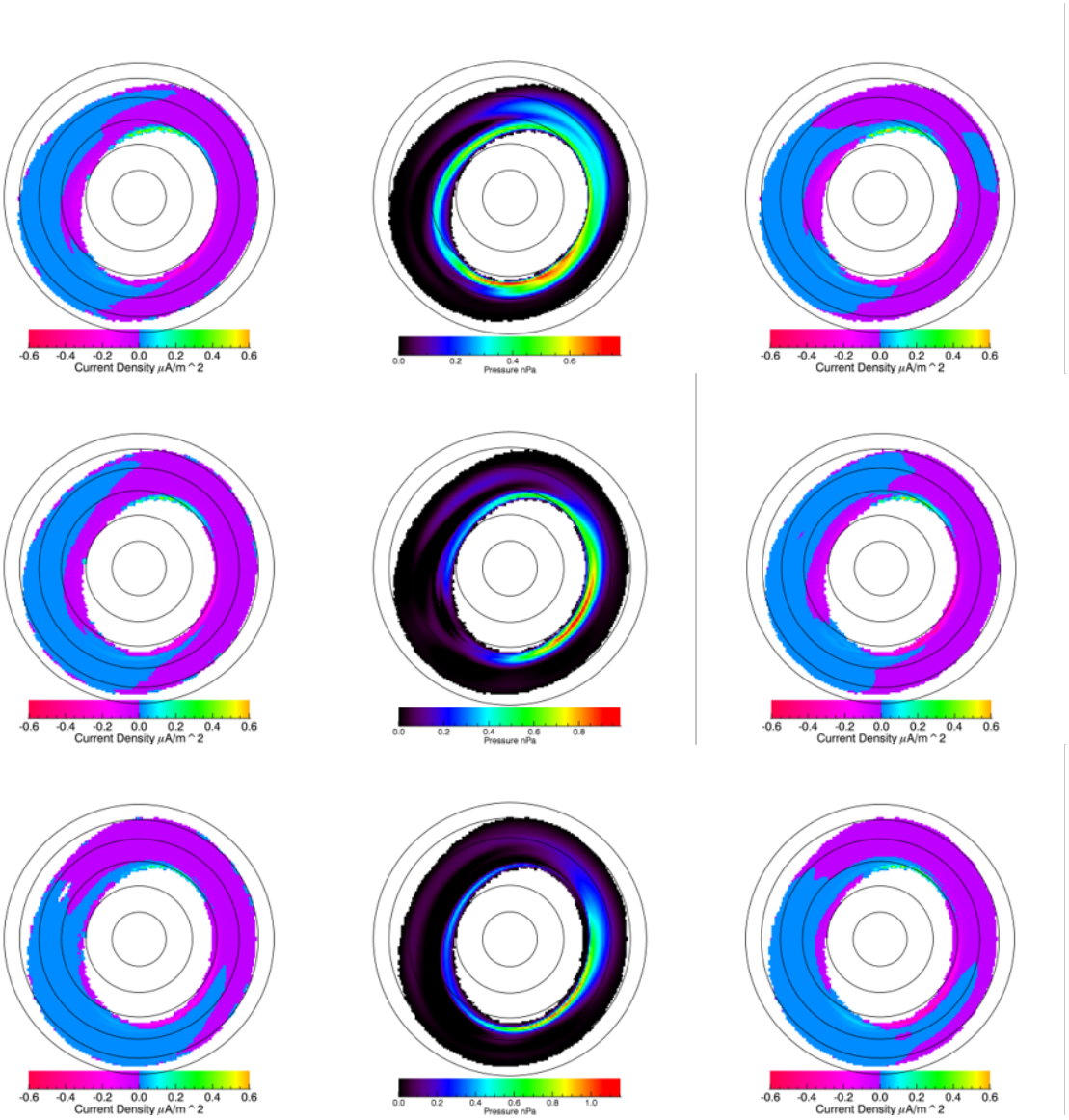

Figure 6.4: Left column: Field aligned current density at northern ionosphere calculated assuming isotropic PAD. Center column: Perpendicular pressure at northern ionosphere. Right column: Field aligned current density at northern ionosphere calculated using TWINS PAD. Top row: 0900UT. Middle row: 1000UT. Bottom row: 1100UT. The Sun is to the left in all images.

The oval corresponding to $L = 8$ at the ionosphere appears slightly more elliptical than it did at 08:00 UT, has rotated slightly counterclockwise, and is more off-center than at previous times, with the center of the oval ten degrees or more from the pole. The peak in pressure has moved toward dusk, stretching from approximately MLT=16h to 21h at high latitude. The region of moderate pressure is far more widespread, essentially encircling the ionosphere at high latitudes. The magnitude of the pressure has again decreased substantially, however. It is

almost 40% lower than at 08:00 UT, and less than half the value at 07:00 UT. This contributes to the continued weakening of the FACs.

The FACs for isotropic and anisotropic PAD at 10:00 UT are more similar to each other than those at 09:00 UT (see middle row of figure 6.4), but still show some important differences. The isotropic PAD case is largely unchanged from 09:00 UT, but the anisotropic PAD case has changed to become closer to the isotropic PAD case. The inward current on the dayside has extended to about dawn, and the region of inward current near midnight in the 09:00 UT plot is now gone. The inward current still connects to the peak near dawn at high latitude, but the connecting region is now much thinner. There is now a very small region of outward current surrounded by inward current in the dawn-noon quadrant which does not appear in the isotropic PAD case.

The oval corresponding to $L = 8$ at the ionosphere has rotated counterclockwise slightly compared to 09:00 UT, and remains off-center. The oval lies north of 70° latitude in the dawn-noon quadrant. The region of greatest pressure has returned to the dusk-midnight quadrant, and the region of moderate pressure no longer extends completely around the ionosphere, interrupted by a region of very low pressure near MLT=15h. The pressure has increased somewhat since 09:00 UT, but not sufficiently to make a noticeable difference in the magnitudes of the peak FACs.

The final set of FACs calculated during the main phase of the storm is for 11:00 UT. In both isotropic and anisotropic PAD cases, the region of outward current has extended counterclockwise well into the dawn-noon quadrant, particularly at lower latitudes. The region of inward current has also extended counterclockwise, occupying most of the dusk-midnight quadrant at mid-latitudes, centered around 50° latitude. The anisotropic PAD case continues to exhibit a band connecting the inward current region to the peak inward current near dawn. For the first time, the isotropic PAD case shows the same feature. The isotropic PAD case has a peculiar region of near-zero current in the dawn-noon quadrant at approximately 55° latitude. The anisotropic PAD case shows a small region of outward current within the large region of inward current, similar to that at 10:00 UT, but somewhat larger and located near dusk. The

secondary inward current peak is substantially stronger in the anisotropic case, but this is not reflected in the isotropic PAD case.

The oval corresponding to $L = 8$ has continued to rotate counterclockwise and remains off-center. The peak pressure has again increased, but this increase is largely confined to a small region about 1° in latitude in the dusk-midnight quadrant. Aside from this region, the pressure remains largely unchanged from 10:00 UT, except for near MLT=15h, which is no longer near zero, and at high latitudes in the midnight-dawn quadrant, where the pressure has decreased substantially from 10:00 UT.

Moving into the recovery phase of the storm, the next set of calculations is for 21:00 UT. Once again, the FACs for both the isotropic and anisotropic PADs are very similar. The region of inward current extends from approximately 60° latitude near midnight, clockwise around to dawn at low latitudes, with a separate region of stronger inward current at high latitude from just past midnight to a few hours after dawn. There is a second, weaker peak of inward current around dusk at approximately 60° latitude. The region of outward current occupies most of the nightside, and encircles the ionosphere at high latitudes, with a region of peak current in the dusk-midnight quadrant near 55° latitude.

The oval corresponding to $L = 8$ is less elliptical than during the main phase, and more consistently at higher latitudes. This indicates the geomagnetic field is becoming less distorted as the storm moves into the recovery phase. There is a region of high pressure centered approximately around midnight, ranging in latitude from approximately 65° latitude near dusk, to 56° latitude approaching dawn. The pressure is greater than it was twelve hours previously, but this does not seem to translate to greater FAC magnitudes in this case, probably because the magnetic field gradients are smaller.

The plots at 22:00 UT show more substantial differences in FACs between the isotropic and anisotropic PAD cases. The isotropic PAD case is similar to 21:00 UT, with the primary differences being a weakening of the secondary peak of inward current near dusk and the region of inward current extending further counterclockwise at high latitudes in the dusk-midnight region, almost connecting with the region of peak inward current. The anisotropic PAD case, however, has changed more substantially from 21:00 UT. In this case, there is a narrow band of

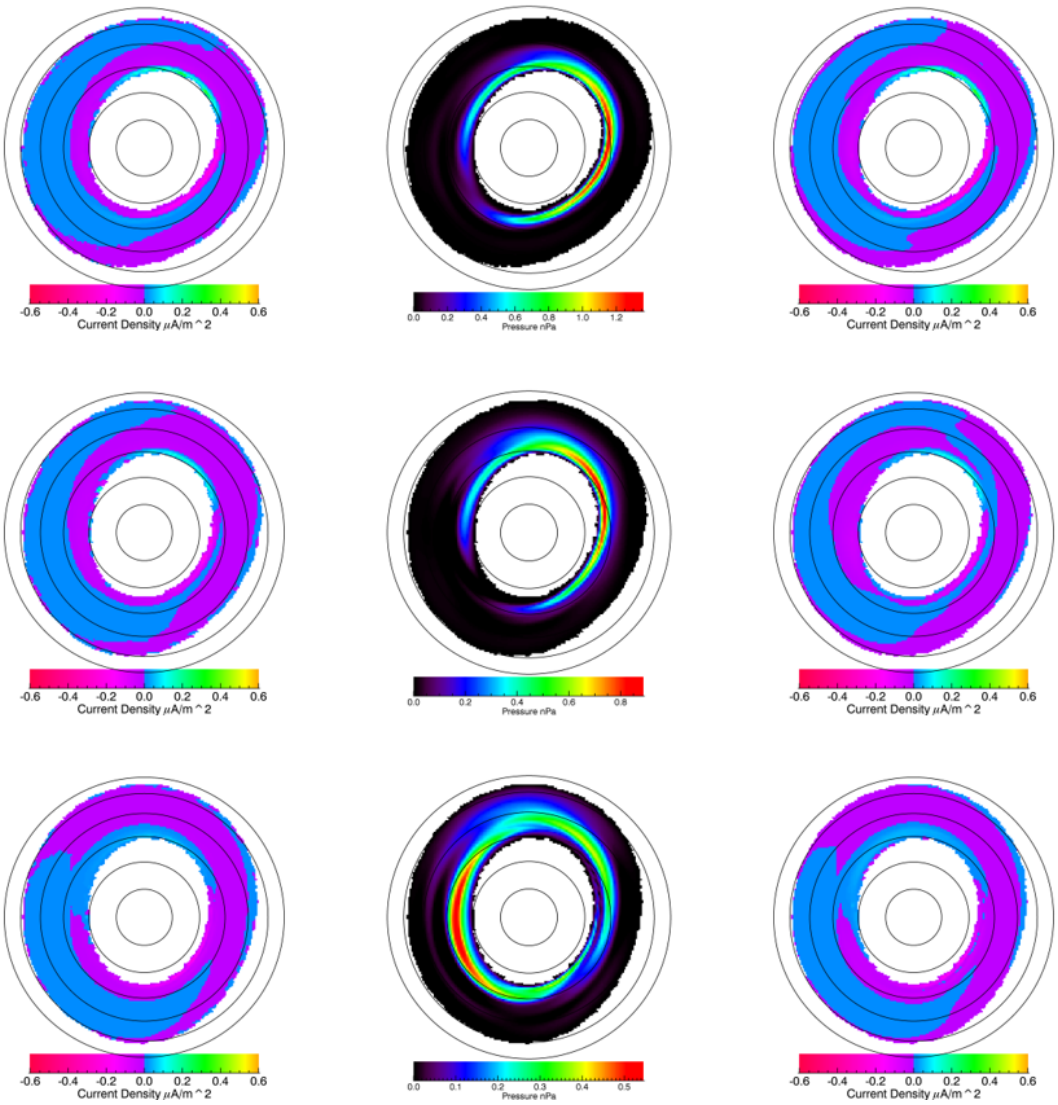

Figure 6.5: Left column: Field aligned current density at northern ionosphere calculated assuming isotropic PAD. Center column: Perpendicular pressure at northern ionosphere. Right column: Field aligned current density at northern ionosphere calculated using TWINS PAD. Top row: 2100UT. Middle row: 2200UT. Bottom row: 2300UT. The Sun is to the left in all images.

inward current stretching across the entire nightside of the ionosphere and connecting with the region of peak inward current. Further, the secondary peak near dusk has weakened substantially, nearly disappearing from the plot.

The oval corresponding to $L = 8$ has rotated counterclockwise compared to 21:00 UT. The region of peak pressure has also moved in this direction, now primarily occupying a band

at high latitude in the midnight-dawn quadrant. The pressure has lessened considerably from 21:00 UT, and as would be expected, the FACs are of lower magnitude as well.

The final time examined during this storm is 23:00 UT. While the FACs have changed considerably from 22:00 UT for both isotropic and anisotropic PAD cases, they once again look quite similar to one another. In both isotropic and anisotropic PAD cases, the region of inward current at mid and low latitudes stretches from just before noon to a few hours after dusk. The outward current region stretches from near dusk at low latitudes to the half way point of the dawn-noon quadrant at mid and low latitudes. There is a small strip of inward current at the lowest latitudes on the nightside. At high latitudes, a relatively large region of inward current occupies the dawn-side half of the ionosphere, connecting with the low latitude inward current region near noon, while the dusk-side half of the ionosphere is occupied by a relatively large region of outward current, which connects with the low latitude outward current in the dusk-midnight quadrant. This time is perhaps the closest to the classic picture of Birkeland currents, with the high latitude currents representing Region I-like currents, and the low latitude currents Region II-like. This is perhaps to be expected, as the magnetosphere slowly returns to quiescent conditions as the recovery phase progresses.

The oval corresponding to $L = 8$ has continued to rotate further counterclockwise. The region of greatest pressure has moved to the dayside, which is quite unusual, and a second, smaller peak occupies the midnight-dawn quadrant. The pressure has dropped even lower at 23:00 UT, and correspondingly the FACs for both the isotropic and anisotropic PAD cases are quite weak.

6.3 FAC Fine Details

Because some of the most interesting differences between the FAC plots using isotropic and anisotropic PADs occur in regions where the magnitude of the current density is small, it is useful to place a limit on the maximum magnitude and examine the regions of small current more closely. To do this, the maximum magnitude of current density in the FAC plots has been set to $0.005 \mu A/m^2$. Thus, any region with magnitude larger than this will appear on the plots

as $\pm 0.005 \mu A/m^2$. This allows the full colorbar to be applied to the range of current densities between $-0.005 \mu A/m^2$ and $0.005 \mu A/m^2$, making more of the fine details visible.

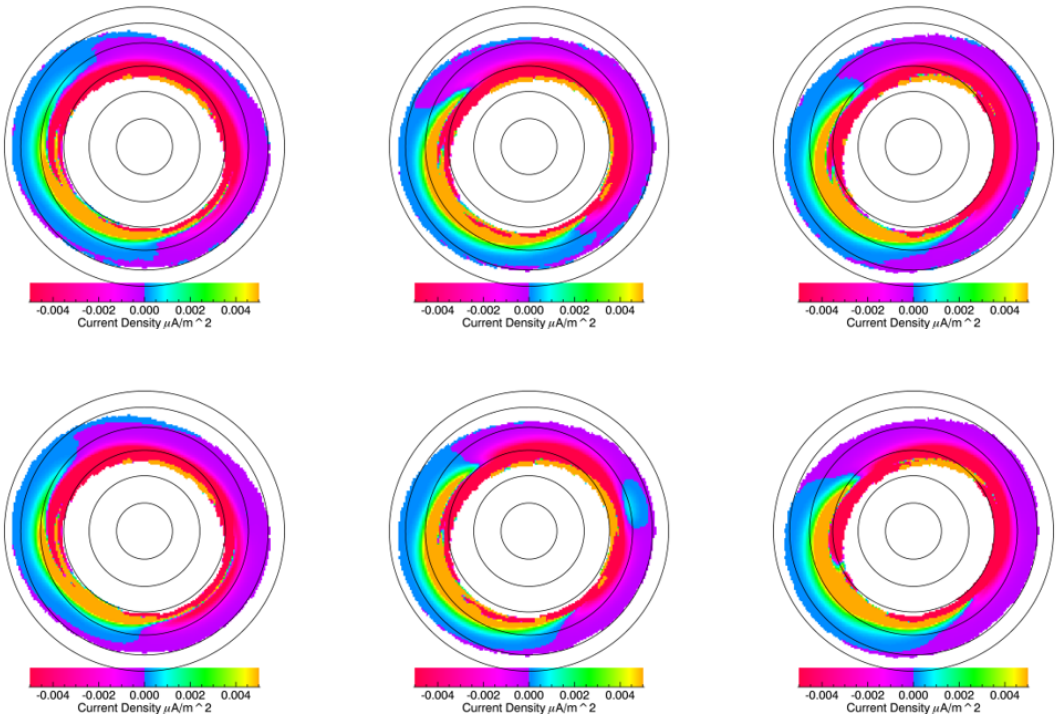

Figure 6.6: FACs at northern ionosphere limited to ± 0.005 μA/m^2 to see detail in small currents. Top Row: FACs from isotropic PAD. Bottom Row: FACs from anisotropic PAD. Left Column: 05:00 UT. Middle Column: 07:00 UT. Right Column: 08:00 UT.

The plots for 05:00 UT (left column of figure 6.6) show few details not apparent in the original FAC plots. For both isotropic and anisotropic PAD cases, the FACs increase in magnitude with latitude, as would normally be expected. The plots show minimal differences between the isotropic and anisotropic PAD cases. The 07:00 UT plots (middle column of figure 6.6), however, shows an important difference between the isotropic and anisotropic PAD cases. As pointed out previously, the region of inward current surrounded by outward current near midnight only appears in the anisotropic PAD plot. In this representation, one can see that the region is not uniform; rather it has a greater magnitude at higher latitude. Further, the high latitude border of this region is very close to reasonably strong outward currents. This region appears to impinge upon the region of high latitude outward current, leaving a narrower band of current in that region than is seen in the isotropic PAD case. This region will be discussed further in the next chapter.

At 08:00 UT (right column of figure 6.6), there are few substantive differences between the FACs for the two cases. In both, stronger current densities are found generally at higher latitude, as expected. At 09:00 UT (left column of figure 6.7), however, there are several important differences between the FACs for the isotropic and anisotropic PAD cases. The most obvious is the region of low latitude inward current near midnight, in the midst of a region of outward current. This region appears only in the anisotropic PAD plot, but unlike the similar region at 07:00 UT, this region remains undifferentiated; that is, the region contains nearly uniformly small magnitude currents throughout. This is likely due to the low latitude, which would be expected to have very small FACs due to the short length of the magnetic field line connecting the ionosphere to the surface of minimum magnetic field (see equation 5.12). As seen in the previous set of plots, in the anisotropic PAD case, the high latitude region of strong inward current near dawn joins with the mid-latitude of moderate inward current, separating the outward current into two regions. The outward currents at high latitude near dawn are of much greater magnitude in the isotropic PAD case, but the weaker outward currents in the anisotropic PAD case occupy a larger area of the ionosphere. One can also see that the secondary inward current peak in the noon-dusk quadrant, while greater in magnitude than the surrounding currents, is smoothly continuous with the surrounding currents in the isotropic PAD case. In the anisotropic PAD case, this current region changes more abruptly, and decreases more rapidly with descending latitude.

The FACs calculated using the anisotropic PAD at 10:00 UT (middle column of figure 6.7) is also substantially less uniform on the dayside than its counterpart using the isotropic PAD. The region of relatively high inward current varies much more substantially with latitude than in the isotropic PAD case. Further, as previously noted, the region of mid-latitude inward current connects to the high latitude region near dawn in the anisotropic PAD case, but not in the isotropic PAD case. While the connecting region is substantially weaker than either of the peak currents it is connecting, it remains moderately strong until low latitudes.

By 11:00 UT (right column of figure 6.7), both the isotropic and anistropic PAD cases have the two regions of inward current connected. At this time, both sets of FACs show unusually rough edges to the regions of strong inward current on the dayside, though the anisotropic PAD

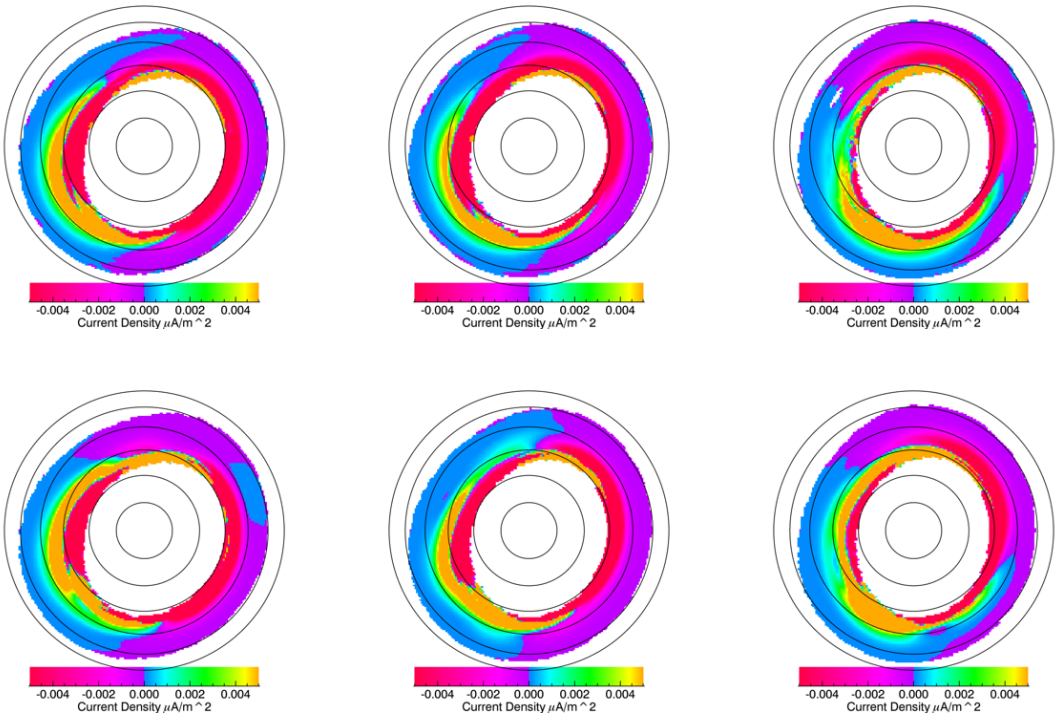

Figure 6.7: FACs at northern ionosphere limited to ± 0.005 $\mu A/m^2$ to see detail in small currents. Top Row: FACs from isotropic PAD. Bottom Row: FACs from anisotropic PAD. Left Column: 09:00 UT. Middle Column: 10:00 UT. Right Column: 11:00 UT.

case shows more variation. For example, the FAC plot using the anisotropic PAD shows a low current region between $55°$ and $60°$ latitude, just past noon, as well as a region of small outward current at approximately $50°$ latitude, just after dusk.

By 21:00 UT (leftt column of figure 6.8), the storm has begun the recovery phase, and the FACs vary more uniformly with latitude. In all three times plotted during the recovery, the current regions appear to be in the process of separating into Region I and II currents. The inward currents at high latitude on the dawn side and the outward currents at high latitude on the dusk side appear to be Region I-like Birkeland currents, while the outward currents at mid-latitude on the dawn side and the inward currents at mid-latitude on the dusk side appear very close to where Region II Birkeland currents should be.

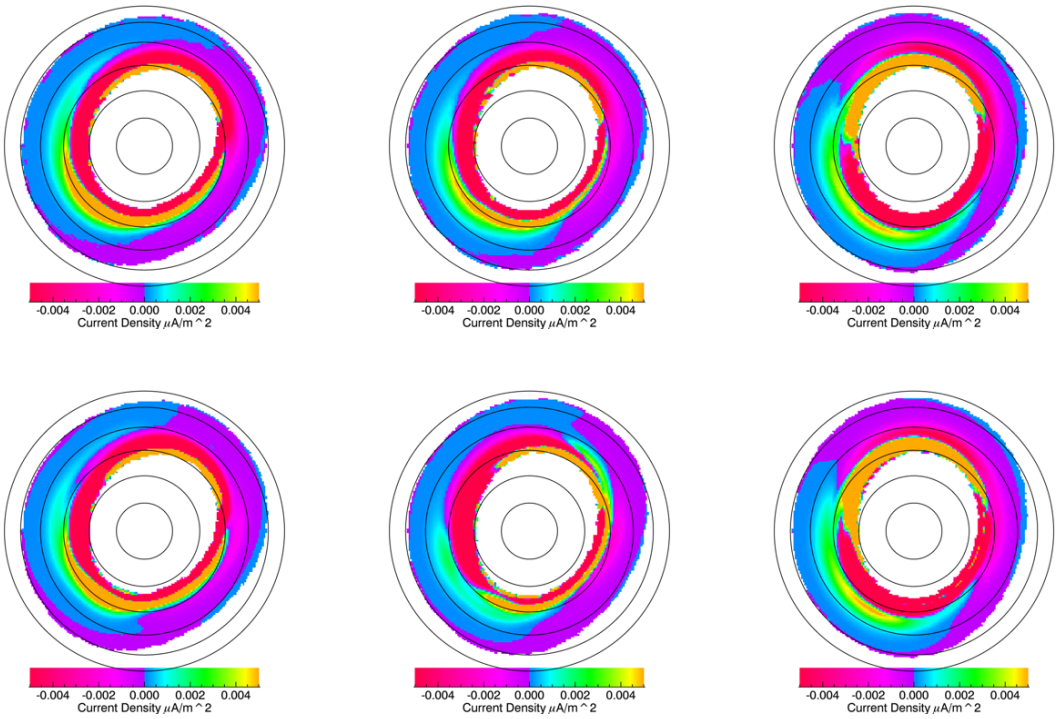

Figure 6.8: FACs at northern ionosphere limited to ± 0.005 $\mu A/m^2$ to see detail in small currents. Top Row: FACs from isotropic PAD. Bottom Row: FACs from anisotropic PAD. Left Column: 21:00 UT. Middle Column: 22:00 UT. Right Column: 23:00 UT.

6.4 Pressure Plots

The following plots show the pressure components of pressure plotted at the ionosphere. While the behavior of pressure has already been discussed, that was based solely on the behavior of the perpendicular pressure. The following plots compare perpendicular pressure, parallel pressure, and the scalar pressure, which is simply the sum of these two components.

It is immediately apparent that there is very little difference between the parallel and perpendicular ionospheric pressure plots, regardless of the time. Not only are the two pressures essentially equal in magnitude, the location of the peak pressure and the structure of the pressure distribution are very nearly identical. The scalar pressure is simply the sum of the parallel and perpendicular pressures, as noted in the derivation in chapter 5. The only substantive difference between this plot and the other two is the scale; the magnitude of the scalar pressure

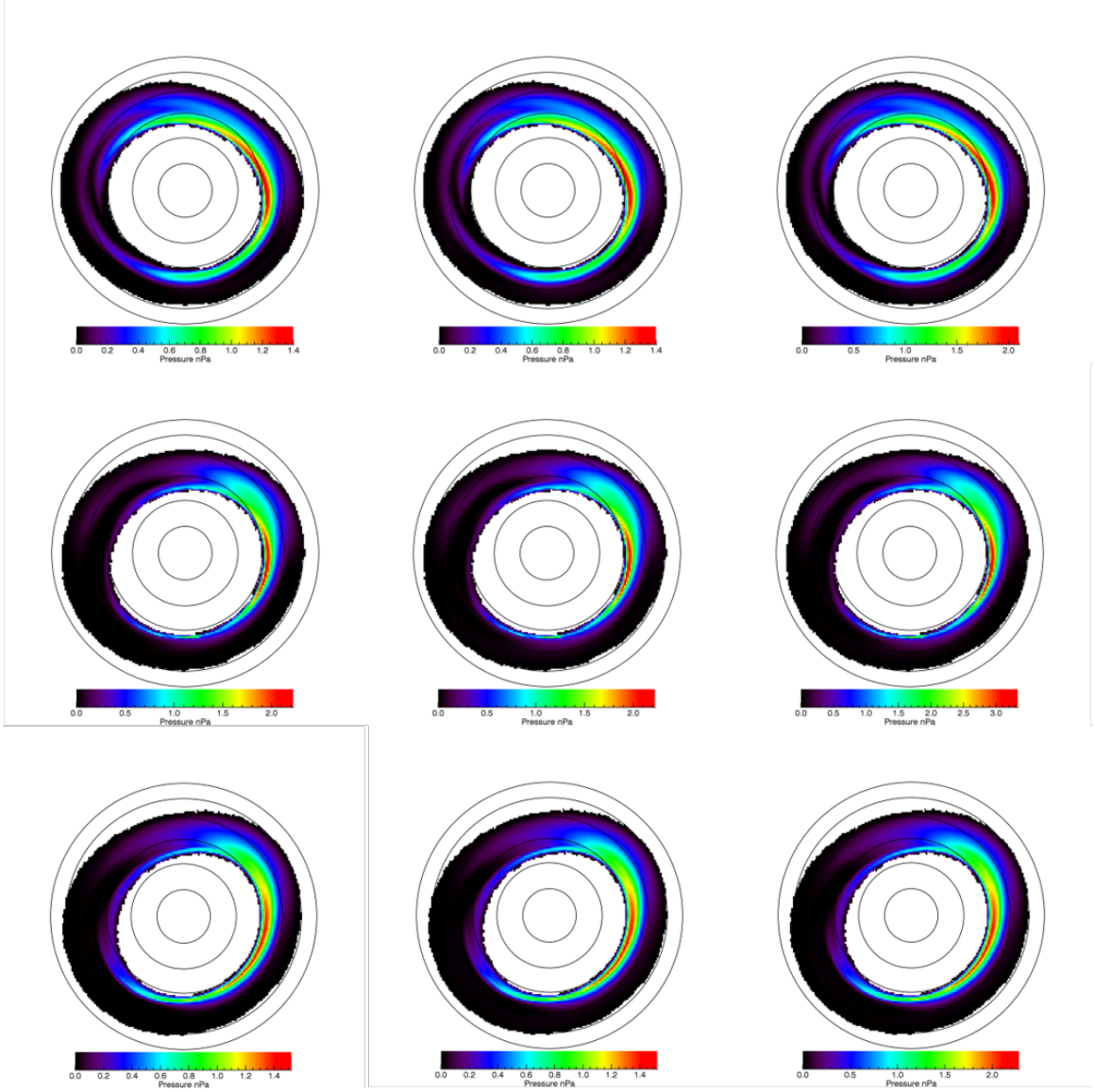

Figure 6.9: Pressure plots at northern ionosphere. Top Row: 05:00 UT. Middle Row: 07:00 UT. Bottom Row: 08:00 UT. Left Column: Parallel Component of Pressure. Middle Column: Perpendicular Component of Pressure. Right Column: Scalar Pressure.

is simply the sum of the parallel and perpendicular pressures. Since the parallel and perpendicular pressure distributions are so nearly identical, the structure of the scalar pressure is not noticeably different from either.

While the $L = 8$ oval rotates counterclockwise throughout the main phase of the storm, the region of maximum moves in the opposite direction through much of this time. At 05:00 UT (left column of figure 6.9), the region of maximum pressure occupies a band from just before midnight through the midnight-dawn quadrant. Over the next several hours, this region moves clockwise, until by 09:00 UT (left column of figure 6.10) it occupies a region centered

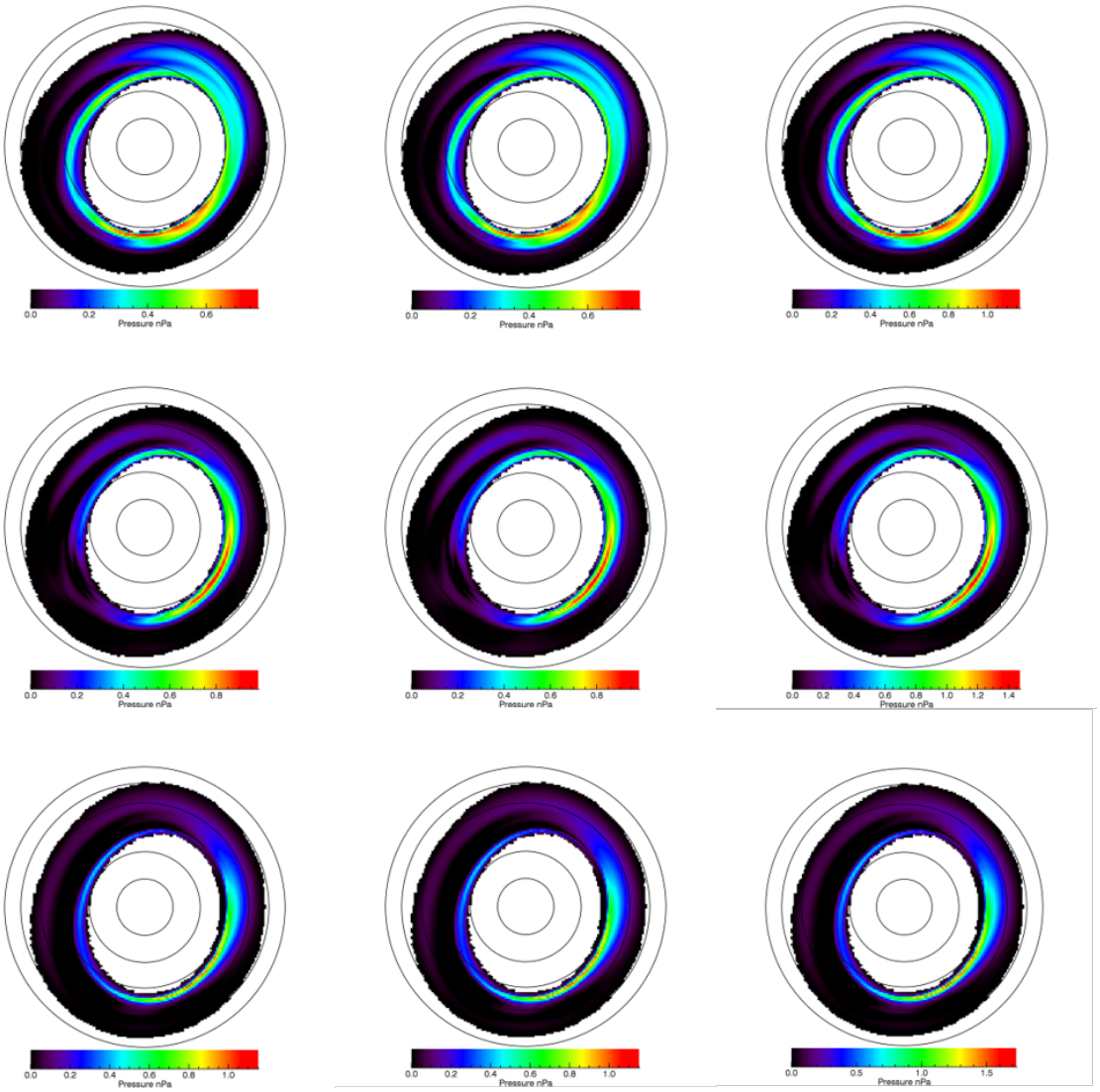

Figure 6.10: Pressure plots at northern ionosphere. Top Row: 09:00 UT. Middle Row: 10:00 UT. Bottom Row: 11:00 UT. Left Column: Parallel Component of Pressure. Middle Column: Perpendicular Component of Pressure. Right Column: Scalar Pressure.

on a point just after dusk. At this time, it has also shows signs of a double peak in the pressure; that is, there is a separate high pressure region, in this case located in the dawn-noon quadrant. After 09:00 UT, the secondary diminishes, and the primary peak settles into the dusk-midnight quadrant.

Figure 6.11 shows the ionospheric ion pressure during the recovery phase of the storm. At 21:00 UT (left column of figure 6.11), the region of peak pressure occupies a wide band centered approximately on midnight. It then moves into the midnight-dusk quadrant for the

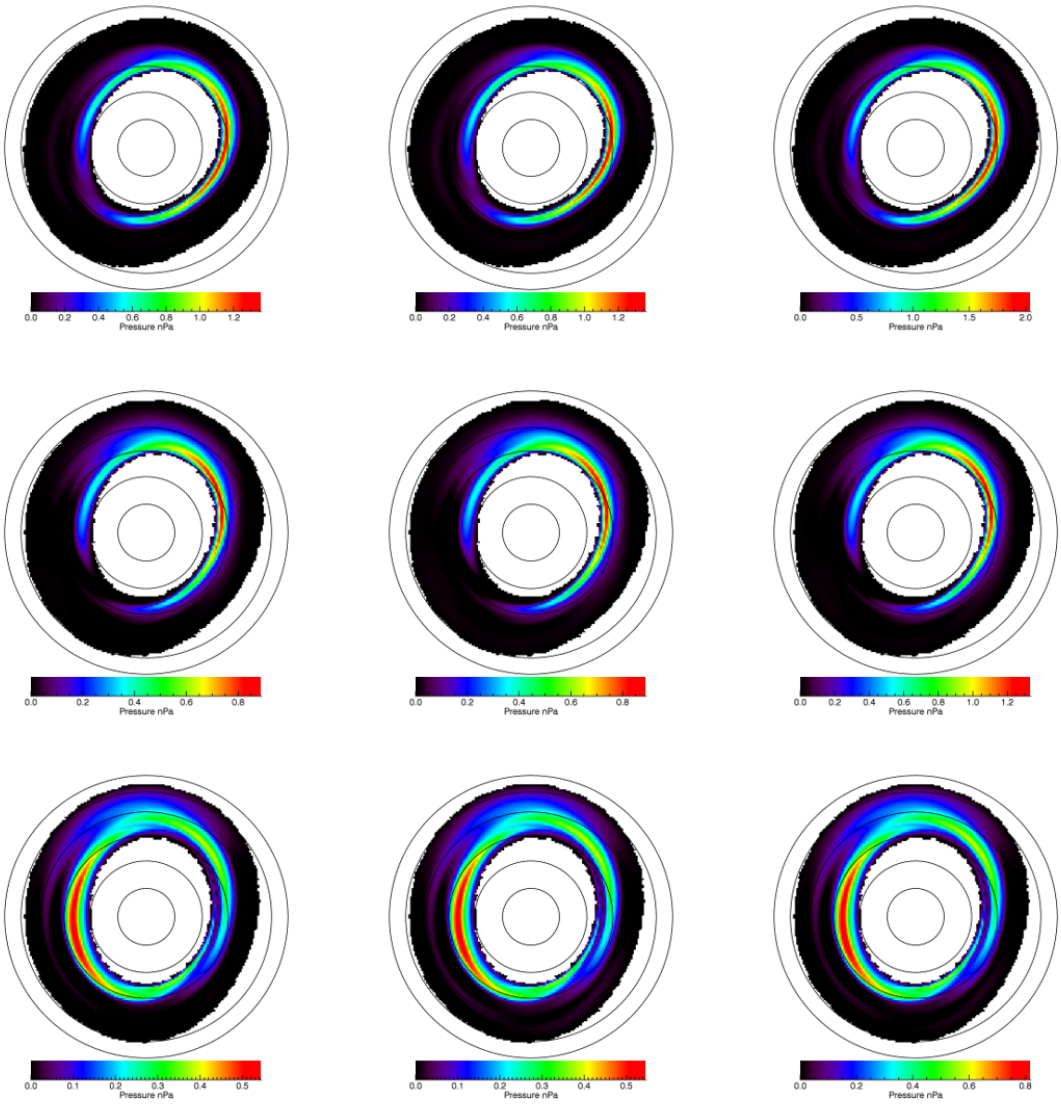

Figure 6.11: Pressure plots at northern ionosphere. Top Row: 21:00 UT. Middle Row: 22:00 UT. Bottom Row: 23:00 UT. Left Column: Parallel Component of Pressure. Middle Column: Perpendicular Component of Pressure. Right Column: Scalar Pressure.

remaining times. By 23:00 UT, the ”secondary” peak has become larger than the primary, and occupies much of the dayside.

Next are plotted the pressure distributions calculated from TWINS ENA measurements at the equatorial plane. Again, the left-most image is the parallel pressure, the central image is the perpendicular pressure, and the right-most image is the scalar pressure, which is the sum of the parallel and perpendicular pressures. Unlike the ionospheric pressure distributions, in this case the parallel and perpendicular pressure distributions are decidedly different. If the difference were negligible, as in the first set of pressure plots, there would be little point in exploring

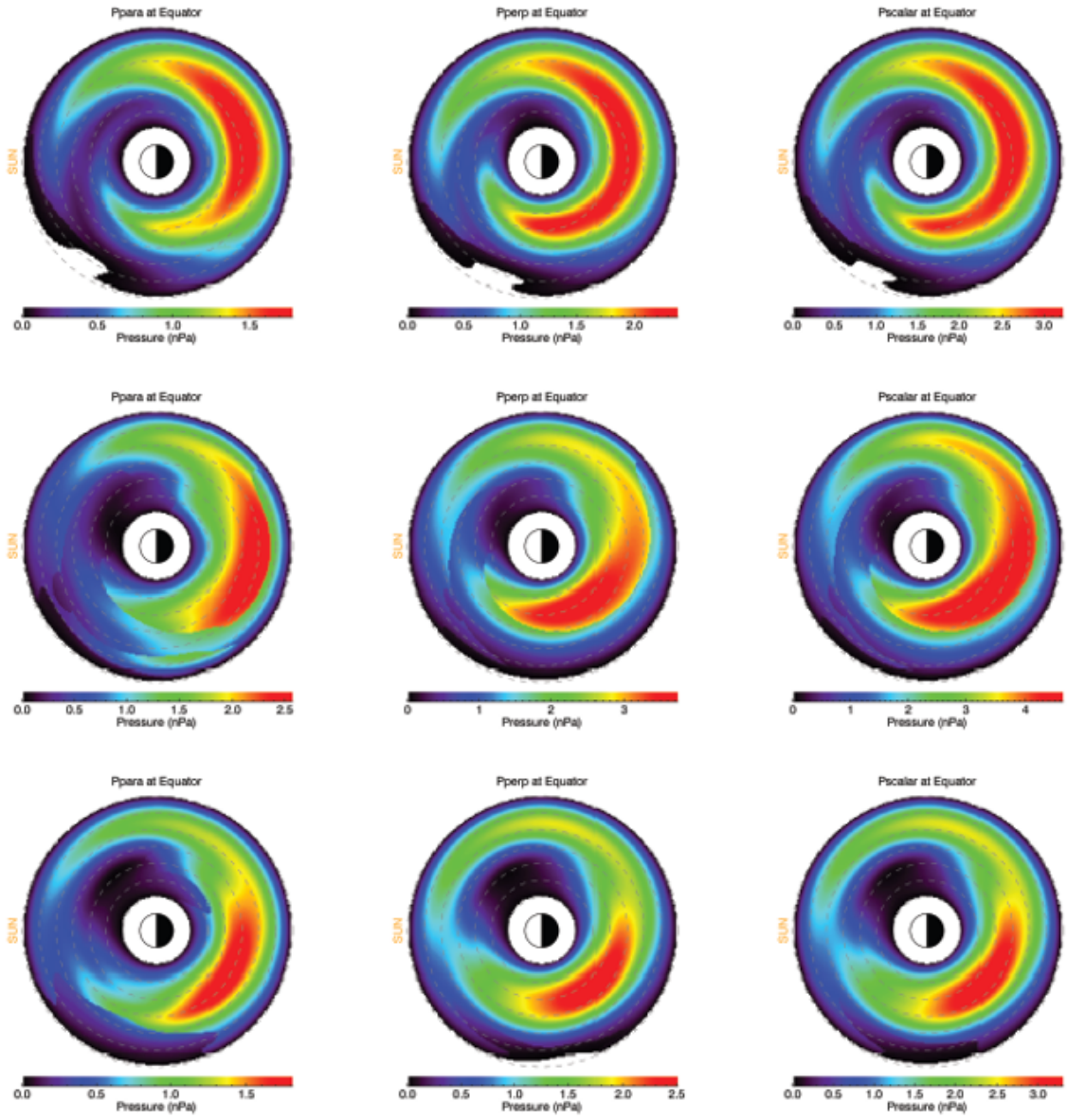

Figure 6.12: Equatorial Ion Pressure from TWINS ENA Measurements. Top Row: 05:00 UT. Middle Row: 07:00 UT. Bottom Row: 08:00 UT. Left Column: Parallel Component of Pressure. Middle Column: Perpendicular Component of Pressure. Right Column: Scalar Pressure.

the effects of anisotropy on FACs, since there would be essentially no anisotropy. These plots indicate, though, that the pressure anisotropy varies with position; near the ionosphere there is essentially no anisotropy, while farther from it, the anisotropy becomes important. While it would be tempting to say the effects are unimportant when calculating FACs at the ionosphere because the ionospheric anisotropy is so small, it is important to remember that the ionospheric FACs are dependent upon the integration over the magnetic field lines, beginning at the point of minimum magnetic field where anisotropic effects may be important. Thus, we cannot neglect

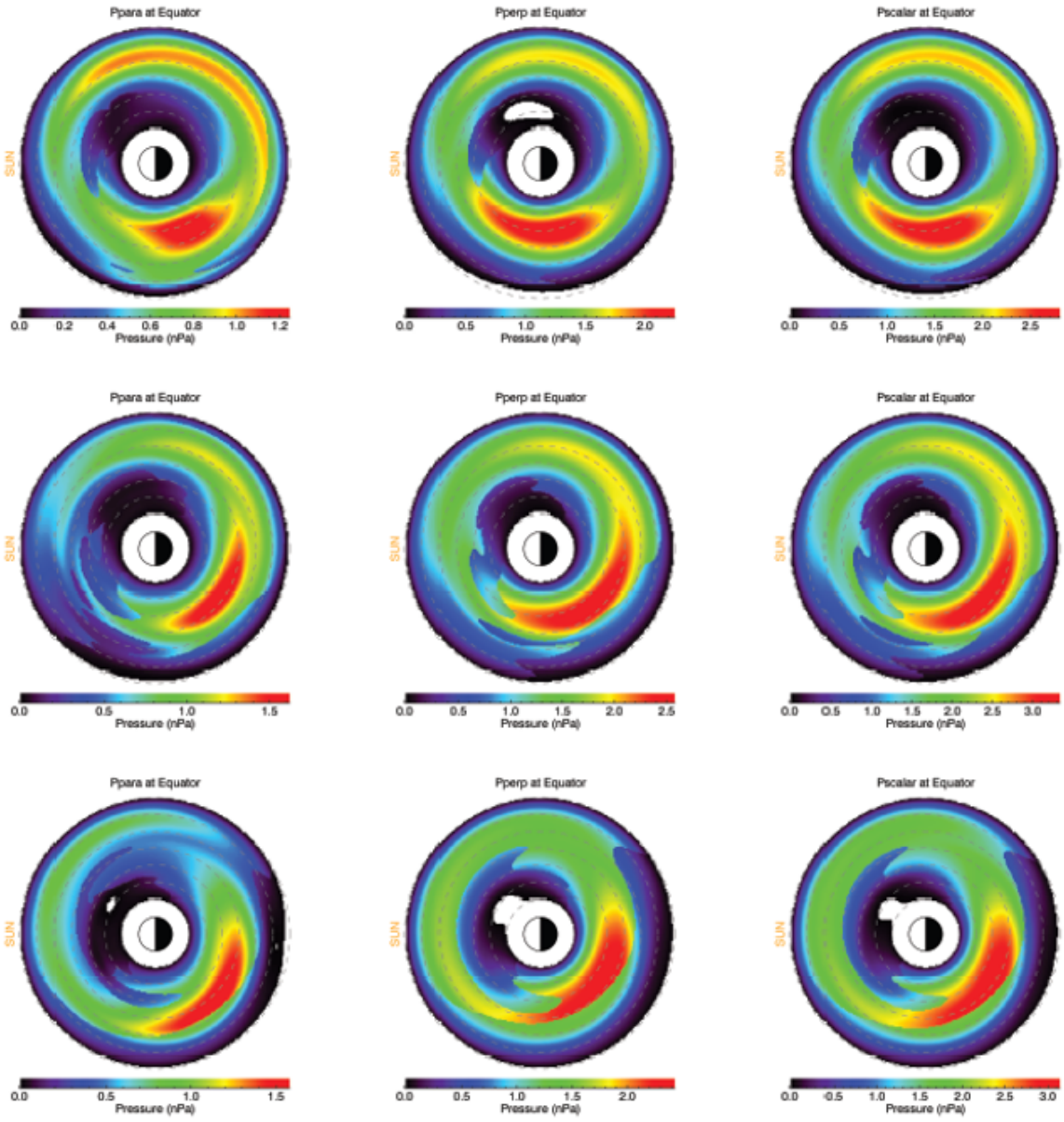

Figure 6.13: Equatorial Ion Pressure from TWINS ENA Measurements. Top Row: 09:00 UT. Middle Row: 10:00 UT. Bottom Row: 11:00 UT. Left Column: Parallel Component of Pressure. Middle Column: Perpendicular Component of Pressure. Right Column: Scalar Pressure.

equatorial pressure anisotropy even at the ionosphere. The change in anisotropy along magnetic field lines will be discussed in more detail in section 7.2.

An examination of the equatorial pressure reveals that the peak perpendicular pressure is always greater than the peak parallel pressure, though these peaks may not be in the same place. At 05:00 UT (left column of figure 6.12), the region of maximum perpendicular pressure occupies nearly all of the nightside between $L = 5$ and $L = 6$, with more a moderate pressure

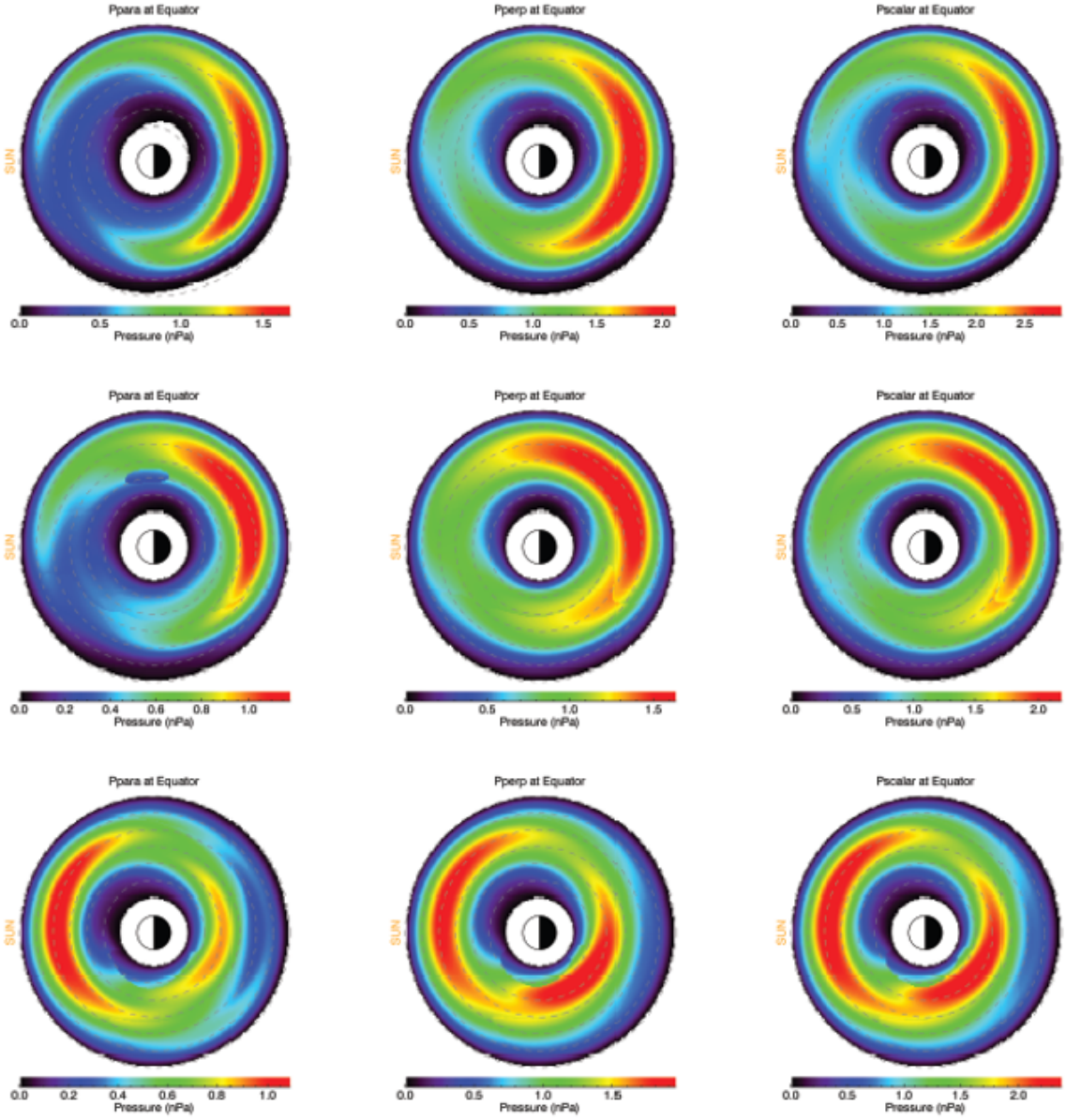

Figure 6.14: Equatorial Ion Pressure from TWINS ENA Measurements. Top Row: 21:00 UT. Middle Row: 22:00 UT. Bottom Row: 23:00 UT. Left Column: Parallel Component of Pressure. Middle Column: Perpendicular Component of Pressure. Right Column: Scalar Pressure.

region completely encircling the inner magnetosphere. The parallel pressure, on the other hand, occupies a somewhat smaller region of the nightside, and the region of moderate pressure is interrupted in the noon-dawn quadrant. These add to make the scalar pressure, which has a large region of high pressure, as in the perpendicular pressure case, and a moderate pressure region nearly encircling the equatorial plane, but with a small low pressure region near noon.

At 07:00 UT (middle column of figure 6.12), there is a widening region of maximum pressure, stretching radially from about $L = 3$ to $L = 6$ in some regions, though it covers a smaller

azimuthal region. By 08:00 UT (right column of figure 6.12), the region of maximum pressure is substantially smaller, occupying only the dusk-midnight quadrant. One can also observe a small secondary pressure peak, particularly in the perpendicular pressure, in the midnight-dusk region. This region becomes distinct by 09:00 UT (left column of figure 6.13), extending from midnight until well past dawn in all three pressure plots. At this time, the secondary maximum has become stronger relative to the primary maximum for the parallel pressure, though the magnitude of this peak is still greater for the perpendicular pressure. Further, the primary pressure maximum has moved to near dusk, nearly opposite to the secondary maximum.

At 10:00 UT (middle column of figure 6.13), the secondary pressure peak is still visible, especially in the parallel pressure. It is, however, weakening and beginning to merge with the primary region of maximum pressure. The primary region of maximum pressure has expanded in the azimuthal direction, now stretching through most of the dusk-midnight quadrant in the parallel pressure plot, and somewhat beyond this for the perpendicular pressure. By 11:00 UT (right column of figure 6.13), the secondary pressure peak has completely disappeared, and the region of maximum pressure is largely confined to the dusk-midnight quadrant in all plots.

During the recovery phase plots, the magnitude of the pressure has largely decreased from that during the main phase. In the plots for 21:00 UT and 22:00 UT (left and middle columns of figure 6.14), the region of highest pressure occupies most of the nightside, moving somewhat dawnward at 22:00 UT. By 23:00 UT (right column of figure 6.14), the nightside high pressure region has moved inward, with the edge closest to Earth at $L = 3$, and a second maximum region has appeared, occupying nearly all of the dayside. At this time, while the ion pressure is still considerably higher than during quiescent times, it is becoming much more uniformly distributed about the equatorial plane. This likely contributes to the near textbook appearance of the FACs at this time.

Chapter 7

Discussion

7.1 Integral Contributions to FACs

As noted in Chapter 5, FACs may be calculated either assuming an isotropic PAD, or using the anisotropic PAD measured by TWINS. If assuming PAD isotropy, the calculation simplifies considerably, reducing to a single integral term: $J_{\parallel Iso} = B(s_2)\int_{s_1}^{s_2}\frac{(\boldsymbol{\nabla}P\times\boldsymbol{\nabla}B)\cdot\hat{s}}{B^3}ds$ (equation 5.13). The calculation from the anisotropic PAD, however, involves integrating three terms: $J_{\parallel 1} = \frac{2B(s_2)}{1-\chi(s_2)}\int_{s_1}^{s_2}\frac{(\boldsymbol{\nabla}P_\perp\times\boldsymbol{\nabla}B)\cdot\hat{s}}{B^3}ds$, $J_{\parallel 2} = \frac{B(s_2)}{1-\chi(s_2)}\int_{s_1}^{s_2}\frac{(\boldsymbol{\nabla}\chi\times\boldsymbol{\nabla}B)\cdot\hat{s}}{B^2(1-\chi)}ds$ and $J_{\parallel 3} = \frac{B(s_2)}{\mu_0(1-\chi(s_2))}\int_{s_1}^{s_2}\frac{(\boldsymbol{\nabla}\chi\times\boldsymbol{\nabla}P_\perp)\cdot\hat{s}}{B(1-\chi)}ds$, where $J_{\parallel Aniso} = J_{\parallel 1} + J_{\parallel 2} + J_{\parallel 3}$ (see equation 5.12). Notice that $J_{\parallel 1}$ is very similar to $J_{\parallel Iso}$. This is to be expected, since $J_{\parallel 1}$ is the term that survives the assumption of isotropy; the other two terms both become zero. $J_{\parallel 1}$ is not identical to $J_{\parallel Iso}$, however. The two differ by a $1-\chi(s_2)$ factor outside the integral, and by the perpendicular pressure in the anisotropic PAD case, instead of the scalar pressure used by the isotropic PAD case. While the factor of $1-\chi(s_2)$ may play a more substantial role near the equatorial plane, the field aligned current density is typically very small in that region. At the ionosphere, while the FACs become much larger in magnitude, the value of χ usually drops to near zero (see section 7.2). Thus, this factor does not contribute substantially to differences between the isotropic and anisotropic PAD cases for ionospheric FACs. The more important difference lies in the use of the perpendicular pressure for the anisotropic PAD case. In the isotropic PAD case, the pressure remains constant along the field line, meaning $\boldsymbol{\nabla}P$ has no component parallel to the magnetic field. This is not generally true in the anisotropic PAD case. Thus, while $J_{\parallel Iso}$ and $J_{\parallel 1}$ become nearly identical in regions of low PAD anisotropy, there will still be differences in regions where the PAD anisotropy is important. The following plots illustrate how each integral term contributes to the ionospheric FACs.

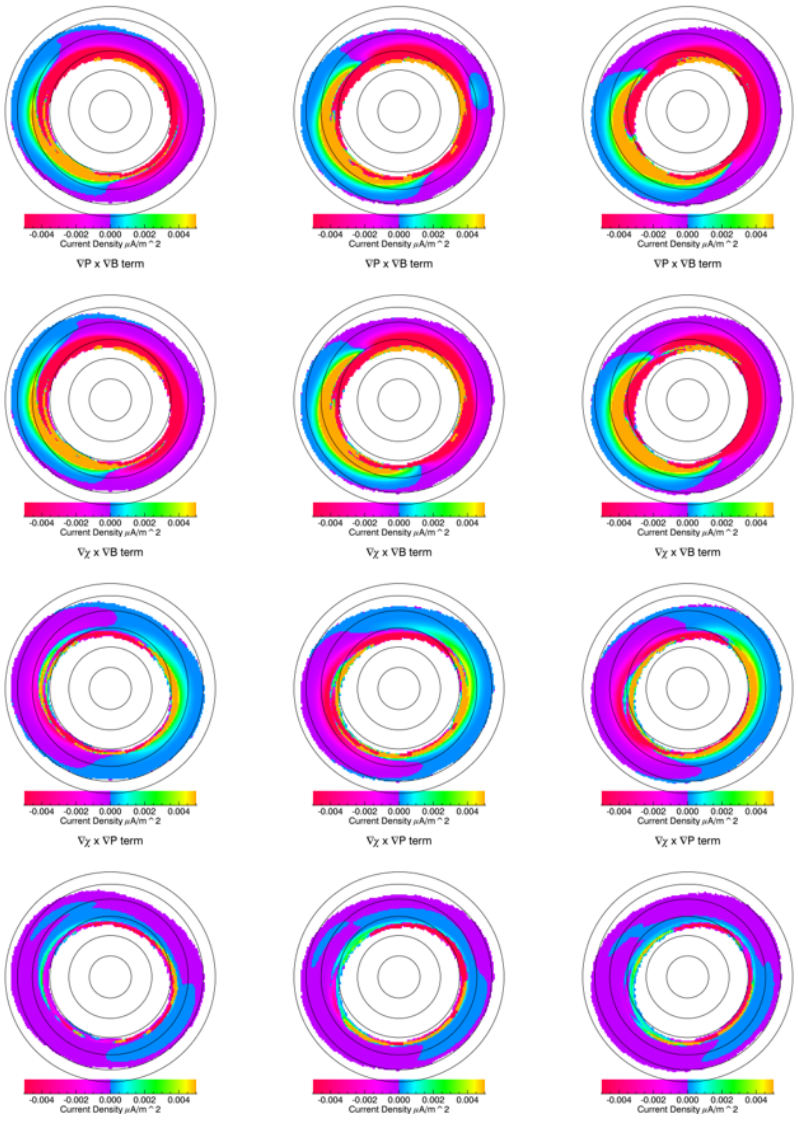

Figure 7.1: Left column: 0500UT. Center column: 0700UT. Right column: 0800UT. Top row: FACs at northern ionosphere calculated using TWINS PAD. Second row: FAC component due to $J_{\|1}$ term. Third row: FAC component due to $J_{\|2}$ term. Fourth row: FAC component due to $J_{\|3}$ term. Positive currents - blue, orange, and green - point inward, while negative currents - red and purple - point outward. The Sun is to the left in all images.

The plots show the FACs at the northern ionosphere due to each term in the anisotropic integral. Each column plots a different time, with the top row plotting the FACs calculated using the anisotropic PAD. The second through fourth rows plot the FACs due to the $J_{\|1}$, $J_{\|2}$, and $J_{\|3}$ terms, respectively. As with figures 6.6, 6.7, and 6.8, the FACs are capped at ± 0.005 $\mu A/m^2$ to show the fine details in the regions with small current densities. The necessity for

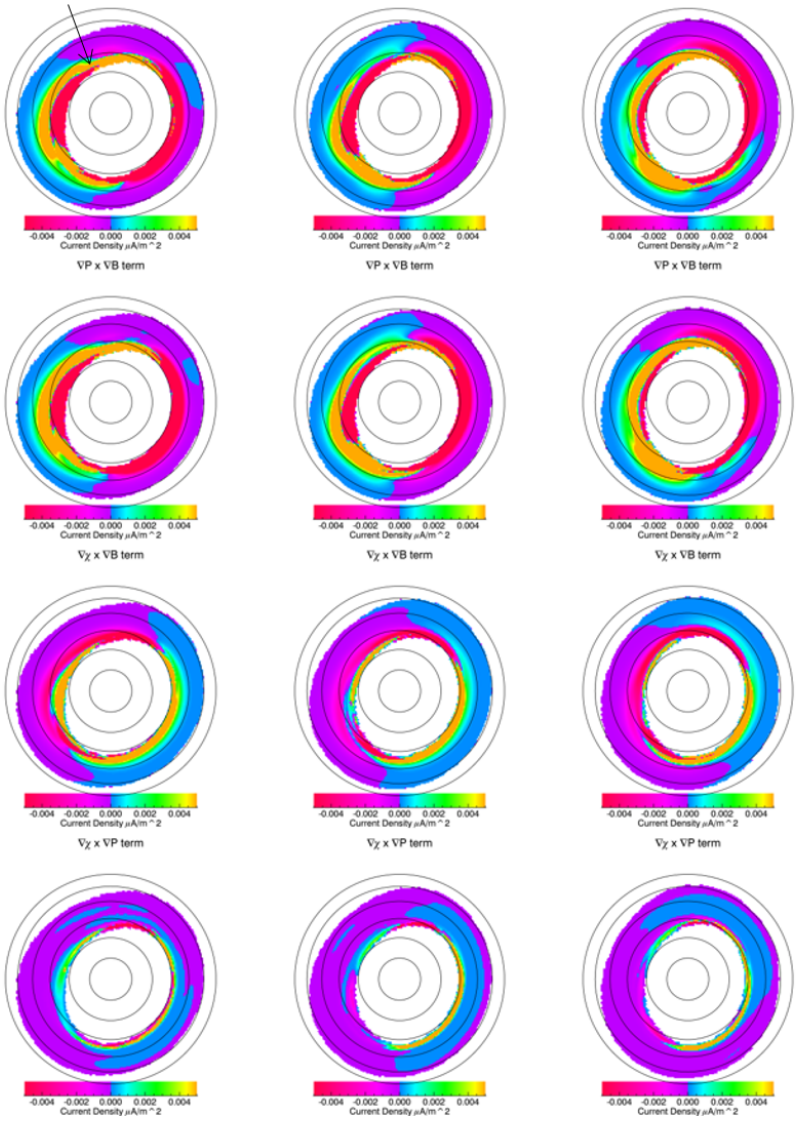

Figure 7.2: Left column: 0900UT. Center column: 1000UT. Right column: 1100UT. Top row: FACs at northern ionosphere calculated using measured PAD. Second row: FAC component due to $J_{\|1}$ term. Third row: FAC component due to $J_{\|2}$ term. Fourth row: FAC component due to $J_{\|3}$ term. Positive currents - blue, orange, and green - point inward, while negative currents - red and purple - point outward. The Sun is to the left in all images.

these small limits is easily seen in the plots; those showing the $J_{\|2}$ and $J_{\|3}$ terms are much lower magnitude than the others, and their details would be washed out with a courser scale.

At 05:00 UT (left column of 7.1), the FACs are almost entirely due to the $J_{\|1}$ term; the FACs due to this term are nearly identical to the total FACs. The other two terms are very small by comparison, but the details are interesting nonetheless. The $J_{\|2}$ term, in particular, is interesting for being essentially opposite to the $J_{\|1}$ term, though of much smaller magnitude.

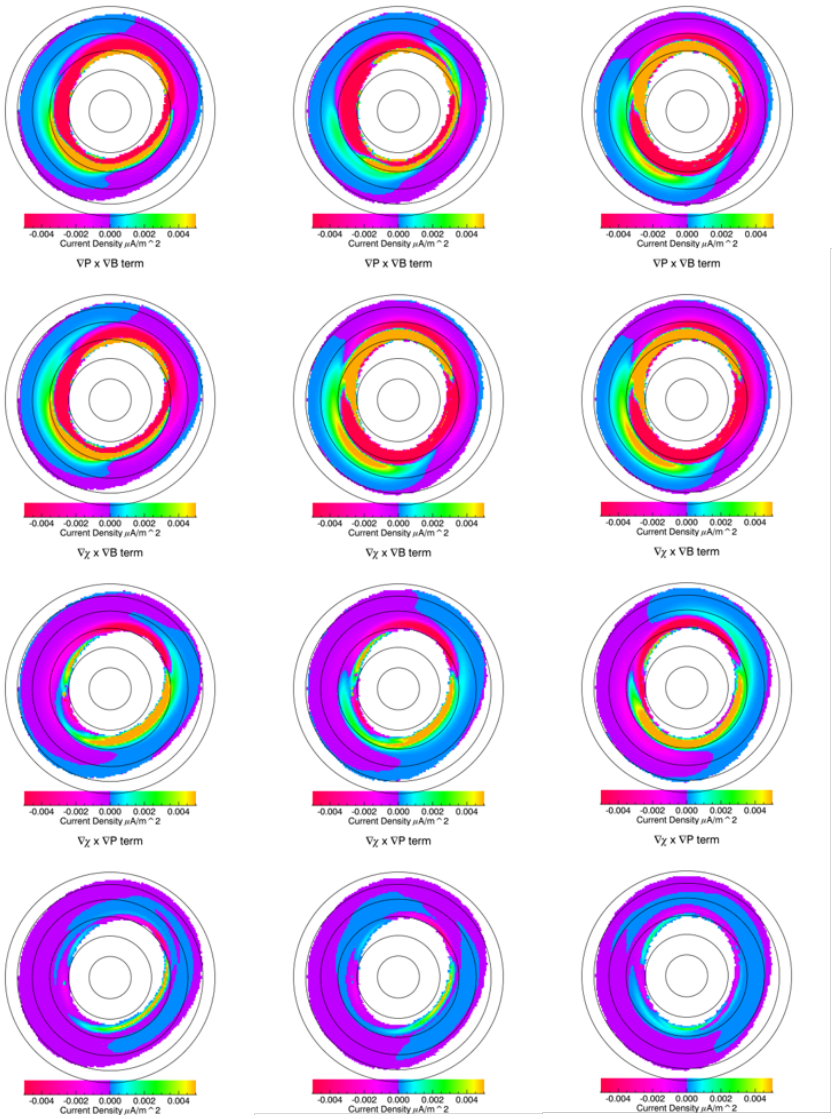

Figure 7.3: Left column: 2100UT. Center column: 2200UT. Right column: 2300UT. Top row: FACs at northern ionosphere calculated using measured PAD. Second row: FAC component due to $J_{\|1}$ term. Third row: FAC component due to $J_{\|2}$ term. Fourth row: FAC component due to $J_{\|3}$ term. Positive currents - blue, orange, and green - point inward, while negative currents - red and purple - point outward. The Sun is to the left in all images.

The $J_{\|3}$ term contributes only exceedingly small currents to the total except at the highest measurable latitudes.

The FACs at 07:00 UT (middle column of figure 7.1) contain an interesting feature in the inward current region at mid to low latitudes in the midnight-dawn quadrant. This region does not appear in the isotropic PAD case, and is one of the most striking differences between the two cases. As previously mentioned, the isotropic PAD case solely has the $J_{\|1}$ term, and

while there is a dependence on χ in this term in the anisotropic PAD case, the dependence is only upon χ at the ionosphere, which is exceedingly small (see equation 5.12). Thus, it is no surprise that the FACs due to the $J_{\parallel 1}$ term look very similar to those of the isotropic PAD case, and do not have the inward current region near midnight. This region is due to the strong inward currents in the midnight-dawn quadrant of the $J_{\parallel 3}$ term. The currents due to this term is generally opposite to $J_{\parallel 2}$, but in this region they are also larger in magnitude. This leads to an unusual feature that differs considerably from the isotropic PAD case.

By 08:00 UT (right column of figure 7.1), the inward region discussed at 07:00 UT is gone. While the inward FACs due to the $J_{\parallel 3}$ term in this region appear to be slightly weaker, the primary reason appears to be an increase to the magnitude of the outward current due to the $J_{\parallel 1}$ term. These factors combine to make the total FACs in this region weaker than the $\boldsymbol{\nabla} P \times \boldsymbol{\nabla} B$ contribution, but still outward.

The FACs at 09:00 UT (left column of figure 7.2) are another interesting case in which there is a region of inward current at low latitude just past midnight. As with the 07:00 UT case, this region appears in the anisotropic PAD case but not the isotropic PAD case. This case is particularly interesting because a small region of this current is already apparent in the $J_{\parallel 1}$ term. As previously mentioned, this term is the only one that contributes to the isotropic PAD case, yet this region of current does not appear there. There are two differences between $J_{\parallel 1}$ and $J_{\parallel Iso}$: one due to a $1 - \chi(s_2)$ factor in the denominator outside the integral, where s_2 is the point at which the current is being calculated, the other a difference between $\boldsymbol{\nabla} P_\perp$ in the anisotropic PAD case, and $\boldsymbol{\nabla} \frac{P}{2}$ in the isotropic PAD case. The $1 - \chi$ term, of course, is simply unity in the isotropic PAD case, and because χ is generally very small at the ionosphere, it is usually very close to unity in the anisotropic PAD case as well. At this particular time, and in this specific region, however, $\chi(s_2)$ becomes large enough to make a difference in this term. Further, the relatively large χ at the ionosphere indicates a high degree of PAD anisotropy along the magnetic field line that intersects the ionosphere here. This indicates that $\boldsymbol{\nabla} P_\perp$ behaves substantially differently from the isotropic $\boldsymbol{\nabla} P$ term in this region. In addition, the $J_{\parallel 3}$ term adds an addition inward current to this region, leading to a wider zone of inward current at low latitude just past midnight.

It is also at 09:00 UT that another difference between the isotropic and anisotropic PAD cases first appears. At this time, the broad region of relatively weak inward current on the dayside connects with the strong, high latitude inward current near dawn, as indicated by the arrow in figure 7.2. This does not happen in the isotropic PAD case until 11:00 UT. As with the previously discussed region, this feature is apparent in the $J_{\parallel 1}$ term. Again, this indicates a substantial degree of anisotropy in this region. This difference continues through 10:00 UT (middle column of figure 7.2), though the region of inward current near midnight is no longer present by this time. By 11:00 UT (right column of 7.2), the region connecting the dayside inward current to the region of high latitude large current near dawn is present in both the isotropic and anisotropic PAD cases.

There are few surprises during the recovery phase of this storm. In all plots, the total FACs are very similar to the contribution due to the $J_{\parallel 1}$ term, with the contribution from the $J_{\parallel 2}$ term generally serving to lessen the magnitude of the currents somewhat, and the contribution from the $J_{\parallel 3}$ term being a minor perturbation. The primary difference between the FACs in the isotropic and anisotropic PAD cases is the thin band of inward current stretching across the nightside, connecting both ends of the dayside inward current region, as well as the high latitude current region near dawn. This difference appears in the $J_{\parallel 1}$ term, and is due to a difference in the behavior of $\boldsymbol{\nabla} P_{\perp}$ and $\boldsymbol{\nabla} P$.

7.2 Values Along Magnetic Field Lines

The following plots show how several quantities vary along magnetic field lines. In each plot, a given quantity is traced from the equatorial plane to the northern ionosphere along a magnetic field line. This is done for several lines at 07:00 UT. This time was chosen because of the unusual FAC feature near dusk that clearly differentiates the isotropic and anisotropic PAD cases. The line positions have been chosen to give a representative view of the changes in these quantities over the northern hemisphere.

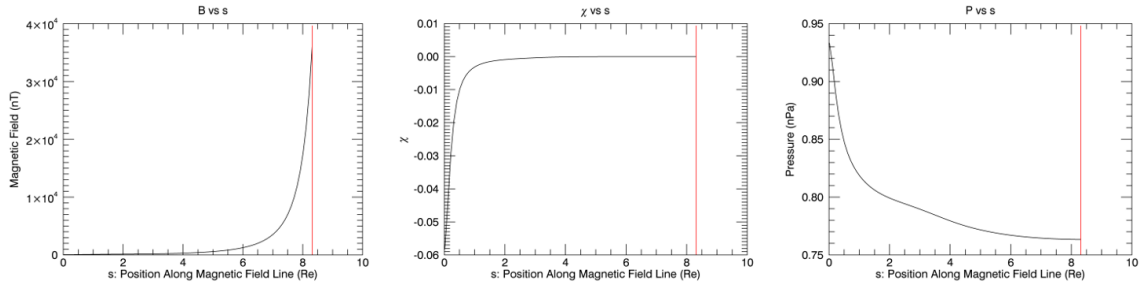

Figure 7.4: Left: Magnetic Field (nT), Middle: χ, Right: Scalar Pressure calculated with TWINS PAD (nPa). On the x-axis, zero represents the point at which the magnetic field line crosses the equatorial plane. The red line is the point at which it intersects the ionosphere.

Figure 7.4 plots magnetic field, χ, and the anisotropic scalar pressure along the field line intersecting the ionosphere at latitude 60° and MLT of 1h 20m. This field line enters the ionosphere in the high latitude region of strong inward current that extends through the midnight-dawn quadrant. The magnetic field is substantially weaker near the equatorial plane than near the ionosphere. This is to be expected; a purely dipole field varies as r^{-3}, and while this is not a dipolar field, it does not differ radically. χ, on the other hand, has its greatest magnitude near the equatorial plane, though it is negative. It approaches zero very rapidly, as the parallel and perpendicular pressures become both smaller and nearer in magnitude to each other. By the ionosphere, the parallel and perpendicular pressures are nearly the same. The final plot in this set shows the anisotropic pressure vs position. This, too, has the greatest magnitude near the equator; positive this time. It declines rapidly as the field line leaves the equatorial plane, but more gradually within 7 R_E of the ionosphere, measured along the field line. It is interesting to note that the pressure behaves in this manner. As previously noted, the $\left[\frac{B(s_0)}{B(s)}\right]$ factor tends to become very small as the ionosphere is approached. Except in unusual circumstances, this tends to make the pressure decrease with proximity to the ionosphere.

The next set of plots, figure 7.5, emphasizes the behavior of pressure along a field line. The left hand plot shows all pressures: parallel, perpendicular, and scalar using the anisotropic PAD, and pressure using isotropic PAD. In the isotropic PAD case, the pressure remains constant along the field line, resulting in a straight, horizontal line on the plot. The scalar pressure is identical to that in the previous plot, and is simply the sum of the parallel and perpendicular pressures. The parallel and perpendicular pressures both follow a similarly shaped path,

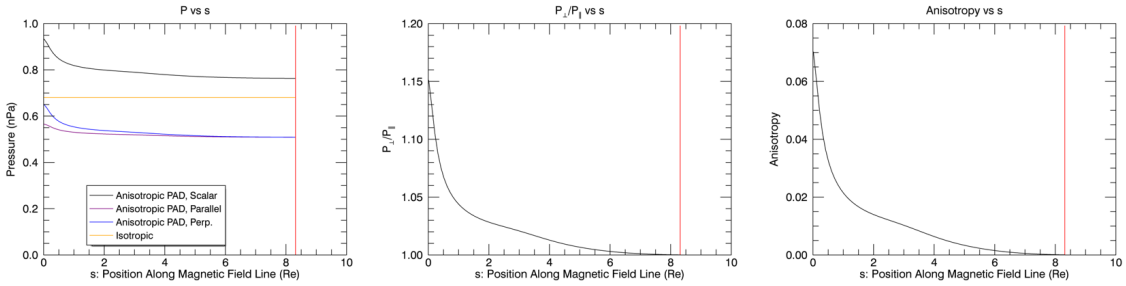

Figure 7.5: Left: All Pressures, plotted together (nPa), Middle: $P_\perp/P_\parallel$, Right: Pressure Anisotropy. On the x-axis, zero represents the point at which the magnetic field line crosses the equatorial plane. The red line is the point at which it intersects the ionosphere.

beginning at relatively high pressure near the equator, and dropping to a lower value near the ionosphere. However, the perpendicular pressure is always greater than the parallel pressure, though they approach the same value at the ionosphere. This situation, with $P_\perp > P_\parallel$ is far more common than the opposite, and requires the ion density to decrease as one approaches the ionosphere, as shown by equations 70 and 71 of Parker [1957].

The central plot shows $P_\perp/P_\parallel$ vs position along the field line. This shows that the difference between $P_\parallel$ and $P_\perp$ is greatest near the equatorial plane, with $P_\perp = 1.15P_\parallel$ there, and drops very rapidly moving toward the ionosphere. While $P_\perp$ is 15% greater than $P_\parallel$ at the equatorial plane, the difference is not tremendous. It makes the maximum anisotropy along this field line only approximately 0.07, as shown in the right hand plot. The anisotropy is defined in this work as $A = \frac{P_\perp - P_\parallel}{P_\perp + P_\parallel}$. Thus, $A = 1$ means the pressure is entirely perpendicular, $A = -1$ means the pressure is entirely parallel, and $A = 0$ means $P_\parallel = P_\perp$. In this case, the anisotropy is very small, so while the pressure is not isotropic, isotropy is not a bad approximation. Near the ionosphere, the anisotropy approaches zero, and the isotropic assumption becomes excellent.

Figure 7.6 is a series of current density plots, all calculated using the anisotropic PAD, and again along the same field line. The top left plot shows the field aligned current density along the field line. Near the equator, $J_\parallel$ is very small, and it remains so over most of the field line, not increasing substantially until it is within $1R_E$ of the ionosphere. While the standard description of Region 2 field aligned currents typically shows them moving along field lines all the way to the equatorial plane, this plot indicates that this is not the case. The current does not become strongly field aligned until near the ionosphere.

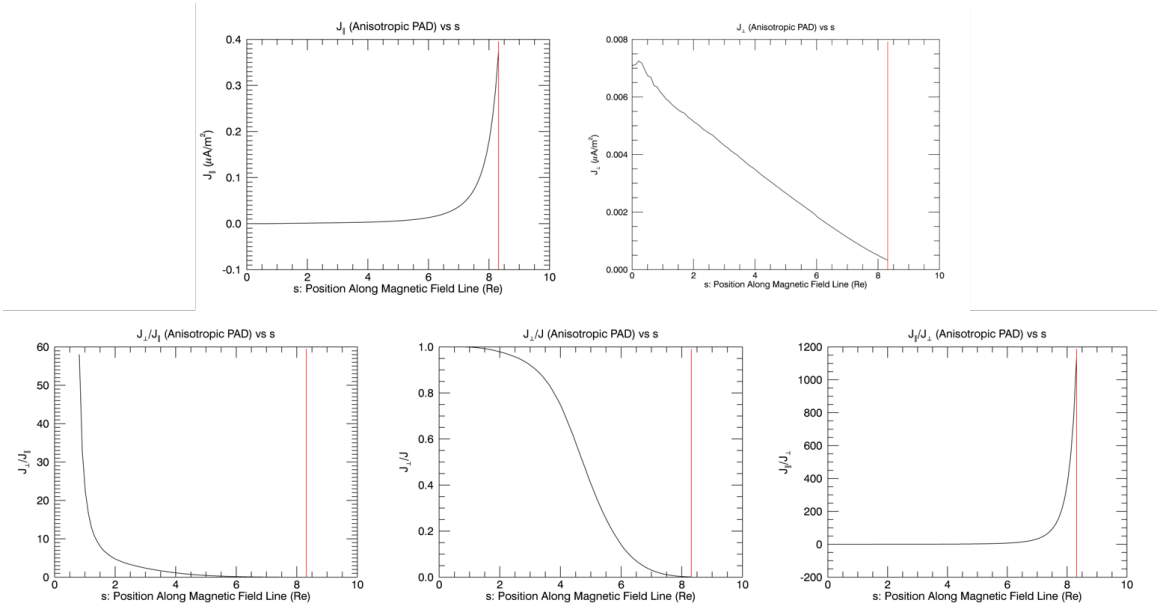

Figure 7.6: Current density calculated from anisotropic PADs. Top left: Field aligned component of current density. Positive indicates current is parallel to B field, negative indicates anti-parallel. Top right: Perpendicular component of current density. Bottom left: Perpendicular component divided by parallel component of current density. Since $J_{\|}$ goes to zero near the equatorial plane, this plot is truncated. Bottom middle: The perpendicular component of the current density as a fraction of the magnitude of the current density. Bottom right: The field aligned component divided by the perpendicular component of the current density. On the x-axis, zero represents the point at which the magnetic field line crosses the equatorial plane. The red line is the point at which it intersects the ionosphere.

The rest of the plots in this figure confirm this finding. The top right plot shows how the perpendicular current density varies along the magnetic field line. $J_{\perp}$ is greatest near the equatorial plane, decreasing almost linearly toward the ionosphere. Note that while the magnitude of $J_{\|}$ at its maximum is much smaller than the maximum $J_{\perp}$, $J_{\|}$ is greater near the equatorial plane. This can be seen more clearly in the bottom row of plots. The bottom left plot shows $J_{\perp}/J_{\|}$ along the filed line, while the bottom right plots shows the inverse. These plots indicate that the current density is nearly perpendicular to the magnetic field line in the vicinity of the equatorial plane, but very nearly field aligned near the ionosphere. The bottom center plot shows what fraction of the total current is perpendicular to the field line. It shows that the current is dominated by the perpendicular component for a relatively wide region around the equatorial plane, and dominated by the field aligned component for a smaller region near the ionosphere. There is a region between two and five R_E from the ionosphere, along the

filed line, where both components play an important role, with the relative magnitudes varying linearly.

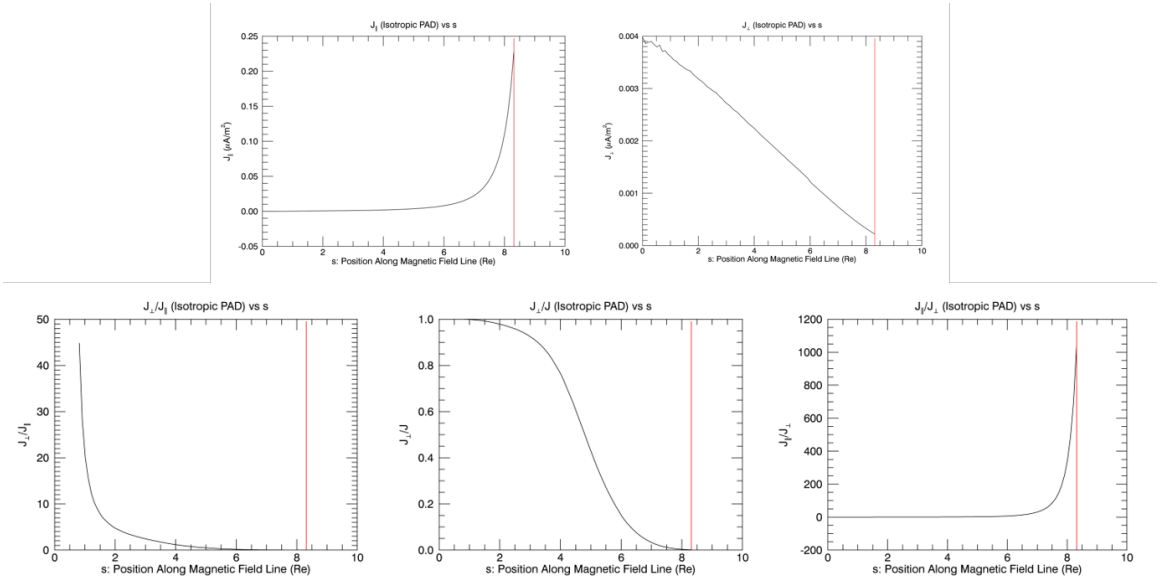

Figure 7.7: Current density calculated from isotropic PADs. Top left: Field aligned component of current density. Positive indicates current is parallel to B field, negative indicates anti-parallel. Top right: Perpendicular component of current density. Bottom left: Perpendicular component diveded by parallel component of current density. Since $J_{\|}$ goes to zero near the equatorial plane, this plot is truncated. Bottom middle: The perpendicular component of the current density as a fraction of the magnitude of the current density. Bottom right: The field aligned component divided by the perpendicular component of the current density. On the x-axis, zero represents the point at which the magnetic field line crosses the equatorial plane. The red line is the point at which it intersects the ionosphere.

Figure 7.7 shows the same plots as figure 7.6, but using currents derived from the isotropic pressure distribution. The current density plots on the top row show similar behavior to that seen in the anisotropic case, but the magnitude of both components of the current density is smaller. This is to be expected, since the isotropic pressure plotted in figure 7.5 shows the isotropic pressure is smaller than the anisotropic scalar pressure. The relative behavior of the current density components is essentially the same, though, with the region near the equatorial plane dominated by the perpendicular component, and the region near the ionosphere highly field aligned.

Figure 7.8 shows the field aligned current density due to each of the integral components that goes into the calculation. Recall from the Derivation chapter, equation 5.12, that there are

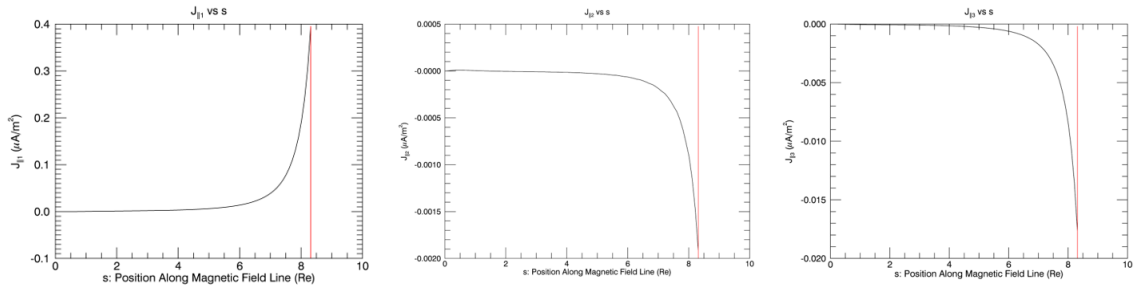

Figure 7.8: Components of current density calculated from anisotropic PADs. Left: $J_{\|}$ component due to $J_{\|1}$ term. Middle: $J_{\|}$ component due to $J_{\|2}$ term. Right: $J_{\|}$ component due to $J_{\|3}$ term. On the x-axis, zero represents the point at which the magnetic field line crosses the equatorial plane. The red line is the point at which it intersects the ionosphere.

three terms which combine to give the total field aligned current density. These plots show the contribution from each term along the magnetic field line.

The left hand plot shows the current due to the $J_{\|1}$ term. This is the only term appearing in the isotropic calculation, and generally is the most important contribution to the field aligned current density. As the plot indicates, this component behaves like the $J_{\|}$ plot in figure 7.6, with very little field alinged current density near the equatorial plane, increasing rapidly near the ionosphere. The magnitude of the current density due to this component is very similar to the total; if this were the only component used, it would be a very good approximation. Because this is the component appearing in the isotropic case, it is not surprising that the two ionospheric FAC cases (figure 6.3) look very similar in this region.

The middle plot of figure 7.8 shows the field aligned current density due to the $J_{\|2}$ term. Like the first term, the magnitude of the current density due to this term remains near zero until near the ionosphere, at which point it rapidly increases. Unlike the first term, however, this term is negative; that is, it is an outward current, while that due to the first term points inward. This means it acts to reduce the net field aligned current density. However, it is much smaller in magnitude than the current density due to the $J_{\|1}$ term - roughly 0.05% its value. Thus, while this term acts to reduce the magnitude of the field aligned current, it is only a small perturbation whose effect may be neglected in this case.

The right hand plot shows the current density due to the $J_{\|3}$ term. Like the others, the magnitude of the current density due to this term is very small near the equatorial plane, and

becomes large only near the ionosphere. The shape of the curve is nearly identical to those of the other terms, and like the $J_{\parallel 2}$ term, it is an outward current. Its magnitude is roughly ten times that of the $J_{\parallel 2}$ term, but is still much smaller than the $J_{\parallel 1}$ term - about 0.5% of its magnitude. Thus, while it is a greater perturbation than the $J_{\parallel 2}$ term, it is still negligible in this case. Thus, the field aligned current density along this field line is nearly entirely due to the $J_{\parallel 1}$ term.

Next, the region of inward current at low latitudes near midnight will be examined. This region is particularly interesting because it does not appear in the isotropic PAD plots, indicating that an assumption of isotropy may miss important details. The following plots will examine the magnetic field line intersecting the ionosphere at latitude 45° and MLT 1h 20m.

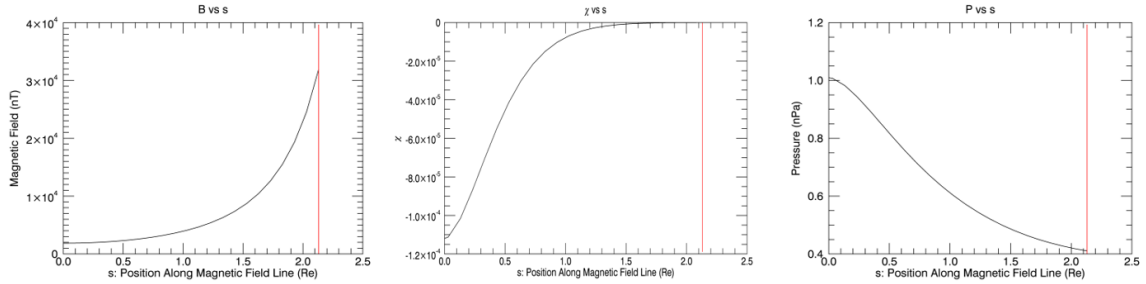

Figure 7.9: Left: Magnetic Field (nT), Middle: χ, Right: Scalar Pressure calculated with TWINS PAD (nPa). On the x-axis, zero represents the point at which the magnetic field line crosses the equatorial plane. The red line is the point at which it intersects the ionosphere.

Figure 7.9 again shows the magnetic field, χ, and anisotropic scalar pressure plotted along the magnetic field line. An important observation regarding these plots is that the magnetic field line is substantially shorter. The point of interest at the ionosphere is at considerably lower latitude, meaning the path length to the equatorial plane is shorter. This path is also more nearly dipolar, and maps to a point on the equatorial plane much closer to Earth than the previous set of plots.

Like in the previous plots, the magnetic field is weakest near the equatorial plane, and strongest at the ionosphere. However, the magnetic field increases more uniformly in this case, reflecting the dipole-like form of the magnetic field line. While the magnetic field in figure 7.4 only deviates a small amount from the dipole, this deviates much less.

χ in this plot is smaller in magnitude than figure 7.4 due to the larger magnetic field, particularly in the vicinity of the equatorial plane. Further, the pressure is smaller. This combination of a smaller pressure and larger magnetic field leads to a much smaller set of values for χ. χ is still negative, however, meaning that $P_\perp > P_\parallel$, and moving toward the ionosphere will see the pressure decrease [Parker 1957].

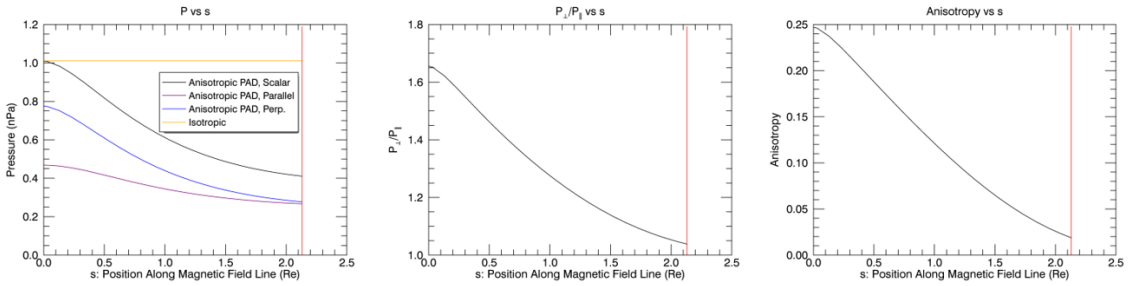

Figure 7.10: Left: All Pressures, plotted together (nPa), Middle: $P_\perp/P_\parallel$, Right: Pressure Anisotropy. On the x-axis, zero represents the point at which the magnetic field line crosses the equatorial plane. The red line is the point at which it intersects the ionosphere.

The left hand plot in figure 7.10 shows parallel and perpendicular pressure calculated from the anisotropic PAD, the total pressure, as well as the pressure calculated using the isotropic PAD. Like before, note that in the isotropic PAD case, pressure remains constant along the field line. Also like before, both parallel and perpendicular pressures decrease approaching the ionosphere. In this case, however, the parallel and perpendicular pressures are not so nearly equal at the ionosphere. There is a much smaller difference between them than at the equatorial plane, but they are never approximately equal. This is reiterated in the right hand plot, which shows anisotropy. The anisotropy along this field line is much greater than the previous. It has approximately three times the value at the equatorial plane, and decreases much more slowly approaching the ionosphere, such that it is still substantial upon reaching it. This is a region in which the FACs for the isotropic and anisotropic PAD cases are considerably different, with the net currents pointing in opposite directions. Thus, it is to be expected that the anisotropy is unusually high in this region, and finding it to be so increases the confidence that this is a real effect due to anisotropy.

The plots in figure 7.11 all pertain to current densities calculated using anisotropic PADs. The top left plot shows the field aligned component of the current density, which is positive

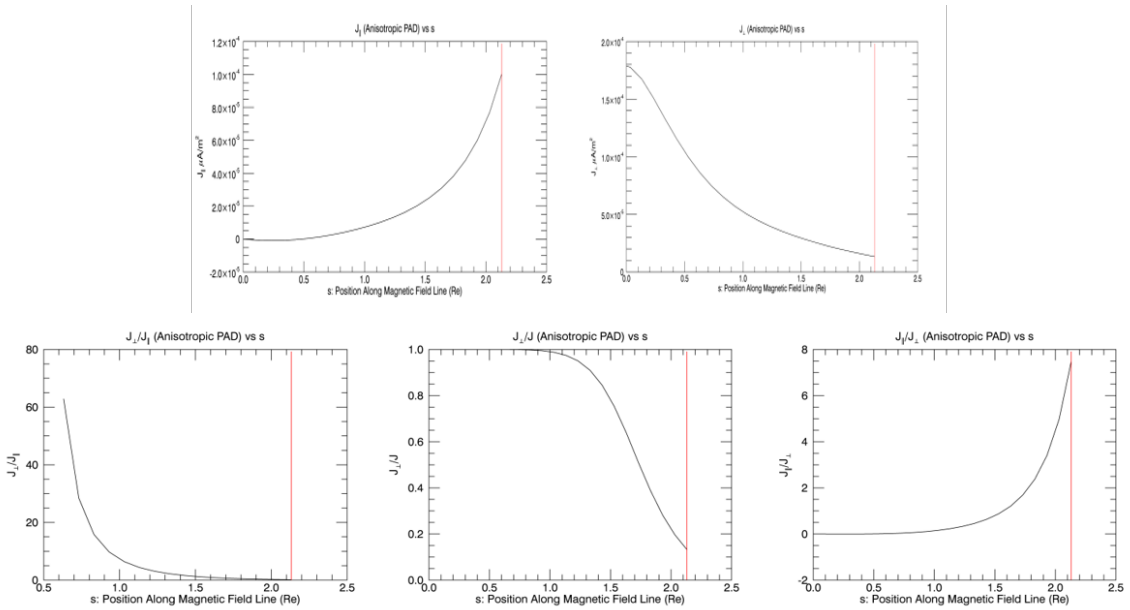

Figure 7.11: Current density from anisotropic PADs. Top left: Field aligned component of current density. Positive indicates current is parallel to B field, negative indicates anti-parallel. Top right: Perpendicular component of current density. Bottom left: Perpendicular component divided by parallel component of current density. Since $J_{||}$ goes to zero near the equatorial plane, this plot is truncated. Bottom middle: The perpendicular component of the current density as a fraction of the magnitude of the current density. Bottom right: The field aligned component divided by the perpendicular component of the current density. On the x-axis, zero represents the point at which the magnetic field line crosses the equatorial plane. The red line is the point at which it intersects the ionosphere.

and increases approaching the ionosphere, though it remains quite small even there. The top left plot shows the magnitude of the perpendicular component of the current density. As in the previous example, it is greatest near the equatorial plane, and becomes smaller approaching the ionosphere. It is interesting to note, however, that the perpendicular current density does not become vanishingly small at the ionosphere, unlike in the previous example. The bottom row compares the components of the current density to see their relative behaviors. The left hand plot shows $J_{\perp}/J_{||}$, which is very large near the equator, and small near the ionosphere. The right hand plot shows $J_{||}/J_{\perp}$, which behaves in the opposite manner; large near the ionosphere, and very small near the equatorial plane. These indicate that, as in the previous example, the field aligned component dominates near the ionosphere, while the perpendicular component dominates near the equatorial plane. The center plot on the bottom row reiterates this. This plot shows the fraction of the total current moving perpendicularly to the magnetic field line.

Near the ionosphere, essentially all of it is perpendicular. Beginning about 1 R_E from the ionosphere, though, this fraction begins to decrease, as more current moves parallel to the field line. Unlike in the previous example, however, the perpendicular component never becomes negligible; approximately 15% of the current density remains perpendicular to the field line at the ionosphere.

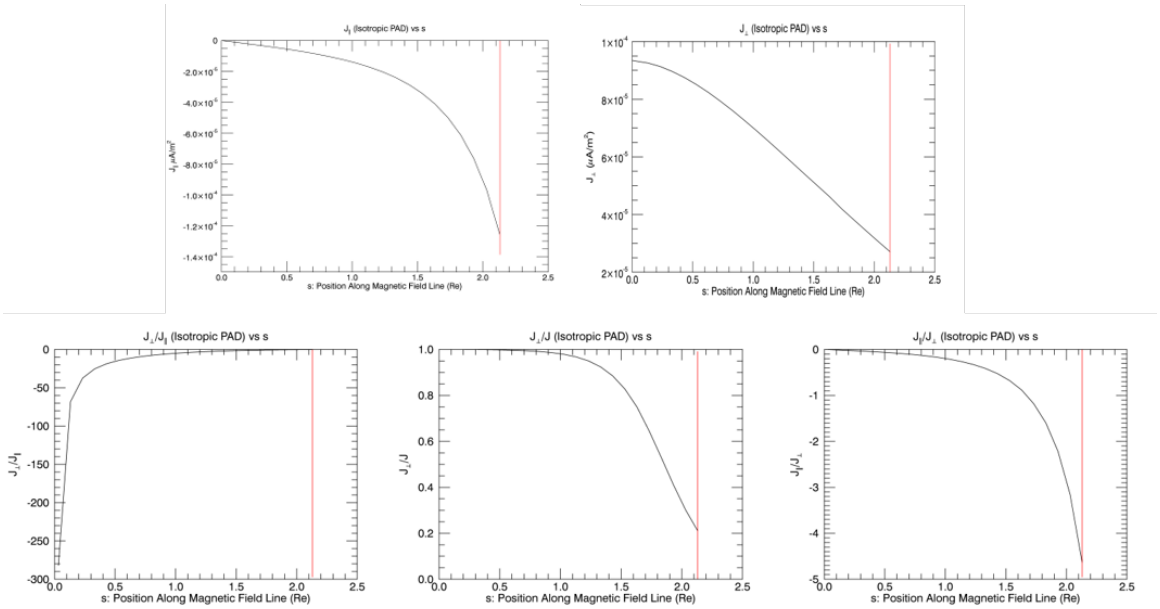

Figure 7.12: Current density from isotropic PADs. Top left: Field aligned component of current density. Positive indicates current is parallel to B field, negative indicates anti-parallel. Top right: Perpendicular component of current density. Bottom left: Perpendicular component diveded by parallel component of current density. Since $J_{||}$ goes to zero near the equatorial plane, this plot is truncated. Bottom middle: The perpendicular component of the current density as a fraction of the magnitude of the current density. Bottom right: The field aligned component divided by the perpendicular component of the current density. On the x-axis, zero represents the point at which the magnetic field line crosses the equatorial plane. The red line is the point at which it intersects the ionosphere.

The plots in figure 7.12 all pertain to current densities calculated using iostropic PADs. The top left plot shows the field aligned component of the current density. As previously mentioned, the field aligned current density flows out of the ionosphere in the isotropic case, opposite to the anisotropic case. It behaves similarly in terms of magnitude, increasing from near zero near the equator to a maximum at the ionosphere.

The top right plot shows the magnitude of the perpendicular current density calculated using isotropic pressure. As in the previous example, the perpendicular current density is greatest

near the equatorial plane, becoming much smaller near the ionosphere. Unlike the anisotropic case, it decreases in a nearly linear manner over the field line. It also becomes substantially smaller near the ionosphere.

The bottom leftt hand plot shows the magnitude of $J_\perp/J_\parallel$ in the isotropic PAD case. As in the anisotropic case, the perpendicular current density dominates near the equator, becoming smaller than the parallel component only about 0.5 R_E from the ionosphere. The bottom right hand plot shows $J_\parallel/J_\perp$, which shows that the current density is primarily field aligned near the ionosphere. Unlike in the previous example, in which $J_\parallel/J_\perp > 1000$ near the ionosphere, in this case it is less than five. Even in the anisotropic case, this ratio is less than eight. This is reiterated in the bottom center plot, which shows the perpendicular fraction of the current density in the isotropic case. This shows the current density being very nearly perpendicular to the magnetic field line near the equatorial plane, and remaining so until less than 1 R_E from the ionosphere. Even at the ionosphere, the perpendicular component makes up nearly 20% of the total current density. This is very different from the previous example, and from typical field lines in general.

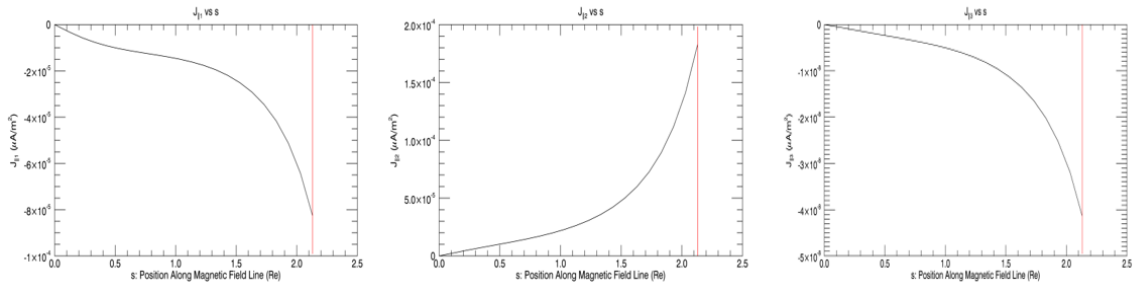

Figure 7.13: Components of current density calculated with anisotropic PAD. Left: $J_\parallel$ component due to $J_{\parallel 1}$ term. Middle: $J_\parallel$ component due to $J_{\parallel 2}$ term. Right: $J_\parallel$ component due to $J_{\parallel 3}$ term. On the x-axis, zero represents the point at which the magnetic field line crosses the equatorial plane. The red line is the point at which it intersects the ionosphere.

Figure 7.13 shows plots of the three terms that compose the anisotropic field aligned current density. The left hand plot shows the current density due to the $J_{\parallel 1}$ term. As previously mentioned, this is the only component to appear in the isotropic calculation. Thus, when this is the dominant term, the FACs calulated with the anisotropic pressure distribution will be very similar to those calculated with the isotropic pressure distribution. In this case, it can be seen

that the currents from this term are negative - that is, out of the ionosphere - like the FACs in the isotropic case. The shape of the curve, however, is somewhat different than usually seen. Instead of the field aligned component of the current density staying near zero throughout the region near the equatorial plane, in this case it jumps quickly from zero to a noticeable value; more than $10^{-5}\mu A/m^2$ in the outward direction. Moving closer to the ionosphere, the current density nearly levels out for the space of approximately 1 R_E along the field line, after which it increases rapidly in magnitude as seen in the previous example.

While the shape of the $J_{\parallel 1}$ curve is unusual, even more unusual is the magnitude relative to the $J_{\parallel 2}$ term. The current density due to this term peaks above $1.8 \times 10^{-4}\mu A/m^2$, greater than the $J_{\parallel 1}$ term. Because the current due to this term flows inward, it completely cancels out the current due to the first term, leaving an inward flowing current. This region is thus truly an effect of anisotropy, since this term does not appear in the isotropic case.

The left hand plot shows the field aligned current density due to the $J_{\parallel 3}$ term. This term is very small, nearly four orders of magnitude smaller than the others. It contributes an outward current, serving to reduce the magnitude of the total inward current slightly, but this amount is very small and may safely be neglected.

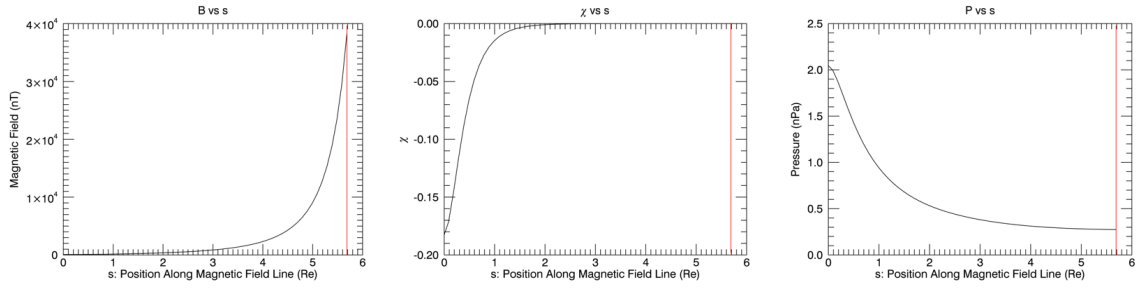

Figure 7.14: Left: Magnetic Field (nT), Middle: χ, Right: Scalar Pressure calculated with TWINS PAD (nPa). On the x-axis, zero represents the point at which the magnetic field line crosses the equatorial plane. The red line is the point at which it intersects the ionosphere.

The final region that will be examined is the secondary inward peak in the noon-dusk quadrant. This peak does not have the high magnitude of the first example, and is found at somewhat lower latitude (latitude $64°$, MLT 14h 40m for this field line). Further, while the previous magnetic field lines were in the inner tail region, this field line is in on the dayside.

Figure 7.14 plots the magnetic field, χ, and pressure along the field line. One can see that this field line is considerably longer than the previous example, though not quite as long as the first. The magnetic field is weak near the equatorial plane, and becomes much greater in magnitude by the ionosphere, peaking at nearly 40,000 nT. χ is negative, and has the greatest magnitude near the equatorial plane. Again, negative χ means that $P_\perp > P_\parallel$, and indicates that the pressure will decrease along the field line towards the ionosphere. Indeed, this behavior is seen in the right hand plot, where the anisotropic scalar pressure peaks near the equatorial plane, and drops to less than a quarter of the equatorial value at the ionosphere.

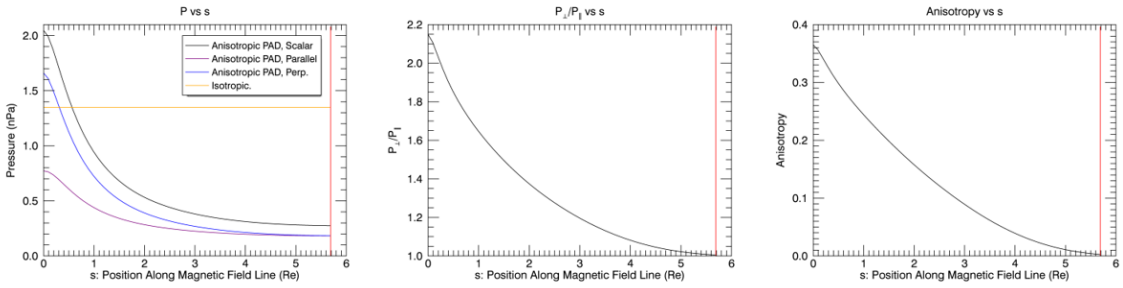

Figure 7.15: Left: All Pressures, plotted together (nPa), Middle: $P_\perp/P_\parallel$, Right: Pressure Anisotropy. On the x-axis, zero represents the point at which the magnetic field line crosses the equatorial plane. The red line is the point at which it intersects the ionosphere.

Figure 7.15 plots the various pressure components and the anisotropy along this field line. The left hand plot again shows constant pressure from the isotropic PAD, with pressure distributions for the anisotropic PAD case at a maximum near the equatorial plane and decreasing approaching the ionosphere. The first plot indicates that the perpendicular pressure is greater than the parallel pressure, but that the difference between them lessens until it is essentially zero by the ionosphere. The middle plot illustrates this, indicating that $P_\perp$ is more than twice the magnitude of $P_\parallel$ near the equatorial plane, but that they are essentially equal at the ionosphere. The left hand plot shows the anisotropy along the field line. Near the equatorial plane, the anisotropy is approximate 0.37, indicating that the perpendicular pressure is greater. Near the ionosphere, however, the pressure is nearly isotropic. In a case like this, one would not expect to see substantial differences between isotropic and anisotropic cases.

This expectation is borne out in the field aligned current components plotted in figures 7.16 and 7.17. In both cases, the field aligned current density is close to zero in the vicinity

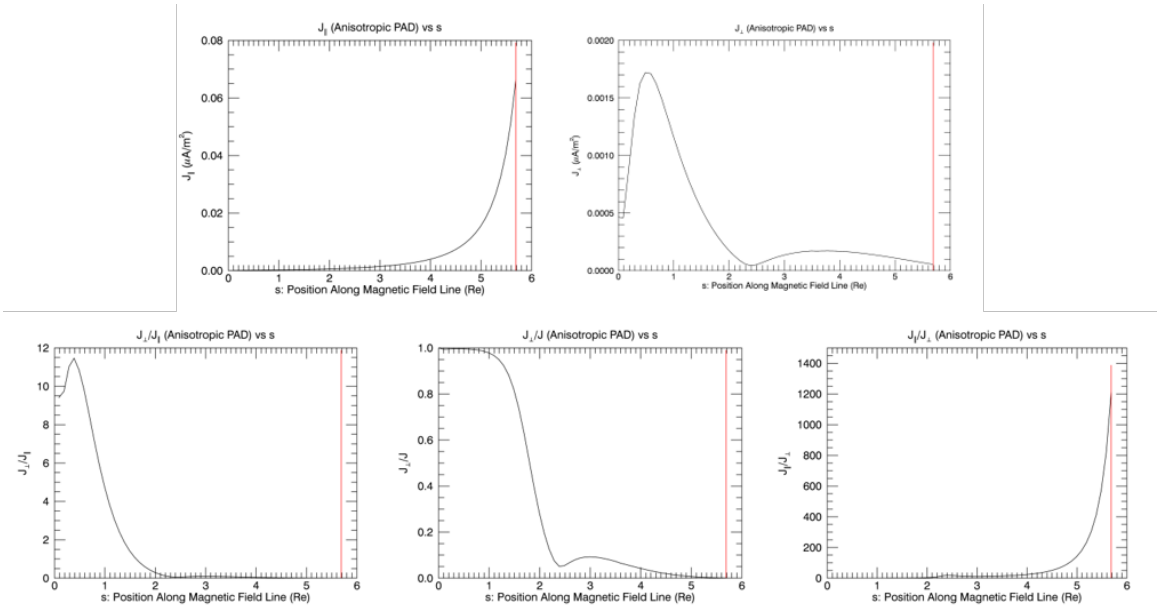

Figure 7.16: Current density calculated with anisotropic PADs. Top left: Field aligned component of current density. Positive indicates current is parallel to B field, negative indicates anti-parallel. Top right: Perpendicular component of current density. Bottom left: Perpendicular component divided by parallel component of current density. Since $J_{||}$ goes to zero near the equatorial plane, this plot is truncated. Bottom middle: The perpendicular component of the current density as a fraction of the magnitude of the current density. Bottom right: The field aligned component divided by the perpendicular component of the current density. On the x-axis, zero represents the point at which the magnetic field line crosses the equatorial plane. The red line is the point at which it intersects the ionosphere.

of the equatorial plane, and rises smoothly to a maximum at the ionosphere. The curves are very similar, with only minimal difference in magnitude. The perpendicular current density is another matter, though. In the isotropic case, the perpendicular current density is greatest near the equatorial plane, and decreases nearly linearly with decreasing distance to the ionosphere. The anisotropic case, however, is not so simple. In this case, the perpendicular current density has a much smaller value than the isotropic case at the equatorial plane, but increases rapidly, peaking approximately 5 R_E from the Earth along the field line, with a magnitude nearly 50% greater than the maximum in the isotropic case. It then plummets, reaching nearly zero by 3.3 R_E from the ionosphere along the field line, before rebounding for a second, smaller peak. While this second peak is small, it is a very unusual occurrence.

The unusual characteristics of the anisotropic perpendicular current density are reflected in the bottom row of plots in figure 7.16. These plots show how the different components

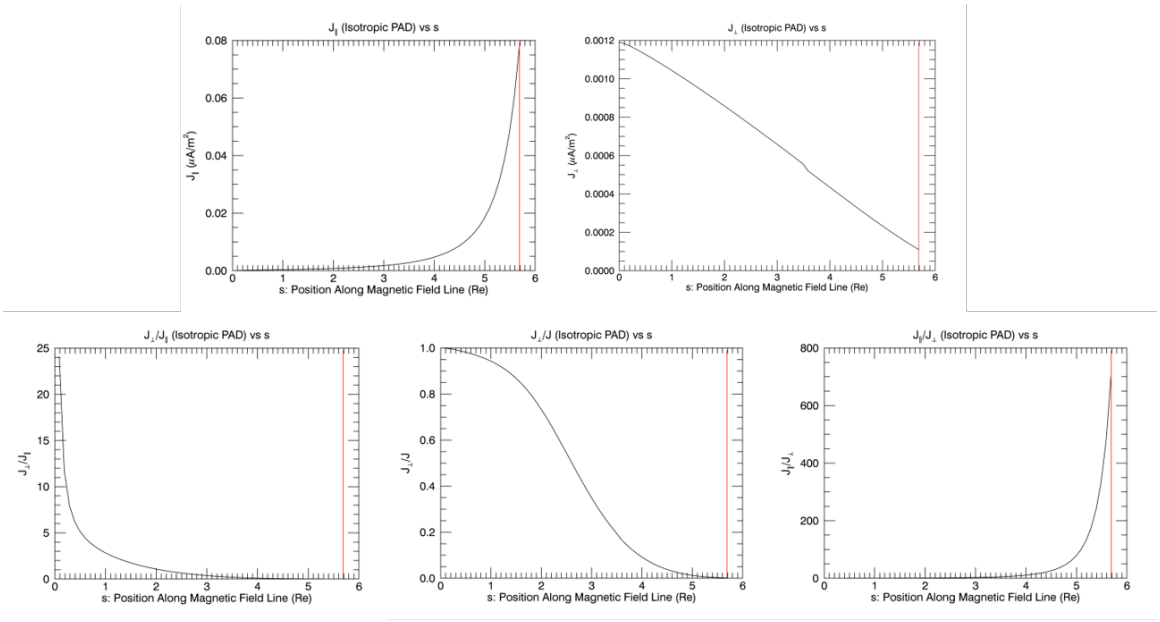

Figure 7.17: Current density calculated with isotropic PADs. Top left: Field aligned component of current density. Positive indicates current is parallel to B field, negative indicates anti-parallel. Top right: Perpendicular component of current density. Bottom left: Perpendicular component diveded by parallel component of current density. Since $J_{\parallel}$ goes to zero near the equatorial plane, this plot is truncated. Bottom middle: The perpendicular component of the current density as a fraction of the magnitude of the current density. Bottom right: The field aligned component divided by the perpendicular component of the current density. On the x-axis, zero represents the point at which the magnetic field line crosses the equatorial plane. The red line is the point at which it intersects the ionosphere.

of the current density relate to each other. The curl at the equatorial end of the left hand plot is due to the near-equatorial peak in $J_{\perp}$. Further, there is a very small bulge in the line at approximately 3.3 R_E from the ionosphere along the field line. Other than these, though, the line looks reasonably familiar. It shows the perpendicular component being the dominant component near the equatorial plane, while the parallel component dominates the ionospheric region, as clearly demonstrated in the right hand plot. The central plot shows what fraction of the current density is perpendicular to the magnetic field line. This has a bulge near 3.3 R_E from the ionosphere, which describes the small resurgence of the perpendicular current component, but otherwise this plot looks normal, as the perpendicular component nearly vanishes close to the ionosphere. The bottom row of figure 7.17 shows that, in the isotropic case, the current density is dominated by the perpendicular component near the equatorial plane, and strongly

dominated by the field aligned component near the ionosphere. The center plot shows that the transition between these states happens smoothly and symmetrically.

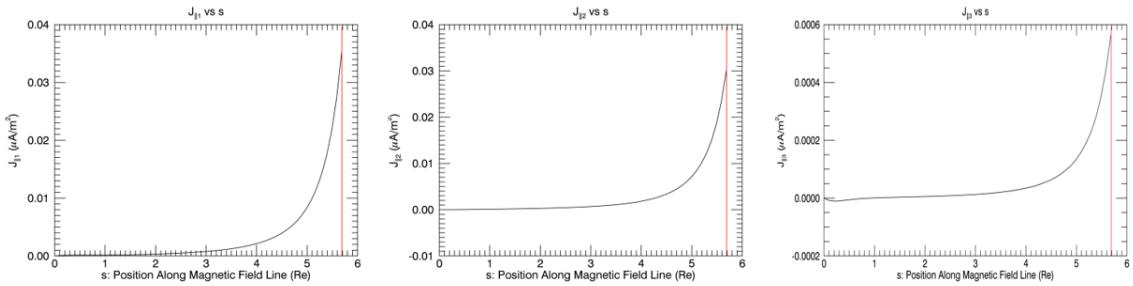

Figure 7.18: Components of current density calculated with anisotropic PADs. Left: $J_{\parallel}$ component due to $J_{\parallel 1}$ term. Middle: $J_{\parallel}$ component due to $J_{\parallel 2}$ term. Right: $J_{\parallel}$ component due to $J_{\parallel 3}$ term. On the x-axis, zero represents the point at which the magnetic field line crosses the equatorial plane. The red line is the point at which it intersects the ionosphere.

Figure 7.18 shows the contributions to the FACs due to each of the three integral terms in the anisotropic case. Despite the unusual peak in the pressure plots near the equatorial plane, all the components of the field aligned current density are relatively flat in this region. The $J_{\parallel 3}$ term has a negative dip in the region closest to the equatorial plane, but it is very small. It appears that, while $P_{\perp}$ certainly has unusual properties near the equatorial plane in this case, the gradient of $P_{\perp}$ is nearly either parallel or antiparallel to the magnetic field line in this region. When crossed with $\boldsymbol{\nabla} B$ the resulting vector does not have much of a field aligned component, and thus does not appear in the integrals calculating $J_{\parallel}$. Thus, the unusual pressure profile in this region has a much greater impact on the perpendicular currents than the FACs.

Chapter 8

Current Paths

As the previous section demonstrated, magnetospheric currents are, in general, neither exclusively field aligned nor perpendicular to the field. Rather, the total current at any given point is composed of both components. In the standard picture, Birkeland currents travel strictly along magnetic field lines, as shown in figure 1.3. This is particularly true for region 2 currents, which remain in the inner magnetosphere. Even region 1 currents, though, eventually make their way to the plasma sheet current along field lines. While it is often useful to consider FACs in this manner, because it connects ionospheric phenomena to equatorial conditions, it is not strictly true. While this is apparent from the behavior of the currents along a single magnetic field line, as shown in the previous chapter, it is illustrative to show the behavior of a current path, which will demonstrate the importance of the perpendicular current component in a more straight-forward way.

In order to demonstrate this, several points have been selected at which the current density can be calculated. The path of the current at this point is traced by following the direction of the current density, both forward and backward. This is done until either the current leaves the region for which TWINS has data, the current reaches the ionosphere, or the step limit - typically 10,000 steps - is reached. By following the total current, consisting of both parallel and perpendicular components, it becomes apparent that the current paths in the inner magnetosphere are considerably more complicated than the basic picture of figure 1.3 would indicate.

Figure 8.1 shows the current path of an arbitrarily chosen point on the equatorial plane at 07:00 UT, assuming an isotropic pressure distribution. As indicated by the plots in the previous chapter, the current density is dominated by the perpendicular component in the vicinity of the equatorial plane. This would lead one to believe that currents in this vicinity should remain near the equatorial plane over large distances, and indeed, this is what occurs. Figure 8.1 comprises three plots which, taken together, show a three dimensional view of the current path through

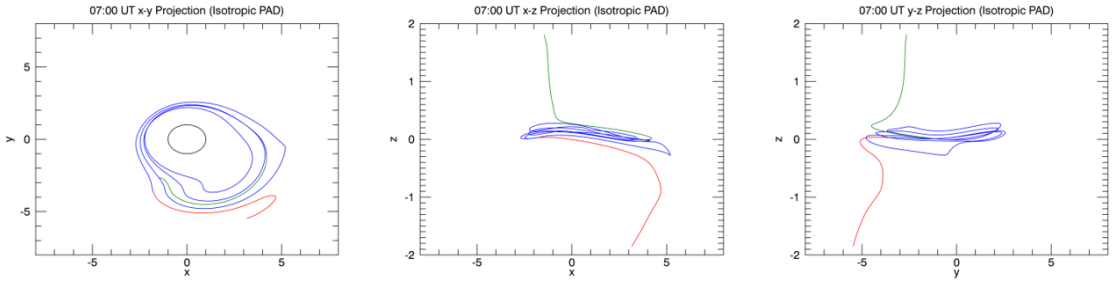

Figure 8.1: Selected Current Path in the case of Isotropic PAD for 07:00 UT. Left: x-y projection of current path. The black circle represents the position of the Earth. Middle: x-z projection of current path. Right: y-z projection of current path. In all figures, the current flows from the region highlighted in green to the region highlighted in red.

the inner magnetosphere. The left hand plot gives the x-y projection of the current path, the middle plot shows the x-z projection, and the right hand plot shows the y-z projection. In all these plots, the sun is to the right.

The left hand plot of figure 8.1 shows that the current occupies a region between 2 and 3 R_E from the ionosphere, and remains there over at least five circuits around the Earth. The other two show that the current does not remain on the equatorial plane. Rather, it oscillates above and below it, tending to be in the northern hemisphere in the vicinity of the x-axis, and the southern hemisphere near the y-axis. This is markedly different than the dipole magnetic field case, where a current on the equatorial plane will be trapped there. In the dipole case, there cannot be a current crossing from the northern to the southern hemisphere, or vice versa. Because of the non-dipolar nature of the magnetic field, however, the equatorial plane is not the surface of minimum magnetic field, and as explained in section 4.3, this allows a field aligned component of the current to exist at the equatorial plane.

Eventually the current reaches a point where a relatively large field aligned component exists, causing the current to move farther from the equatorial plane. The z-component continues to increase in magnitude as the current leaves the equatorial region, causing its path to bend more sharply northward, in the northern hemisphere, or southward, in the southern hemisphere. Because there remains a perpendicular component, however, the current continuously moves to different field lines. Eventually, the current reaches a field line for which TWINS has no data, and the calculation stops. The current, of course, continues onward. In this region, the ion

pressure is assumed to be approximately zero, which means the gradient of the ion pressure is also zero. As shown in equation 5.9, this means there can be no perpendicular current density in the case of an isotropic PAD. Thus, the current will continue to flow along the field line, eventually reaching either the ionosphere or the ring current near the equatorial plane.

In these figures, the current enters the region for which TWINS has measurements at the end highlighted in green, and moves toward the end highlighted in red, at which point it leaves the region of interest once again. In this case, the current flows from the northern hemisphere to the southern hemisphere. This scenario is impossible in the dipole magnetic field case, but happens regularly with the TS05 magnetic field. This illustrates the importance of using non-dipolar magnetic field models, even in the inner magnetosphere.

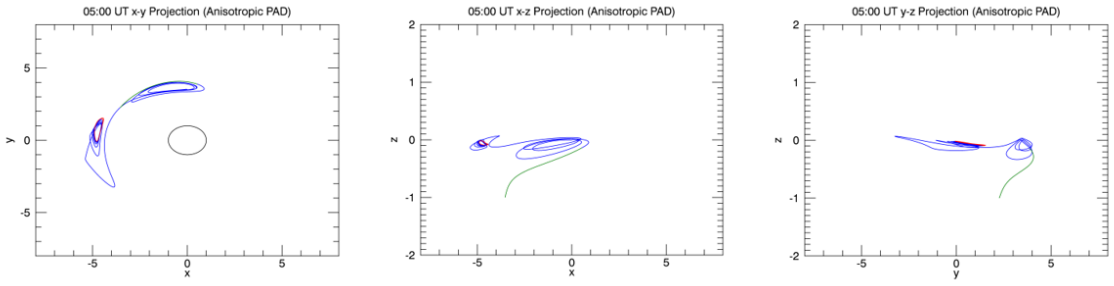

Figure 8.2: Selected Current Path in the case of Anisotropic PAD for 05:00 UT. Left: x-y projection of current path. The black circle represents the position of the Earth. Middle: x-z projection of current path. Right: y-z projection of current path. In all figures, the current flows from the region highlighted in green to the region highlighted in red.

Figure 8.2 shows an interesting current path from 05:00 UT, using the anisotropic pressure distributions. This path is much more complicated than the previous example, and the projections are more difficult to decipher. The left hand image is the x-y projection, and shows that the current is largely trapped around two points; one near dusk at about $4R_E$, and one near midnight at about 5 R_E. Both points are near the equatorial plane. The presence of two regions of current is a substantial difference from the previous example, but more unusual is the orientation of these regions. Both are tilted with respect to the equatorial plane. A plane through each would be tilted such that the northern part of it is angled toward the Earth.

The current loops near midnight are more tightly bound to the point they rotate about, which appears to be the piont of maximum ion pressure. This region has strong pressure gradients, which allows for greater perpendicular currents than in other regions (see equation 5.8). The loops are not only smaller in diameter, but they oscillate much less in the z-direction as well. The current loops near dusk are more loosely arranged, with a larger average distance from the point they revolve about, and a greater extent in the z-direction. This segment of current appears to encompass a region with relatively high pressure gradients in a region of high pressure near dusk. Again, this allows the existence of strong perpendicular currents. Both sets of current loops extend much further intho the southern hemisphere than the current loop in the first example. The current near dusk, in particular, extends 0.4 R_E south of the equatorial plane. The current eventually leaves the region for which data is available, extending extending nearly 1 R_E south of the equator. As with the previous example, the pressure in this region is assumed to be zero. This eliminates the perpendicular current density in the anisotropic PAD case, too. Thus, the current will continue along the magnetic field line until it reaches the ionosphere or equatorial plane.

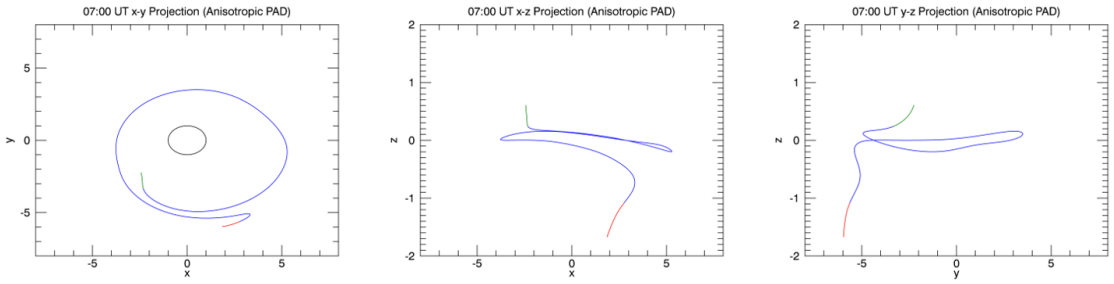

Figure 8.3: Selected Current Path in the case of Anisotropic PAD for 07:00 UT. Left: x-y projection of current path. The black circle represents the position of the Earth. Middle: x-z projection of current path. Right: y-z projection of current path. In all figures, the current flows from the region highlighted in green to the region highlighted in red.

Figures 8.3, 8.4, and 8.5 are all plots of current paths at 07:00 UT, and all begin at the same point on the equatorial plane. Figure 8.3 shows the current path in the case of the anisotropic pressure distribution, while figure 8.4 shows the current path in the isotropic pressure case. Figure 8.5 shows both cases on the same plot, to make comparison easier. Since both cases were calculated beginning at the same point on the equatorial plane (L=4, MLT=3h), one would

expect the currents to be similar. Tracing the current forward, this is approximately true; both currents flow counterclockwise around the Earth, exiting the region of TWINS observations to the south in roughly the same location. Tracing backward, however, the paths are not similar. The current in the isotropic PAD case rapidly turns to flow counterclockwise and exits to the north. In the Anisotropic PAD case, however, the current flows clockwise across the entire dayside before exiting the region of interest to the north.

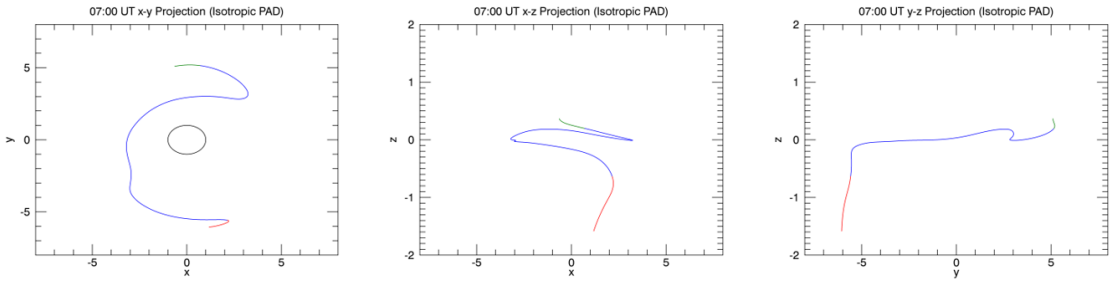

Figure 8.4: Selected Current Path in the case of Isotropic PAD for 07:00 UT. Left: x-y projection of current path. The black circle represents the position of the Earth. Middle: x-z projection of current path. Right: y-z projection of current path. In all figures, the current flows from the region highlighted in green to the region highlighted in red.

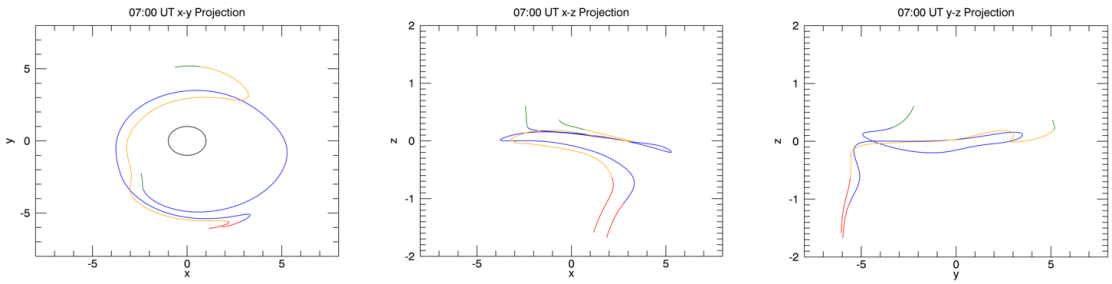

Figure 8.5: Selected Current Paths for Isotropic and Anisotropic PAD cases for 07:00 UT. The Isotropic PAD case is shown in orange, and the Anisotropic PAD case is shown in blue. Left: x-y projection of current paths. The black circle represents the position of the Earth. Middle: x-z projection of current paths. Right: y-z projection of current paths. In all figures, the current flows from the region highlighted in green to the region highlighted in red.

Looking at the behavior of the current flow as a whole, one may note that current in the anisotropic PAD case travels a complete path around the Earth before leaving the region near the equatorial plane, while the isotropic case travels only about three fourths of the way around. The northward-pointing currents are also in different places. In both cases, the northward turn occurs sharply, but in the anisotropic case, this turn occurs roughly halfway between midnight

and dawn, while in the isotropic case it occurs near dusk. These discrepancies indicate a significant difference between the isotropic and anisotropic cases. While the FAC plots at the ionosphere look very similar in most cases, it is important to remember that this does not necessarily indicate the currents near the equatorial plane are the same. The perpendicular component of the current density can be quite different, yet still allow similar field aligned results.

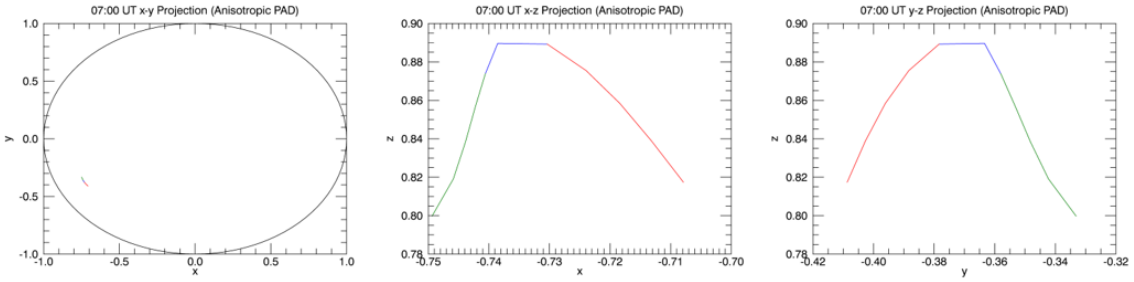

Figure 8.6: Current Path for 07:00 UT region of low latitude inward current on nightside. Left: x-y projection of current path. The black circle represents the position of the Earth. Middle: x-z projection of current path. Right: y-z projection of current path. In all figures, the current flows from the region highlighted in green to the region highlighted in red.

The final set of plots to be examined begin at the ionosphere in the region of low latitude inward current, discussed in section 6.2 (see figure 6.3), using the anisotropic pressure distribution at 07:00 UT. In the classic picture shown in figure 1.3, the currents in this region would extend to the equatorial plane, connecting to equatorial currents in the inner magnetopshere. These plots, however, show this not to be the case. Instead, the perpendicular current moves them off the field line, quickly moving the current path to a field line on which the field aligned component is in the opposite direction. In this case, the current at the ionosphere pointed inward, so it was traced backward. The perpendicular current rapidly moved the trace point away from the region of inward current, until the trace began moving back toward the ionosphere once again. In a relatively small number of steps, the current had returned to the ionosphere. Due to its high conductivity, the ionosphere completes the circuit. Thus, current is drawn from the ionosphere, flows briefly through the magnetosphere in the region near Earth, and then returns to the ionosphere. In these cases, it does not travel to the equatorial plane.

This is consistent with Roelof [2004]. In figure 4.2, one can see that currents intersecting the ionosphere never extend down to the equatorial plane. While the currents traced by Roelof

[2004] extend much further into the magnetosphere than those calculated in this work, there are important reasons for these differences. First, Roelof has chosen currents that intersect the ionosphere at higher latitude than those of figure 8.6. This means the currents are associated with magnetic field lines that take a longer path to reach the equatorial plane. Second, Roelof worked with a dipole magnetic field and isotropic PAD, while figure 8.6 was calculated using the TS05 magnetic field model and measured TWINS anisotropic PAD. This makes both the gradients of both pressure and magnetic field more complicated. Finally, the current path in figure 8.6 was specifically chosen to intersect the ionosphere in an unusual region, in which an inward flow of current is bordered by an outward flow of current. Given the close proximity of these opposite flows, it is no surprise that the current path would reverse direction so quickly. While the current loop is shorter than those pictured in Roelof [2004], the behavior is very similar. The method used here produces results that, while consistent with Roelof [2004], do not employ the simplifying assumtions used in that work. These results are thus both more complicated and more realistic.

Chapter 9

References

1. Bazell, D., E. C. Roelof, T. Sotirelis, P. C. Brandt, H. Nair, P. Valek, J. Goldstein, and D. McComas (2010), Comparison of TWINS images of low-altitude emission of energetic neutral atoms with DMSP precipitating ion fluxes, J. Geophys. Res., 115, A10204, doi:10.1029/2010JA015644.

2. Brandt, P., E. C. Roelof, S. Ohtani, D. G. Mitchell, and B. Anderson, IMAGE/HENA: pressure and current distributions during the 1 October 2002 storm, Advances in Space Research, 33.5, 719-22, 2004.

3. Chen, M. W., J. L. Roeder, J. F. Fennell, and L. R. Lyons, Simulations of ring current proton pitch angle distributions, J. Geophys. Res., 103, 165-178, 1998.

4. Chen, M. W., J. L. Roeder, J. F. Fennell, L. R. Lyons, R. L. Lambour, M. Schulz, Proton ring current pitch angle distributions: Comparison of simulations with CRRES observations, J. Geophys. Res., 104, 379-389, 1999.

5. Cowley, S. W. H., The effect of pressure anisotropy on the equilibrium structure of magnetic current sheets, Planet. Space Sci., 26, 1037, 1978.

6. Goldstein, J., and D. McComas (2013), Five years of stereo magnetospheric imaging by TWINS, Space Sci. Rev., 180(14), 3970, doi:10.1007/ s11214-013-0012-8.

7. Goldstein, J., P. Valek, D. J. McComas, and J. Redfern (2012a), Latitudinal anisotropy in ring current energetic neutral atoms, Geophys. Res. Lett., 39, L08102, doi:10.1029/2012GL051417.

8. Goldstein, J., P. Valek, D. J. McComas, and J. Redfern (2012b), TWINS energetic neutral atom observations of local-time-dependent ring current anisotropy, J. Geophys. Res., 117, A11213, doi:10.1029/2012JA017804.

9. Grimes, Eric W. Evolution of the Earth's Ring Current during Geomagnetic Storms. Thesis. Auburn University, 2012. Print.

10. Heinemann, M., Representations of currents and magnetic fields in anisotropic magnetohydrostatic plasma, J. Geophys. Res. 95.A6, 7789, 1990.

11. Heinemann, M., and D. H. Pontius, Jr., Representations of currents and magnetic fields in isotropic magnetohydrostatic plasma, J. Geophys. Res., 95,251, 1990.

12. Iijima, Takesi, Thomas A. Potemra, and Laurence J. Zanetti. (1997), Contribution of pressure gradients to the generation of dawnside region 1 and region 2 currents, J. Geophys. Res.: Space Physics 102.A12, 27069-7081.

13. Mauk, B. H., and L. J. Zanetti (1987), Magnetospheric electric fields and currents, Reviews of Geophysics, 25.3, 541.

14. McComas, D. J., P. Valek, J. L. Burch, C. J. Pollock, R. M. Skoug, and M. F. Thomsen (2002), Filling and emptying of the plasma sheet: Remote observations with 170 keV energetic neutral atoms, Geophys. Res. Lett., 29(22), 2079, doi:10.1029/2002GL016153.

15. McComas, D. J., et al. (2009), The Two Wide-angle Imaging Neutral-atom Spectrometers (TWINS) NASA mission-of-opportunity, Space Sci. Rev., 142, 157231, doi:10.1007/s11214-008-9467-4.

16. Parker, E. N., Newtonian development of dynamical properties of ionized gases of low density, Phys. Rev., 107, 924, 1957

17. Perez, J. D., M.-C. Fok, and T. E. Moore (2000), Deconvolution of energetic neutral atom images of the Earths magnetosphere, Space Sci. Rev.,91, 421.

18. Perez, J. D., G. Kozlowski, P. C:son Brandt, D. G. Mitchell, J.-M. Jahn, C. J. Pollock, and X.-X. Zhang (2001), Initial ion equatorial pitch angle distributions from medium and high energy neutral atom images obtained by IMAGE, Geophys. Res. Lett., 28, 1155.

19. Perez, J. D., X.-X. Zhang, P. C:son Brandt, D. G. Mitchell, J.-M. Jahn, C. J. Pollock, and S. B. Mende (2004), Trapped and precipitating protons in the inner magnetosphere as seen by IMAGE, J. Geophys. Res., 109, A09202, doi:10.1029/2004JA010421.

20. Perez, J. D., X.-X. Zhang, P. C:son Brandt, D. G. Mitchell, J.-M. Jahn, and C. J. Pollock (2004), Dynamics of ring current ions as obtained from IMAGE HENA and MENA ENA images, J. G eophys. R es., 109, A05208, doi:10.1029/2003JA010164.

21. Perez, J. D., E. W. Grimes, J. Goldstein, D. J. McComas, P. Valek, and N. Billor (2012), Evolution of CIR storm on 22 july 2009, J. Geophys. Res., 117, A09221, doi:10.1029/2012JA017572.

22. Perez, J. D., E. W. Grimes, J. Goldstein, D. J. McComas, and P. Valek (2013), Validation of a method for obtaining ion intensities from ENA images using data from TWINS and THEMIS, J. Geophys. Res. Space Physics, doi:10.1029/2010JA015343.

23. Perez, J. D., J. Goldstein, D. J. McComas, P. Valek, N. Buzulukova, M.-C. Fok, and H. J. Singer (2015), TWINS stereoscopic imaging of multiple peaks in the ring current, J. Geophys. Res. Space Physics, 120, 368383, doi:10.1002/2014JA020662.

24. Pollock, C., et al. (2003), The role and contributions of energetic neutral atom (ENA) imaging in magnetospheric substorm research, Space Sci. Rev., 109, 155182, doi:10.1023/B:SPAC.0000007518.933

25. Roelof, E. C. (1987), Energetic neutral atom image of a storm-time ring current, Geophys. Res. Lett., 14(6), 652655, doi:10.1029/ GL014i006p00652.

26. Roelof, E. C. (1997), ENA emission from nearly-mirroring magnetospheric ions interacting with the exosphere, Adv. Space Res., 20(3), 361366, doi:10.1016/S0273-1177(97)00692-3.

27. Roelof, E.c, P. C:son Brandt, and D.g Mitchell. "Derivation of currents and diamagnetic effects from global plasma pressure distributions obtained by IMAGE/HENA." Advances in Space Research 33.5 (2004): 747-51. Web.

28. Tsyganenko, N. A., and M. I. Sitnov. ”Modeling the dynamics of the inner magnetosphere during strong geomagnetic storms.” Journal of Geophysical Research 110.A3 (2005): n. pag. Web.

29. Valek, P., P. C. Brandt, N. Buzulukova, M. C. Fok, J. Goldstein, D. J. McComas, J. D. Perez, E. Roelof, and R. Skoug (2010), Evolution of low-altitude and ring current ENA emissions from a moderate magnetospheric storm: Continuous and simultaneous TWINS observations, J. Geophys. Res., 115, A11209, doi:10.1029/2010JA015429.

30. Valek, P. W., J. Goldstein, D. J. McComas, R. Ilie, N. Buzulukova, M. C. Fok, and J. D. Perez (2013), Oxygen-hydrogen differentiated observations from TWINS: The 22 July 2009 storm, J. Geophys. Res. Space Physics, 118, 33773393, doi:10.1002/jgra.50204.

31. Valek, P. W., J. Goldstein, D. J. McComas, M. C. Fok, and D. Mitchell (2014), Large magnetic storms as viewed by TWINS: A study of the differences in the medium energy ENA composition, J. Geophys. Res. Space Physics, 119, 28192835, doi:10.1002/2014JA019782.

32. Vasyliunas, V. M., Mathematical models of magnetospheric convection and its coupling to the ionosphere, in Particles and Fields in the Magnetosphere, edited by B. M. McCormac, p. 60, D. Reidel, Hingham, Mass., 1970.

33. Vasyliunas, V. M., Fundamentals of current description, in Magnetospheric Currents, Geophys. Monogr. Ser., vol. 28, edited by T. A. Potemra, p. 63, AGU, Washington, D.C., 1984.

34. Zoennchen, J. H., U. Nass, G. Lay, and H. J. Fahr. (2010), 3-D-geocoronal hydrogen density derived from TWINS Ly--data, Annales Geophysicae 28.6, 1221-228.

35. Zoennchen, J. H., J. J. Bailey, U. Nass, M. Gruntman, H. J. Fahr, and J. Goldstein (2011), The TWINS exospheric neutral H-density distribution under solar minimum conditions, Annales Geophysicae 29.12, 2211-217.

36. Zoennchen, J. H., U. Nass, and H. J. Fahr (2015), Terrestrial exospheric hydrogen density distributions under solar minimum and solar maximum conditions observed by the TWINS stereo mission, Ann. Geophys., 33(3), 413426, doi:10.5194/angeo-33-413-2015.